

Renormierungsgruppenanalyse des Hubbard-Modells in zwei Dimensionen

Daniel Rohe

MAX-PLANCK-INSTITUT FÜR FESTKÖRPERFORSCHUNG

STUTT GART, 2005

MEINEN GROSSELTERN

Renormierungsgruppenanalyse des Hubbard-Modells in zwei Dimensionen

Von der Fakultät Mathematik und Physik der Universität Stuttgart
zur Erlangung der Würde eines
Doktors der Naturwissenschaften (Dr. rer. nat.)
genehmigte Abhandlung

Vorgelegt von

Daniel Rohe

aus Jülich

Hauptberichter:	Prof. Dr. W. Metzner
Mitberichter:	Prof. Dr. A. Muramatsu
Tag der mündlichen Prüfung:	13. Januar 2005

MAX-PLANCK-INSTITUT FÜR FESTKÖRPERFORSCHUNG

STUTTGART, 2005

Contents

Zusammenfassung	III
Introduction	1
1 Hubbard Model and RG Technique	3
1.1 The two-dimensional Hubbard Model	3
1.2 Functional Description	6
1.3 Renormalisation-Group Methods	9
2 Numerical Treatment	19
2.1 Static Approximation	19
2.2 Discretisation of the Brillouin Zone	21
2.3 External vs Internal Projection	22
2.4 Integrating the RGE	24
2.5 How Many Patches Do We Need?	24
3 Critical Scales and Dominant Correlations	27
3.1 Parameters	28
3.2 Wick-ordered vs 1-PI Scheme	29
3.3 Critical Scales	30
3.4 Dominant Correlations	33
3.5 Discussion	40
4 Self Energy and Spectral Function	43
4.1 Spectral Function and Quasi-Particle Peak	43
4.2 Adjustment of the Fermi Surface	45
4.3 Calculating the Self Energy at Real Frequencies	46
4.4 Parameters	48
4.5 Results	49
4.6 Discussion	64
5 Discussion and Conclusion	67
Appendix	68
A Polchinski and Wiczerkowski Equations	69
B Evaluation of RHS for the Two-point Function	73

Zusammenfassung

In dieser Arbeit werden Korrelationseffekte in niedrigdimensionalen Elektronensystemen untersucht, die unter anderem für die Physik in kupratbasierten Hochtemperatursupraleitern (HTSL) eine wichtige Rolle spielen. Die theoretische Beschreibung von Systemen wechselwirkender Elektronen erweist sich in diesem Zusammenhang als ausgesprochen schwierig. In herkömmlichen metallischen Systemen kann der Wechselwirkung im Rahmen der Fermiflüssigkeitstheorie genüge getan werden, die eine stark vereinfachte aber dennoch quantitativ erstaunlich gute Beschreibung der niederenergetischen elektronischen Freiheitsgrade liefert. In niedrigen Dimensionen sind Wechselwirkungs- und Korrelationseffekte allerdings bedeutsamer. Es ist diese Niedrigdimensionalität, verbunden mit einer starken, kurzreichweitigen Wechselwirkung der Elektronen untereinander, die zu den reichhaltigen und komplexen physikalischen Eigenschaften der HTSL führt.

Eines der Prototypmodelle im Kontext von HTSL ist das zweidimensionale Hubbard-Modell (2D-HM), das die Dynamik von Elektronen auf einem zweidimensionalen Quadratgitter unter dem Einfluß einer lokalen, abstoßenden Wechselwirkung beschreibt. Obgleich dieses Modell schon vor über 40 Jahren eingeführt wurde, und trotz seiner scheinbaren Einfachheit, ist es bisher nicht gelungen, seine Eigenschaften zweifelsfrei zu bestimmen, geschweige denn eine allgemeine exakte Lösung zu finden. Außerdem ist es umstritten, in wiefern es als theoretische Basis für HTSL geeignet bzw. hinreichend ist. Trotzdem, oder gerade deswegen, steht das 2D-HM auch heute noch im Fokus der theoretischen Festkörperphysik. Es bedarf dabei der Entwicklung neuer Methoden, um substantielle Fortschritte erreichen zu können. Dies ist ein wesentliches Ziel dieser Arbeit, in der die sogenannte funktionale Renormierungsgruppe (fRG) auf das 2D-HM angewendet wird. Die fRG erlaubt es, aufbauend auf einer exakten funktionalen Beschreibung der elektronischen Freiheitsgrade eine Energieskalentrennung vorzunehmen und auf kontrollierte Art und Weise eine Näherung für die effektive Niederenergiephysik zu bestimmen. Auf dem aktuellen Niveau ist diese Näherung perturbativ, das bedeutet sie gilt nur im Bereich hinreichend schwacher Wechselwirkung. Allerdings stellt sich heraus, daß im 2D-HM bereits in diesem Fall höchst nichttriviales Verhalten auftritt, das sich mit einigen wichtigen Eigenschaften von HTSL deckt, obwohl in diesen Materialien die Wechselwirkung in der Regel als deutlich stärker anzusetzen ist. Jedoch gibt es Hinweise, daß in elektrondotierten HTSL die Kopplung schwächer ist als in den "traditionellen" lochdotierten Kupraten, was der quantitativen Anwendung perturbativer Methoden entgegenkom-

men könnte.

Diese Arbeit baut auf den Dissertationen von C. J. Halboth [1] und C. Honerkamp [2] auf, in denen zwei verschiedene Versionen der fRG in unterschiedlichen Parameterbereichen auf das 2D-HM angewandt wurden. Wir vergleichen die Resultate beider Schemata für identische Parameter und Randbedingungen, um etwas über die Zuverlässigkeit und Aussagekraft der Ergebnisse zu erfahren. Desweiteren erweitern wir die bestehenden Rechnungen dahingehend, daß wir spektrale Einteilcheneigenschaften im Niederenergiebereich mit Hilfe der fRG untersuchen.

Kapitel 1

Im ersten Kapitel wird das zweidimensionale Hubbard-Modell eingeführt, und es wird ein konzeptioneller Überblick über verschiedene Renormierungsgruppenschemata gegeben. Schließlich werden die genäherten Versionen der Renormierungsgruppengleichung in der Form, wie wir sie benutzen, vorgestellt.

Hubbard-Modell

Das Hubbard-Modell ist ein quantenmechanisches Model zur Beschreibung von wechselwirkenden Elektronen auf einem Quadratgitter, die einer lokalen Wechselwirkung unterworfen sind. Der zugehörige Hamiltonoperator $\mathcal{H} = \mathcal{H}_0 + \mathcal{H}_I$ setzt sich additiv zusammen aus einem kinetischen Anteil \mathcal{H}_0 und einem Wechselwirkungsanteil \mathcal{H}_I .

Der freie Anteil \mathcal{H}_0 hat seinen Ursprung in der tight-binding Beschreibung für die Elektrodynamik in Festkörpern und lautet in zweiter Quantisierung

$$\mathcal{H}_0 = -t \sum_{\langle i,j \rangle, \sigma} \psi_{\mathbf{r}_i, \sigma}^\dagger \psi_{\mathbf{r}_j, \sigma} - t' \sum_{\langle\langle i,j \rangle\rangle, \sigma} \psi_{\mathbf{r}_i, \sigma}^\dagger \psi_{\mathbf{r}_j, \sigma} \quad ,$$

wobei die Amplituden t und t' das Hüpfen eines Elektrons zum nächsten bzw. übernächsten Nachbargitterplatz parametrisieren. Der Operator $\psi_{\mathbf{r}_i, \sigma}^\dagger$ ($\psi_{\mathbf{r}_i, \sigma}$) erzeugt (vernichtet) ein Elektron mit Spinprojektion σ am Gitterplatz \mathbf{r}_i . \mathcal{H}_0 ist diagonal im reziproken Raum:

$$\mathcal{H}_0 = \sum_{\mathbf{k}, \sigma} \epsilon_{\mathbf{k}}^0 \psi_{\mathbf{k}, \sigma}^\dagger \psi_{\mathbf{k}, \sigma} \quad ,$$

mit der freien Dispersion

$$\epsilon_{\mathbf{k}}^0 = -2t(\cos k_x + \cos k_y) - 4t' \cos k_x \cos k_y.$$

\mathcal{H}_I beschreibt die Abstoßung zwischen zwei Elektronen am gleichen Gitterplatz:

$$\mathcal{H}_I = U \sum_i n_{\mathbf{r}_i, \uparrow} n_{\mathbf{r}_i, \downarrow}$$

wobei $n_{\mathbf{r}_i, \sigma} := \psi_{\mathbf{r}_i, \sigma}^\dagger \psi_{\mathbf{r}_i, \sigma}$ der Operator der Teilchendichte für Teilchen mit Spinprojektion σ am Gitterplatz \mathbf{r}_i ist.

Die interessante Physik spielt sich in der Umgebung halber Füllung ab. Bei verschwindendem t' ist der Grundzustand des 2D-HM genau bei halber Füllung antiferromagnetisch. Bei endlichem t' und/oder Abweichung von halber Füllung gibt es einen Übergang zu einem supraleitenden Grundzustand. Ab einer bestimmten Temperatur, die sowohl von t' als auch der Füllung abhängt, verschwindet die spontane Symmetriebrechung. Die Eigenschaften in der normalen Phase in der Nähe dieser Übergangstemperatur werden jedoch von den in diesem Parameterbereich auftretenden starken Korrelationen beeinflusst.

Renormierungsgruppenmethoden

Seit den Arbeiten von Wilson [3] sind Renormierungsgruppenmethoden ausgesprochen erfolgreich in vielen Bereichen der theoretischen Physik angewendet worden. Ausgangspunkt ist die Beschreibung der Eigenschaften eines physikalischen Modells durch seine Korrelationsfunktionen. Von diesen gibt es verschiedene Arten, die sich alle ineinander überführen lassen. Zu jeder lässt sich ein Funktional in Grassmannfeldern η und $\bar{\eta}$ definieren gemäß

$$\mathcal{G}^X[\bar{\eta}, \eta] = \sum_n G_{2n}^X(\alpha_1, \dots, \alpha_n, \beta_n, \dots, \beta_1) \bar{\eta}_{\alpha_1} \dots \bar{\eta}_{\alpha_n} \eta_{\beta_n} \dots \eta_{\beta_1},$$

wobei die Indizes α_i und β_i alle Einteilchenquantenzahlen durchlaufen, und Summation über doppelte Indizes impliziert ist. Das Label X definiert die Art der Korrelationsfunktionen, z.B. zusammenhängende oder einteilchenirreduzible, und das Funktional wird in den zugehörigen $2n$ -Punktfunktionen $G_{2n}^X(\alpha_1, \dots, \alpha_n, \beta_n, \dots, \beta_1)$ entwickelt.

Die Kernidee der Renormierungsgruppe besteht nun darin, zunächst durch die Einführung eines zusätzlichen Parameters eine Skalentrennung zu definieren, z.B. in einer Energie- oder

Längenskala, um sich dann mittels einer schrittweisen Veränderung dieses Parameters dem ursprünglichen physikalischen Problem zu nähern. In dieser Arbeit wird zunächst im reziproken Raum nach freien Energieskalen abwärts sortiert und alle Moden “ausgeschaltet”. Dann werden die hochenergetischen Moden sukzessive “angeschaltet”. Ganz allgemein führt die Einführung eines zusätzlichen Parameters Λ zur sogenannten Renormierungsgruppen-gleichung (RGE) für die $2n$ -Punktfunktionen

$$\partial_{\Lambda} G_{2n}^X(\Lambda | \alpha_1, \dots, \alpha_n, \beta_n, \dots, \beta_1) = R^X[G_{2m}^X(\Lambda | \alpha_1, \dots, \alpha_m, \beta_m, \dots, \beta_1); m = 1 \dots \infty] \quad .$$

Dies ist eine unendliche Hierarchie gekoppelter Integro-Differentialgleichungen, die in der Praxis trunziert werden muß, damit der Renormierungsgruppenfluß für das 2D-HM numerisch durchgeführt werden kann. Wir erreichen dies, indem wir die Sechspunktfunktion auf Null setzen, was ihrem Anfangswert entspricht.

Kapitel 2

In Kapitel 2 werden die grundlegenden Näherungen sowie die technischen Schritte erläutert, die für die oben angesprochene numerische Integration der RGE notwendig sind. Die Vierpunktfunktion, auch effektive Wechselwirkung genannt, wird parametrisiert durch ihre statischen Komponenten auf der Fermifläche. Zusätzlich wird die tangentielle Impulsabhängigkeit diskretisiert. Diese relativ drastischen Näherungen sind zwingend notwendig, um das Problem computerunterstützt behandeln zu können. Die Projektion im reziproken Raum auf die Fermifläche wird im Detail definiert, und diverse Probeläufe motivieren die Wahl einer bestimmten Diskretisierung der Brillouinzone, die in Abbildung 2.3 zu sehen ist.

Kapitel 3

In Kapitel 3 vergleichen wir im Detail die Ergebnisse des fRG-Flusses der effektiven Wechselwirkung im sogenannten Wick-geordneten Schema mit den Ergebnissen im einteilchen-irreduziblen (1-PI) Schema. In beiden Fällen fließt die effektive Wechselwirkung zu starker Kopplung, und das Wechselspiel zwischen Teilchen-Loch Prozessen, die antiferromagnetische Tendenzen begünstigen, und Teilchen-Teilchen Prozessen, die für Supraleitungstendenzen verantwortlich sind, wird qualitativ gleich beschrieben. Im quantitativen Bereich zeigen sich allerdings teilweise nicht unerhebliche Diskrepanzen, was wiederum nicht

übermäßig verwundert, da nicht-universelle Größen betrachtet werden. Dies führt unter anderem dazu, daß die Temperaturskala, bei der starke Korrelationen einsetzen, als Funktion des chemischen Potentials nur sehr grob bestimmt werden kann.

Der wichtigste Aspekt der detaillierten Analyse ist die Beobachtung, daß sogenannte Hot Spots eine besondere Rolle spielen. Sie sind definiert als die Punkte, an denen die Fermifläche die Umklappfläche, definiert durch $|\mathbf{k}_x| + |\mathbf{k}_y| = \pi$, schneidet. Sie sind deshalb ausgezeichnete Punkte, weil sie durch einen Impulsübertrag $\mathbf{Q} = (\pi, \pi)$ verbunden werden können, und dadurch in Gittermodellen einen zusätzlichen niederenergetischen Streukanal öffnen.

Beide Näherungen sind ein-loop Gleichungen, die über konventionelle störungstheoretische Resummationen wie T-Matrix oder Random Phase Approximation (RPA) hinausgehen, da sie die Kopplung zwischen Teilchen-Teilchen und Teilchen-Loch Beiträgen in führender Ordnung berücksichtigen. Allerdings sind diese ein-loop Näherungen nicht-selbstkonsistent, das heißt, daß die Rückkopplung von Selbstenergieeffekten auf die rechte Seite der RGE vernachlässigt wird.

Kapitel 4

In Kapitel 4 wird das Wick-geordnete fRG Schema angewendet, um den Einfluß der in Kapitel 3 erörterten starken Korrelationen in der Nähe einer kritischen Temperaturskala auf Einteilchenspektraleigenschaften im Niederenergiebereich zu untersuchen. Dazu wird parallel zur Renormierungsgruppengleichung für die effektive Wechselwirkung die RGE für die Einteilchenselbstenergie numerisch integriert, um oberhalb einer kritischen Temperatur den Imaginärteil der Selbstenergie zu bestimmen. Daraus läßt sich anschließend der Realteil mittels einer Kramers-Kronig Beziehung bestimmen, und damit auch unmittelbar die Einteilchenspekttralfunktion.

Die Einkopplung der renormierten Wechselwirkung in den Fluß der Selbstenergie führt zu teilweise drastischen Effekten im Einteilchenspektrum. Analog zu den Beobachtungen in Kapitel 3 spielen auch hier die Hot Spots eine besondere Rolle. In ihrer Umgebung entsteht im Falle starker renormierter Kopplungen eine ausgeprägte negative Spitze im Imaginärteil der Selbstenergie, was in der Spektralfunktion zu einer Mulde im sonst lorentzartigen Spektralpeak führt. Dieses Phänomen wird als das Einsetzen eines Pseudogaps interpretiert, und ist im Fall schwacher nackter Kopplung sowohl in seiner Impuls-, als auch seiner Temperaturabhängigkeit auf einen relativ kleinen Bereich beschränkt. Schwächere Korrelationseffekte wie z.B. erhöhte Streuraten oder reduzierte Quasiteilchengewichte sind hingegen in

einem breiteren Parameterbereich präsent.

Es zeigt sich weiterhin, daß in Abhängigkeit vom chemischen Potential unterschiedliche Korrelationen für diese Pseudogapphysik verantwortlich sind. Während bei und in der Nähe von van Hove Füllung sowohl Q -transferierende Teilchen-Loch Prozesse, als auch Teilchen-Teilchen Prozesse mit Gesamtimpuls Null (Cooperkanal) zum anomalen Verhalten des Imaginärteils der Selbstenergie beitragen, so sind es mit wachsendem Abstand von der van Hove Skala hin zu höheren Füllungen weniger Teilchen-Teilchen Korrelationen, sondern in erster Linie Teilchen-Loch Beiträge.

Die Selbstenergie ist von Katanin und Kampf ebenfalls mittels fRG behandelt worden, allerdings im 1-PI Schema und auf technisch etwas andere Weise [4]. Auch dabei gilt das Interesse dem Einfluß starker effektiver Wechselwirkungen auf Einteilcheneigenschaften, jedoch vornehmlich in der Nähe von van Hove Füllung. Dabei zeigen sich Unterschiede im generischen Verhalten der Spektralfunktion im Vergleich zu den Resultaten in dieser Arbeit. Es werden ebenfalls starke Signaturen im Niederenergieverhalten beobachtet, allerdings entwickelt sich die Spektralfunktion qualitativ anders. Es entsteht zwar ebenfalls ein Pseudogap, jedoch überlebt im generischen Fall ein schmaler Quasiteilchenpeak in der Mitte des Pseudogaps. Dies ist ein gravierender qualitativer Unterschied. Aus technischer Sicht verstehen wir, wie diese Unterschiede entstehen können. Welches Bild physikalisch realistischer ist, läßt sich ohne weiteres dagegen nicht sagen. Dies ist eine der Fragen, die durch eine genauere Analyse der verschiedenen Approximationen zu untersuchen ist. Dies betrifft vor allem die Wahl des Flußparameters, das Niveau der Trunkierung, sowie die Parametrisierung der effektiven Wechselwirkung.

Abschließende Bemerkungen

In dieser Arbeit haben wir funktionale Renormierungsgruppenmethoden auf das zweidimensionale Hubbard-Modell (2D-HM) angewendet, indem approximative Renormierungsgruppengleichungen mittels numerischer Integration gelöst wurden. Dies diente zum einen der Methodenentwicklung, da der Anwendungsbereich von fRG Methoden erweitert wurde. Zum anderen haben wir neue Einsichten in das Verhalten des 2D-HM gewonnen.

Abschließend sei erwähnt, daß fRG Methoden nicht auf das 2D-HM und verwandte Modelle beschränkt, sondern sehr allgemein anwendbar sind. So wurden und werden sie unter Anderem sehr erfolgreich bei eindimensionalen Problemen eingesetzt, siehe z.B. [5]. Des Weiteren sind sie sehr flexibel bezüglich des oben angesprochenen Parameters, in dem der

RG-Fluß aufgesetzt wird. Es muß keineswegs ein (künstlicher) Cutoff im Frequenz- und/oder Impulsraum sein. So können auch echte physikalische Parameter wie die Temperatur [6, 7] oder die nackte Wechselwirkung [8] als Flußparameter gewählt werden.

Introduction

Suppose you order a glass of Champagne and the waiter brings you a glass of mineral water. A lawyer may call this fraud. A mathematician may call it an error. A physicist will probably call it an approximation.

Superconductivity and magnetism are central phenomena in solid state physics. Both are macroscopic features of quantum origin, and with the discovery of High- T_c cuprates by Bednorz and Müller in 1986 [9] their importance has grown even more. The High- T_c cuprates are crystalline materials with a layered structure. The electronic movement in the z -direction is strongly suppressed, and the dynamics of electrons is mainly restricted to copper-oxide planes. Generically, these materials can exhibit antiferromagnetism and/or superconductivity, depending on the detailed chemical composition and external parameters. The big puzzle are the high superconducting transition temperatures of up to 130 Kelvin in these compounds. After more than 15 years of intense theoretical and experimental effort a coherent and conclusive description remains to be found. A promising and at the same time controversial model in this context is the Hubbard model. Its three-dimensional version was introduced by Anderson in 1959 to describe super exchange in transition metals [10]. In 1963, Hubbard, Gutzwiller and Kanamori independently invoked it to study correlation effects in the same materials, such as a possible metal-insulator transition and ferromagnetism [11–13]. From its introduction till 1986 the interest in the model was considerable, but not enormous. This changed shortly after the discovery of High- T_c superconductivity, when Anderson proposed the *two*-dimensional Hubbard model (2D-HM), or rather its strong-coupling version, the t - J model, as a potential minimum basis for the theoretical description and understanding of High- T_c compounds [14], a proposition he repeated recently rather strongly [15]. Since then the number of publications concerned with the Hubbard model has increased dramatically. Though simple in its definition, it proves to be quite resistant when it comes to extracting its physical behaviour. While there exists an exact solution for the one-dimensional case [16], up to this day many aspects and features of the model in higher dimensions are either unknown, or not rigorously proven and thus controversial. Many techniques have been used to study the 2D-HM, some of them actually invented with the treatment of this model as the main objective. As a consequence, many results are available, which are useful because they can be compared amongst each other, and because they give us certain ideas about what the physics of the model *could* be. There are also special sets of parameters for which the

model is exactly solvable, or at least for which exact relations hold. It is then possible to try to "expand" around these special parameters. However, a general exact solution is not available to this day, and the effort to learn more about the 2D-HM continues. In this thesis some small steps forward are made in this respect, which are hoped to help understanding the physics of this quite reluctant model.

We will tackle the 2D-HM with a version of the functional renormalisation group (fRG), as proposed by Salmhofer [17]. Starting from exact relations it provides the basis for an approximate treatment which goes beyond many other approaches. Yet, due to the limitations of this approximation it still lacks the accuracy and reliability a physicist should ultimately strive for. Furthermore, in the form we use it, it is restricted to the case of weak electron-electron interaction, while in most real systems of interest this interaction is believed to be larger. Nevertheless, the fRG enables us to make essential and promising steps forward towards a deeper and more reliable understanding of the physics of the 2D-HM. In particular, it opens the gate to systematic improvements of approximations within a rigorous framework, and it has already proven to be very successful in this respect.

This work is closely related to the Ph.D. theses of C. J. Halboth [1] and C. Honerkamp [2], who have applied two different fRG schemes to the 2D-HM. One objective in this thesis is a comparison of these two schemes to estimate the reliability of the results. The main goal is then to extend the calculations in [1] to obtain one-electron properties, namely the one-particle self energy and spectral functions.

The thesis is organised as follows: The two-dimensional Hubbard model and renormalisation-group methods are introduced in the first chapter. The second chapter is concerned with the numerical treatment of the fRG equations and presents the chain of successive approximations which are necessary to conduct calculations on the computer. In the third chapter results for the renormalised two-particle interaction as obtained within the two fRG schemes employed in [1, 18] and [2, 19] are compared. In the fourth chapter the self energy and spectral functions are calculated in the scheme used in [1], and are contrasted to results obtained in second-order perturbation theory. Finally, a discussion and conclusion is offered in the fifth and last chapter.

Chapter 1

Hubbard Model and RG Technique

In this chapter we introduce the two-dimensional Hubbard model and describe the technique of renormalisation-group methods for many-fermion systems, as we will apply them. Our main intention here is to fix the notation and set up the frame within which our calculations are done. We will add comments concerning some of the details, but we shall not give a self-contained introduction, neither to the discussion of the Hubbard model and its validity, nor to renormalisation-group methods in general. This has been done in a very good manner in some of the references which we provide when appropriate.

1.1 The two-dimensional Hubbard Model

The two-dimensional Hubbard model (2D-HM) [10–13] is a quantum-mechanical model for interacting electrons on a two-dimensional square lattice subject to an on-site repulsion U , as illustrated in figure 1.1. The Hamiltonian is given by the sum of a kinetic part \mathcal{H}_0 and an interaction part \mathcal{H}_I :

$$\mathcal{H} = \mathcal{H}_0 + \mathcal{H}_I. \quad (1.1)$$

\mathcal{H}_0 originates from a one-band tight-binding description and reads in second-quantised form

$$\mathcal{H}_0 = -t \sum_{\langle i,j \rangle, \sigma} \psi_{\mathbf{r}_i, \sigma}^\dagger \psi_{\mathbf{r}_j, \sigma} - t' \sum_{\langle\langle i,j \rangle\rangle, \sigma} \psi_{\mathbf{r}_i, \sigma}^\dagger \psi_{\mathbf{r}_j, \sigma}, \quad (1.2)$$

where t describes the hopping of electrons between nearest neighbour sites, and t' the hopping between next-nearest neighbour sites. The operator $\psi_{\mathbf{r}_i, \sigma}^\dagger$ ($\psi_{\mathbf{r}_i, \sigma}$) creates (annihilates) an electron with spin projection σ at site \mathbf{r}_i .

\mathcal{H}_0 is diagonal in momentum space:

$$\mathcal{H}_0 = \sum_{\mathbf{k}, \sigma} \epsilon_{\mathbf{k}}^0 \psi_{\mathbf{k}, \sigma}^\dagger \psi_{\mathbf{k}, \sigma} \quad , \quad (1.3)$$

with the free dispersion

$$\epsilon_{\mathbf{k}}^0 = -2t(\cos k_x + \cos k_y) - 4t' \cos k_x \cos k_y. \quad (1.4)$$

\mathcal{H}_I describes the repulsion between two electrons located at the same site:

$$\mathcal{H}_I = U \sum_i n_{\mathbf{r}_i, \uparrow} n_{\mathbf{r}_i, \downarrow} \quad (1.5)$$

where $n_{\mathbf{r}_i, \sigma} := \psi_{\mathbf{r}_i, \sigma}^\dagger \psi_{\mathbf{r}_i, \sigma}$ is the density operator for spin component σ at lattice site \mathbf{r}_i .

For any operator \mathcal{A} the quantum-statistical average $\langle \mathcal{A} \rangle$ is defined as

$$\langle \mathcal{A} \rangle = \frac{1}{Z} \text{tr} \left(e^{-\beta(\mathcal{H} - \mu \mathcal{N})} \mathcal{A} \right) \quad (1.6)$$

with the partition function $Z = \text{tr} e^{-\beta(\mathcal{H} - \mu \mathcal{N})}$, $\beta = \frac{1}{k_B T}$ and the number operator $\mathcal{N} = \sum_{i, \sigma} n_{\mathbf{r}_i, \sigma}$. The filling n is defined as the average number of particles per lattice site.

For vanishing next-nearest neighbour hopping $t' = 0$ the ground state of the 2D-HM is antiferromagnetic at half filling. It can be driven to a different state in several ways: When the interaction is weak, a finite t' can cause the system to change to a different type of symmetry breaking, such as superconductivity, while keeping the filling fixed at $n = 1$. The same can happen when changing the filling for fixed $t' = 0$ [1, 18], while a sufficiently high temperature can destroy symmetry breaking altogether [2].

While there is consensus that the phase diagram of the 2D-HM is rather rich, there is no consensus on what it precisely looks like. The closeness of antiferromagnetism and d-wave superconductivity near half filling is a feature most experts agree upon, which is particularly nice, since this feature is inherent to the High- T_c cuprates. We shall not enter the discussion on whether the 2D-HM is suitable for the description of High- T_c cuprates, but rather conduct calculations to learn about its behaviour. A discussion concerning the range of applicability

$$\mathcal{H} = \mathcal{H}_0 + \mathcal{H}_I$$

$$\mathcal{H}_0 = \sum_{\mathbf{k}, \sigma} \epsilon_{\mathbf{k}}^0 \psi_{\mathbf{k}, \sigma}^\dagger \psi_{\mathbf{k}, \sigma}$$

$$\mathcal{H}_I = U \sum_i n_{\uparrow}(\mathbf{r}_i) n_{\downarrow}(\mathbf{r}_i)$$

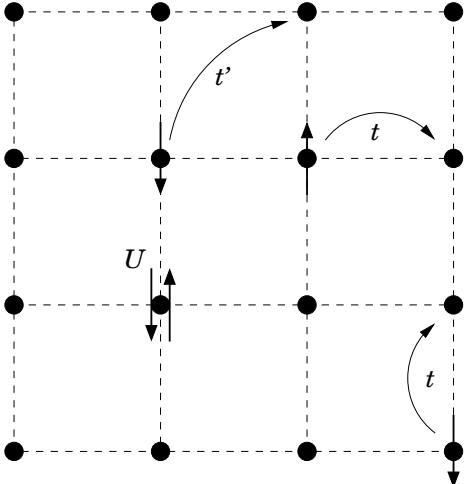
$$\epsilon_{\mathbf{k}}^0 = -2t (\cos k_x + \cos k_y) - 4t' \cos k_x \cos k_y$$


Figure 1.1: The two-dimensional Hubbard model.

of the one-band Hubbard model and its extensions to High- T_c cuprates can be found for example in [20] and [21].

We will be interested in the behaviour of the model near half filling when instabilities are approached from within the normal, i.e. non-symmetry-broken state. The physical observables we will calculate are in chapter 3 the leading correlations and in chapter 4 the influence of these correlations on one-particle properties. We will use functional renormalisation-group (fRG) methods, which are particularly powerful when an unbiased inclusion of several important perturbative contributions is needed, as is the case in the 2D-HM.

We use the common convention of choosing units such that $\hbar = c = k_B = t = 1$. An overview of all relevant parameters is shown in table 1.1.

Symbol	Meaning
t	Nearest neighbour hopping amplitude
t'	Next-nearest neighbour hopping amplitude
μ	Chemical potential
U	Bare on-site interaction
$\epsilon_{vH} := \epsilon_{(0,\pi)}^0$	van Hove energy
$\delta_{vH} := \mu - \epsilon_{vH}$	Distance in energy between Fermi level and van Hove energy
Conventions	$\hbar = c = k_B = t = 1$

Table 1.1: Parameters and conventions

1.2 Functional Description

In order to apply renormalisation-group methods to quantum many-particle systems it is convenient to use functional methods, also known as the path-integral description. In the following we give a short technical overview, mainly to fix the notation and define our terms. A rather detailed introduction to the matter is given for example in [22].

Partition Function and Path Integral

Starting point is the Grassmann path-integral representation of the partition function of a system of electrons subject to a two-particle bare interaction, in the presence of fermionic external fields $(\bar{\eta}, \eta)$:

$$Z[\bar{\eta}, \eta] = \int \mathcal{D}(\bar{\psi}\psi) e^{\mathcal{S}_0 + \mathcal{S}_I + \mathcal{S}_g} \quad (1.7)$$

with

$$\begin{aligned}
\int \mathcal{D}(\bar{\psi}\psi) &= \int \prod_{\zeta} d\bar{\psi}_{\zeta} d\psi_{\zeta} \quad , \\
\mathcal{S}_0 &= \int \int_{\gamma \delta} S_0^{\gamma, \nu} \bar{\psi}_{\gamma} \psi_{\nu} \quad \text{(Gaussian part)} \quad , \\
\mathcal{S}_I &= \int \int_{\alpha \beta} \int \int_{\gamma \delta} S_I^{\alpha, \beta, \gamma, \delta} \bar{\psi}_{\alpha} \bar{\psi}_{\beta} \psi_{\gamma} \psi_{\delta} \quad \text{(Interacting part)} \quad , \\
\mathcal{S}_g &= \int_{\nu} \bar{\eta}_{\nu} \psi_{\nu} - \bar{\psi}_{\nu} \eta_{\nu} \quad \text{(Generating part)} \quad ,
\end{aligned} \tag{1.8}$$

where the fields $\bar{\psi}$ and ψ are Grassmann fields. By differentiating $Z[\bar{\eta}, \eta]$ with respect to $\bar{\eta}_{\nu}$ and η_{ν} , setting $(\bar{\eta}, \eta) = 0$ and then dividing by $Z[0, 0]$, all correlation functions are generated through S_g .¹ In the case of the Hubbard model the Greek indices in momentum representation are given as $\zeta = (i\omega_n, \mathbf{k}, \sigma)$, where $\sigma \in \{\uparrow, \downarrow\}$ denotes the spin index, and we have

$$\begin{aligned}
\int \mathcal{D}(\bar{\psi}\psi) &= \int \prod_{i\omega_n, \mathbf{k}, \sigma} d\bar{\psi}_{(i\omega_n, \mathbf{k}, \sigma)} d\psi_{(i\omega_n, \mathbf{k}, \sigma)} \\
\mathcal{S}_0 &= \int_{(k, \sigma)} (i\omega_n - \xi_{\mathbf{k}}^0) \bar{\psi}_{(i\omega_n, \mathbf{k}, \sigma)} \psi_{(i\omega_n, \mathbf{k}, \sigma)} \\
\mathcal{S}_I &= -U \int_p \int_q \int_r \int_s \delta_{p+q, r+s} \bar{\psi}_{p\uparrow} \bar{\psi}_{q\downarrow} \psi_{r\downarrow} \psi_{s\uparrow} \quad ,
\end{aligned} \tag{1.9}$$

where $k = (i\omega_n, \mathbf{k})$, $\xi_{\mathbf{k}}^0 = \epsilon_{\mathbf{k}}^0 - \mu$, and $\int_{(k, \sigma)}$ is a short-hand notation for $\frac{T}{(2\pi)^d} \sum_{i\omega_n} \sum_{\sigma} \int d^d \mathbf{k}$. The discrete set of Matsubara frequencies $\omega_n = (2n+1)\pi T$ with $n \in \mathbb{Z}$ becomes dense in the limit $T \rightarrow 0$.

It is common to set up a perturbation theory around S_0 in powers of the bare interaction U with the free propagator $C(i\omega_n, \mathbf{k}) := S_0^{-1} = (i\omega_n - \xi_{\mathbf{k}}^0)^{-1}$ as the building block, having the

¹ Strictly speaking, in order to calculate the non-interacting partition function itself it is obligatory to go back to the discrete form of S^0 [22]. As far as correlation functions are concerned, we can use the ‘‘short-hand’’ notation literally.

well-known graphical representation in terms of Feynman graphs. However, several fundamental problems arise when proceeding in this way:

- (1) At $T = 0$ the infrared divergence of $C(i\omega_n, \mathbf{k})$ in the limit $\omega \rightarrow 0$, $\mathbf{k} \rightarrow \mathbf{k}_F$ leads to divergent contributions of individual Feynman graphs, thus yielding an expansion in which some of the coefficients are divergent [23].
- (2) A direct consequence of (1) is the necessity to take Fermi surface shifts into account at zero temperature. The non-interacting system has a Fermi surface defined by $\xi_{\mathbf{k}}^0 = 0$, which in general is not identical to the Fermi surface of the interacting system which is defined by $\xi_{\mathbf{k}_F}^0 + \Sigma(\omega=0, \mathbf{k}_F) = 0$. In order to construct a well-defined perturbation theory, this shift has to be included by expanding around a free system which already possesses the correct Fermi surface [24]. This is equivalent to the requirement that the self energy at zero frequency vanishes everywhere on the Fermi surface, given that the latter has been correctly chosen.
- (3) At small but finite temperature all individual Feynman diagrams give finite contributions, but summing certain infinite subsets, such as ladder or bubble diagrams, can cause the expansion to diverge, provided that the interaction is strong enough. In the case of the 2D-HM near half filling such singularities can appear in several different “channels”, leading to a multiplicity of possible types of broken symmetry. It is one of the main advantages of the fRG to treat all channels simultaneously on equal footing.

The last two problems arise because the attempt is made to set up a perturbation series with the non-symmetry-broken state as the starting point, and the divergences reflect the fact that the system tends to a state of broken symmetry. If we expand around a system which already takes the correct broken symmetry into account, things will become (almost) regular.² For instance, in the superconducting phase the expectation value $\Delta = \langle \psi_{k,\uparrow} \psi_{-k,\downarrow} \rangle$ acquires a finite, non-zero value, and in order to construct a well-defined perturbation theory it is necessary to expand with respect to a quadratic action S_0^Δ which already incorporates the superconducting state [25].

We note that in two dimensions a continuous symmetry cannot be broken at non-zero temperature, as is known from the Mermin-Wagner theorem [26]. However, the inclusion of a

²Except for possible Goldstone modes.

small but finite hopping in the z direction suffices to allow for it. The calculations done in this work, just like the ones in [1] and [2], do not account for this. Instead, they yield critical temperatures of the mean-field type, which is one of the major drawbacks of the approximation. We shall keep this in mind when interpreting the results in chapters 3 and 4.

1.3 Renormalisation-Group Methods

Since Wilson's work in the 1970s (see for example [3]) RG methods have extensively and successfully been applied in many areas of theoretical physics, such as high-energy physics, critical phenomena and polymer systems. The RG concept has proven to be extremely useful, and since its introduction it has continuously been improved and extended. Nowadays, there exist many versions and adaptations of this concept, one of which is the *exact functional renormalisation group* (fRG) [17,27], which we use. With respect to systems of interacting fermions it provides a rigorous tool to connect the low-energy properties, essential for phenomenological descriptions, to the underlying microscopic model. For instance, Feldman et al. used it to construct a *rigorous* proof of the existence of a true Fermi liquid at $T = 0$ under certain conditions [24].

The fRG enables us to investigate properties of interacting Fermi systems, in particular the 2D-HM, with a lack of bias as compared to other methods. It maps the original model, which describes the interaction between all degrees of freedom, to one in which energy scales are separated, and the influence of high-energy degrees of freedom on the low-energy degrees of freedom, namely the states near the Fermi surface, is obtained in a continuous manner by changing the separation scale. The way we shall apply the fRG it is a perturbative approach, since it is implemented on an approximate level valid only in the weak-coupling limit.

The generic starting point in the derivation of fRG equations is the introduction of an additional energy-scale parameter, which regularises the theory and provides us with a well-defined starting point. By varying this parameter, the original model is approached in a way which treats competing perturbative channels on equal footing. Finally, either the low-energy properties of the system are obtained, or divergences appear at a finite energy scale. While such divergences have the same interpretation as in perturbation theory – they signal the appearance of strong correlations and the potential onset of symmetry breaking and/or Fermi-surface deformations – the information on the actual *type* of singularity can be expected to be much less biased within the fRG, as compared to the direct application of perturbation theory.

It is common to choose the scale parameter in a way which takes the separation of energy scales literally. We do this by using a sharp cutoff Λ in momentum space as in [1] and define

$$C_\Lambda(k) = \frac{\Theta(|\xi_{\mathbf{k}}^0| - \Lambda)}{i\omega_n - \xi_{\mathbf{k}}^0} = \Theta(|\xi_{\mathbf{k}}^0| - \Lambda) C(k). \quad (1.10)$$

The free propagator is the building block of all Feynman diagrams, and by removing its largest contributions, the cutoff Λ provides a regular theory as the starting point. In the limit $\Lambda \rightarrow 0$ we have $C_\Lambda \rightarrow C$, and we obtain the properties of the system of interest. More specific information on the fRG machinery is given in the following sections.

Generating Functionals and fRG Schemes

The physics of many-particle systems is encoded in correlation functions, also known as Green functions. There are different types of Green functions, each associated with a specific generating functional, as shown in figure 1.2. By introducing a cutoff, the generating functionals and the corresponding Green functions become scale dependent. First, the cutoff in equation 1.10 will be chosen such that all momenta are cut out, and the initial values of all Green functions are known. Upon varying the cutoff continuously they evolve according to a differential equation called renormalisation-group equation (RGE). The form of the RGE depends on the functional we choose, but if it is solved *exactly*, we recover the same physics in all cases. This is where the trouble starts: In practice it is not possible to solve any RGE exactly. Approximations have to be made, and it is the properties of these approximations which makes us choose a specific functional for practical purposes.

General fRG Setup

Each functional \mathcal{G}^X can be expressed in terms of the corresponding Green functions G_{2n}^X :

$$\mathcal{G}^X[\bar{\eta}, \eta] = \sum_n \frac{1}{(n!)^2} G_{2n}^X(\alpha_1, \dots, \alpha_n, \beta_n, \dots, \beta_1) \bar{\eta}_{\alpha_1} \dots \bar{\eta}_{\alpha_n} \eta_{\beta_n} \dots \eta_{\beta_1} \quad (1.11)$$

where summation over the internal indices α_i and β_i is implied. Inversely, a $2n$ -point Green function is obtained by differentiating the associated functional with respect to the source

Functional	Generated Green functions
$\mathcal{G}^c[\bar{\eta}, \eta] = \log \left(Z_0^{-1} \int \mathcal{D}(\bar{\psi}, \psi) e^{S_0 + S_I + S_g} \right)$	Connected Green functions
$\mathcal{G}^{ac}[\bar{\eta}, \eta] = \log \left(Z_0^{-1} \int \mathcal{D}(\bar{\psi}, \psi) e^{S_0[\bar{\psi}, \psi]} e^{S_I[\bar{\psi}-\bar{\eta}, \psi+\eta]} \right)$	C -amputated, connected Green functions
$\mathcal{G}^{irr}[\bar{\chi}, \chi] = \mathcal{G}^c[\bar{\eta}, \eta] - (\bar{\eta} \chi) + (\bar{\chi} \eta)$ $\bar{\chi} = \langle \bar{\psi} \rangle = \frac{\delta \mathcal{G}^c}{\delta \bar{\eta}}$ $\chi = \langle \psi \rangle = \frac{\delta \mathcal{G}^c}{\delta \eta}$	One-particle irreducible vertex functions

Table 1.2: Different types of generating functionals

fields and then setting the source fields to zero:

$$G_{2n}^X(\alpha_1, \dots, \alpha_n, \beta_n, \dots, \beta_1) := (-1)^n \frac{\delta}{\delta \bar{\eta}_{\alpha_1}} \dots \frac{\delta}{\delta \bar{\eta}_{\alpha_n}} \frac{\delta}{\delta \eta_{\beta_n}} \dots \frac{\delta}{\delta \eta_{\beta_1}} \mathcal{G}^X[\bar{\eta}, \eta] \Big|_{[\bar{\eta}, \eta]=0}, \quad (1.12)$$

with $X \in \{c, ac, irr\}$ (cf. table 1.2). The factor $(-1)^n$ accounts for the n permutations which are needed to put the fields in the correct order.

With the introduction of the cutoff Λ the functions G_{2n}^X become scale-dependent:

$$G_{2n}^X(\alpha_1, \dots, \alpha_n, \beta_n, \dots, \beta_1) \rightarrow G_{2n}^X(\Lambda | \alpha_1, \dots, \alpha_n, \beta_n, \dots, \beta_1). \quad (1.13)$$

The RGE describes the evolution of these functions when Λ is continuously changed:

$$\partial_\Lambda G_{2n}^X(\Lambda | \alpha_1, \dots, \alpha_n, \beta_n, \dots, \beta_1) = R^X[G_{2m}^X(\Lambda | \alpha_1, \dots, \alpha_m, \beta_m, \dots, \beta_1); m = 1 \dots \infty]. \quad (1.14)$$

The right-hand side (RHS) is a functional of all $2m$ -point correlation functions, and the RGE constitutes an infinite hierarchy of coupled, non-linear functional integro-differential equations. In practice, this hierarchy has to be truncated, and many further approximations have to be made in order to prepare the RGE for numerical treatments.

In the following we give a brief overview of different fRG schemes, including references relevant to the 2D-HM, and some short comments.

RGE for One-particle Irreducible Vertex Functions

The RGE for the one-particle irreducible (1-PI) vertex functions [28–30] has been used extensively in the last years to investigate properties of low-dimensional Fermi systems [2, 19, 31–38]. In this scheme the infinite hierarchy is usually truncated by setting the six-point function to zero and keeping two and four-point functions. It has the advantage that the flow of all $2m$ -point functions is regular in the sense that no jumps or discontinuities appear. Therefore, if the flow indicates a deviation from Fermi-liquid behaviour, it does this in a continuous manner at all levels of approximation. However, it has drawbacks on the technical side when applied to the 2D-HM, some of which will be discussed in chapter 3 where we compare results obtained from the 1-PI scheme to results from the Wick-ordered scheme, which is introduced below.

RGE for C-amputated, Connected Green Functions

Polchinski introduced the flow of \mathcal{G}_Λ^{ac} , the generating functional for the C -amputated, connected Green functions, and applied it to the four-dimensional ϕ^4 theory [39]. An appealing feature of this fRG scheme is the fact that at each scale Λ the functional \mathcal{G}_Λ^{ac} not only generates the Green functions for the system with cutoff Λ , but at the same time constitutes the effective action for the complementary degrees of freedom, i.e. the ones which have not been “integrated out”.

In its functional form the Polchinski equation reads

$$\partial_\Lambda \mathcal{G}_\Lambda^{ac} = -\Delta_{\dot{C}_\Lambda} \mathcal{G}_\Lambda^{ac} - \left(\frac{\delta \mathcal{G}_\Lambda^{ac}}{\delta \eta} \middle| \dot{C}_\Lambda \middle| \frac{\delta \mathcal{G}_\Lambda^{ac}}{\delta \bar{\eta}} \right) \quad (1.15)$$

where $\dot{C} := \partial_\Lambda C_\Lambda$, and $\Delta_X := (\delta_\eta | X | \delta_{\bar{\eta}})$ is the functional Laplacian with respect to X . In the context of interacting electron systems it was employed by Zanchi and Schulz, who used it to

investigate the 2D-HM [40–42]. In this scheme, the six-point function needs to be taken into account already at one-loop order, and the hierarchy is truncated at the level of the eight-point function. The Polchinski equation is somewhat difficult to handle, since the numerical procedure to solve the RGE is non-local in Λ already at one-loop level. However, it has the advantage that the calculated entity has a straightforward physical interpretation. The reader may refer to [42] and further references therein for a more detailed discussion.

RGE for Wick-ordered C-amputated, Connected Green Functions

Starting from the Polchinski equation, Wiczerkowski formulated an RGE for Wick-ordered C-amputated, connected Green functions [43]. This can be done by defining

$$D_\Lambda = C - C_\Lambda = \frac{1 - \Theta(|\xi_{\mathbf{k}}^0| - \Lambda)}{i\omega_n - \xi_{\mathbf{k}}^0} = \frac{\Theta(\Lambda - |\xi_{\mathbf{k}}^0|)}{i\omega_n - \xi_{\mathbf{k}}^0}, \quad (1.16)$$

and introducing a new functional \mathcal{G}_Λ^w by

$$\mathcal{G}_\Lambda^w := e^{-\Delta_{D_\Lambda}} \mathcal{G}_\Lambda^{ac}. \quad (1.17)$$

The RGE for this functional, which we will call Wiczerkowski equation, reads

$$\partial_\Lambda \mathcal{G}_\Lambda^w = e^{-\Delta_{D_\Lambda}} \left(\frac{\delta(e^{\Delta_{D_\Lambda}} \mathcal{G}_\Lambda^w)}{\delta\eta} \Big| \dot{D}_\Lambda \Big| \frac{\delta(e^{\Delta_{D_\Lambda}} \mathcal{G}_\Lambda^w)}{\delta\bar{\eta}} \right). \quad (1.18)$$

Figure 1.2 shows the diagrammatic representation of the flow of the two- and four-point functions, when the hierarchy of equations is truncated by setting the six-point function to zero. This scheme has been used by Halboth and Metzner to tackle the 2D-HM [1, 18, 44], and also by Chauve and Le Doussal in the context of classical systems with disorder [45]. Unlike the Polchinski equation, the Wiczerkowski equation does not contain tadpoles on the right-hand side, which is an advantage. However, it is also evident from figure 1.2 that the RHS generally contains one-particle *reducible* terms, which are inconvenient for our purposes, and some of which can be removed by switching to yet another set of $2n$ -point functions, which leads to the scheme we will use.

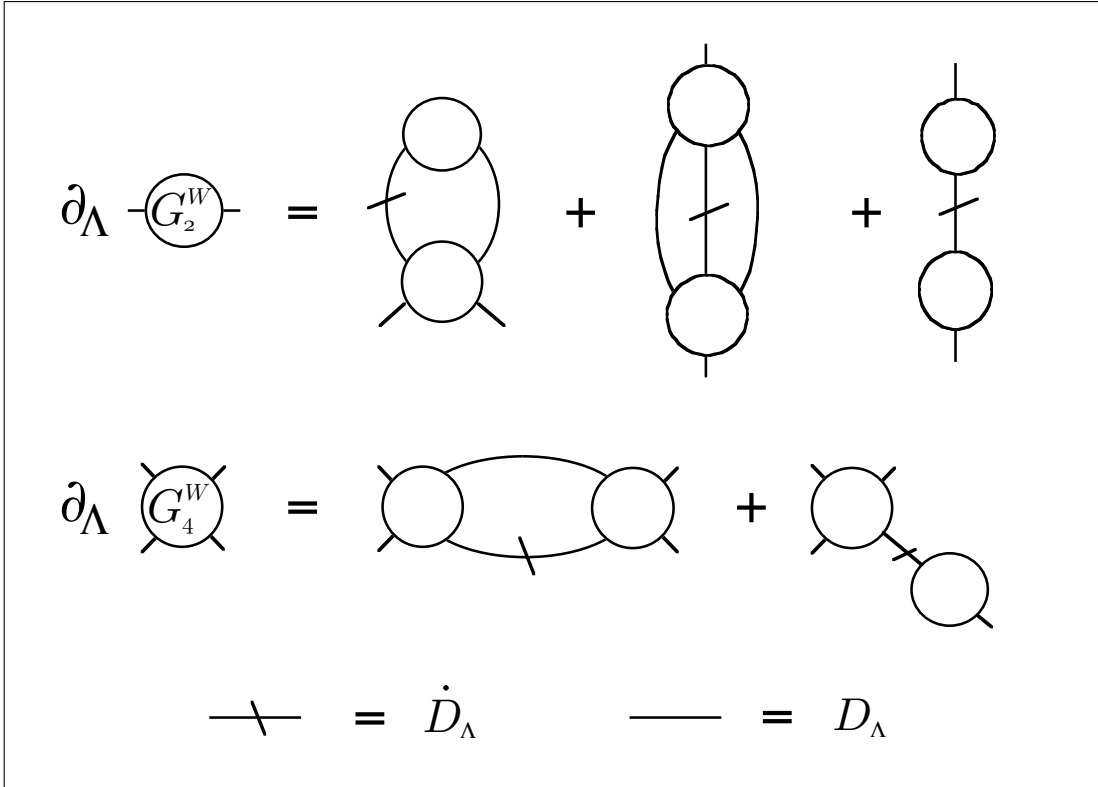


Figure 1.2: Graphical representation of the Wiczerkowski equation, truncated by setting the six-point function to zero on the right-hand side. Normal internal lines correspond to D_Λ , slashed lines to \dot{D}_Λ .

RGE for Fully Amputated, Wick-ordered Connected Correlation Functions

We follow Salmhofer [17] who, starting from the truncated Wiczerkowski equation, introduced new two-point and four-point functions defined as

$$G_2^S(\Lambda) := \frac{G_2^W(\Lambda)}{1 + C_\Lambda G_2^W(\Lambda)} \quad (1.19)$$

and

$$G_4^S(\Lambda | k_1^f, k_2^f; k_2^i, k_1^i) := A_\Lambda(k_1^f) A_\Lambda(k_2^f) G_4^W(\Lambda | k_1^f, k_2^f; k_2^i, k_1^i) A_\Lambda(k_2^i) A_\Lambda(k_1^i), \quad (1.20)$$

with

$$A_\Lambda := (1 - C_\Lambda G_2^S(\Lambda))^{-1}. \quad (1.21)$$

This leads to an RGE with a structure shown in figure 1.3. The flow equation for the two-point function contains only one-particle irreducible contributions, and by construction smoothly

$$\partial_\Lambda \text{---} G_2^S \text{---} = \text{diagram 1} + \text{diagram 2}$$

$$\partial_\Lambda \text{---} G_4^S \text{---} = \text{diagram 3} + \text{diagram 4}$$

$$\text{---} \diagup \text{---} = A_\Lambda \dot{D}_\Lambda A_\Lambda \quad \text{---} \diagdown \text{---} = D_\Lambda \dot{G}_2^S$$

$$\text{---} \text{---} = A_\Lambda D_\Lambda A_\Lambda$$

Figure 1.3: Graphical representation of the Salmhofer equation for fully amputated, Wick-ordered connected correlation functions.

approaches the (one-particle irreducible) self energy in the limit $\Lambda \rightarrow 0$. We note that this RGE is obtained by direct manipulation on the level of Green functions, and not by switching to a new functional. We could, however, define a corresponding functional via equation 1.11, but there is no need for that.

The initial condition of the two-point function can be set to zero by introducing appropriate counter terms.³ To prepare for the application of numerical methods, the equation is further approximated by expanding the RHS to second order in powers of the flowing four-point function $G_4^S(\Lambda|\alpha_1, \dots, \alpha_n, \beta_n, \dots, \beta_1)$. This simplifies the structure of the Salmhofer equation to the one shown in figure 1.4: It removes the one-particle reducible contribution in the flow of the four-point function, and eliminates all feedback effects of the two-point function via internal lines. Thereby, the numerical treatment is greatly simplified.

Due to rotation invariance in spin space and translation invariance in direct space we can write

³In the case of the Hubbard model this is simply the inclusion of the Hartree correction in the chemical potential.

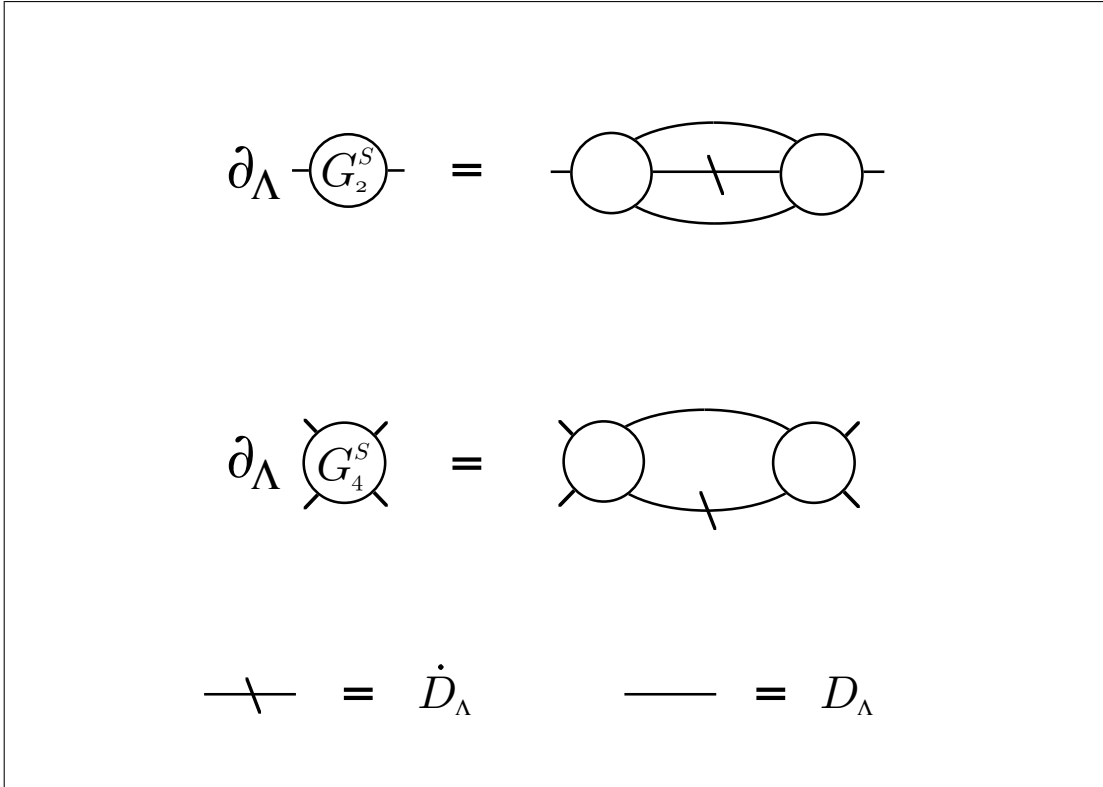


Figure 1.4: Graphical representation of the Salmhofer equation up to second order in the flowing (renormalised) four-point function.

$$G_2^S(\Lambda|\alpha; \beta) = \Sigma_\Lambda(k_\alpha) \delta_{\sigma_\alpha, \sigma_\beta} \delta_{k_\alpha, k_\beta} \quad (1.22)$$

$$\begin{aligned} -G_4^S(\Lambda|\alpha, \beta; \gamma, \delta) &= \Gamma_\Lambda^s(k_\alpha, k_\beta; k_\gamma, k_\delta) \delta_{k_\alpha+k_\beta-k_\gamma, k_\delta} (\delta_{\sigma_\alpha \sigma_\delta} \delta_{\sigma_\beta} \delta_{\sigma_\gamma} - \delta_{\sigma_\alpha \sigma_\gamma} \delta_{\sigma_\beta \sigma_\delta}) \\ &+ \Gamma_\Lambda^t(k_\alpha, k_\beta; k_\gamma, k_\delta) \delta_{k_\alpha+k_\beta-k_\gamma, k_\delta} (\delta_{\sigma_\alpha \sigma_\delta} \delta_{\sigma_\beta} \delta_{\sigma_\gamma} + \delta_{\sigma_\alpha \sigma_\gamma} \delta_{\sigma_\beta \sigma_\delta}) \end{aligned} \quad (1.23)$$

where the minus sign is introduced for convenience, since it makes the initial condition for Γ coincide with the bare Hubbard interaction U . This singlet-triplet representation, with a slightly different choice of pre-factors, is also used in [1].⁴ We will use the Salmhofer equation written in terms of Σ_Λ and $\Gamma_\Lambda^{s,t}$. At the level of approximation we use here, the flow of the four-point function is identical to the flow in the Wiczerkowski scheme used in [1].

⁴This is not the only possible way to separate spatial and spin parts. In [2] a different choice is made.

The explicit expressions for the flow of Σ_Λ , Γ_Λ^s and Γ_Λ^t are

$$\begin{aligned} \frac{\partial}{\partial \Lambda} \Sigma_\Lambda(k) &= \int_{p_1, p_2} \left[(\Gamma_\Lambda^s(p_1, p_2; p_1 + p_2 - k, k))^2 + 3 (\Gamma_\Lambda^t(p_1, p_2; p_1 + p_2 - k, k))^2 \right] \\ &\quad \frac{\partial}{\partial \Lambda} (D_\Lambda(p_1) D_\Lambda(p_2) D_\Lambda(p_1 + p_2 - k)) \end{aligned} \quad (1.24)$$

$$\begin{aligned} \frac{\partial}{\partial \Lambda} \Gamma_\Lambda^s(k_1^i, k_2^i; k_2^f, k_1^f) &= PP_\Lambda^s(k_1^i, k_2^i; k_2^f, k_1^f) + PH_\Lambda^s(k_1^i, k_2^i; k_2^f, k_1^f) + PH_\Lambda^s(k_1^i, k_2^i; k_1^f, k_2^f) \\ \frac{\partial}{\partial \Lambda} \Gamma_\Lambda^t(k_1^i, k_2^i; k_2^f, k_1^f) &= PP_\Lambda^t(k_1^i, k_2^i; k_2^f, k_1^f) - PH_\Lambda^t(k_1^i, k_2^i; k_2^f, k_1^f) + PH_\Lambda^t(k_1^i, k_2^i; k_1^f, k_2^f), \end{aligned} \quad (1.25)$$

where

$$\begin{aligned} PP_\Lambda^{s,t}(k_1^i, k_2^i; k_2^f, k_1^f) &= \sum_{i,j} I_{i,j}^{s,t} \int_p \Gamma_\Lambda^i(k_1^i, k_2^i; p, k_1^i + k_2^i - p) \Gamma_\Lambda^j(k_1^i + k_2^i - p, p; k_1^i + k_2^i - k_1^f, k_1^f) \\ &\quad \frac{\partial}{\partial \Lambda} (D_\Lambda(p) D_\Lambda(k_1^i + k_2^i - p)), \end{aligned} \quad (1.26)$$

$$\begin{aligned} PH_\Lambda^{s,t}(k_1^i, k_2^i; k_2^f, k_1^f) &= \sum_{i,j} J_{i,j}^{s,t} \int_p \Gamma_\Lambda^i(k_1^i, p; k_1^i + p - k_1^f, k_1^f) \Gamma_\Lambda^j(k_2^i, k_1^i + p - k_1^f; p, k_1^i + k_2^i - k_1^f) \\ &\quad \frac{\partial}{\partial \Lambda} (D_\Lambda(p) D_\Lambda(k_1^i + p - k_1^f)) \end{aligned} \quad (1.27)$$

and

$$\begin{aligned} I_{i,j}^s &= 2 \begin{pmatrix} 1 & 0 \\ 0 & 0 \end{pmatrix} & I_{i,j}^t &= 2 \begin{pmatrix} 0 & 0 \\ 0 & 1 \end{pmatrix} \\ J_{i,j}^s &= \frac{1}{2} \begin{pmatrix} 1 & -3 \\ -3 & -3 \end{pmatrix} & J_{i,j}^t &= \frac{1}{2} \begin{pmatrix} 1 & 1 \\ 1 & 5 \end{pmatrix}. \end{aligned} \quad (1.28)$$

In the following chapters we will describe some important details concerning the numerical treatment of these equations, compare some of the results to those obtained by the RGE for 1-PI vertex functions, and finally calculate self-energy effects and spectral functions from it.

The route from the Polchinski equation to the Wieczerkowski equation is straightforward. In appendix A we outline this procedure and comment on essential steps. The transformations needed to arrive at the final flow equations 1.24 and 1.25 are then purely algebraic and easily obtained by simple substitutions.

It is interesting to note that the one-loop flow defined by equation 1.25 is identical to that derived by Zanchi and Schulz starting from the field-theoretic RG [46].

Chapter 2

Numerical Treatment

Our goal is to solve equations 1.24 and 1.25 numerically. In this chapter we present the approximations we make to bring the complexity of this task to a feasible level. We recall the definition of the cutoff-dependent propagator C_Λ , and the form of the complementary propagator D_Λ :

$$C_\Lambda(k) = \Theta(|\xi_{\mathbf{k}}^0| - \Lambda) C(k) = \frac{\Theta(|\xi_{\mathbf{k}}^0| - \Lambda)}{i\omega_n - \xi_{\mathbf{k}}^0},$$

$$D_\Lambda(k) = C - C_\Lambda = \Theta(\Lambda - |\xi_{\mathbf{k}}^0|) C(k) = \frac{\Theta(\Lambda - |\xi_{\mathbf{k}}^0|)}{i\omega_n - \xi_{\mathbf{k}}^0}.$$

The simple choice of a sharp, frequency-independent cutoff will allow for substantial simplifications of the RHS of equations 1.24 and 1.25.

2.1 Static Approximation

We adopt the common procedure to replace the four-point function Γ by its values at zero frequencies, thus approximating it by its static components. This holds exactly at the beginning of the flow, and is further motivated by the assumption that the frequency dependence of the four-point function becomes irrelevant in the RG sense in the limit $\Lambda \rightarrow 0$. This is also supported by simple power counting arguments [23]. However, we will see that the four-point function can develop singularities which invalidate this assumption at a certain stage. We will comment on this in chapter 3. With the static approximation we have $\Gamma_\Lambda^{s,t}(k_1^f, k_2^f; k_2^i, k_1^i) \rightarrow \Gamma_\Lambda^{s,t}(\mathbf{k}_1^f, \mathbf{k}_2^f; \mathbf{k}_2^i, \mathbf{k}_1^i)$, which simplifies the RHS of equation 1.25 substantially.

Writing $q = (i\nu_n, \mathbf{q})$ and $p = (i\omega_n, \mathbf{p})$ we have $\int_p = \int_{\mathbf{p}} T \sum_{\omega_n}$, and we can pull the four-point function as well as the cutoff functions out of the frequency sum. Equations 1.26 and 1.27 then read

$$\begin{aligned}
PP_{\Lambda}^{s,t}(\mathbf{k}_1^i, \mathbf{k}_2^i; \mathbf{k}_2^f, \mathbf{k}_1^f) = & \\
& \sum_{i,j} I_{i,j}^{s,t} \int_{\mathbf{p}} \Gamma_{\Lambda}^i(\mathbf{k}_1^i, \mathbf{k}_2^i; \mathbf{p}, \mathbf{k}_1^i + \mathbf{k}_2^i - \mathbf{p}) \Gamma_{\Lambda}^j(\mathbf{k}_1^i + \mathbf{k}_2^i - \mathbf{p}, \mathbf{p}; \mathbf{k}_1^f, \mathbf{k}_2^f) \\
& \frac{\partial}{\partial \Lambda} \left(\Theta(\Lambda - |\xi_{\mathbf{p}}^0|) \Theta(\Lambda - |\xi_{\mathbf{k}_1^i + \mathbf{k}_2^i - \mathbf{p}}^0|) \right) T \sum_{\omega_n} \left(C(p) C(k_1^i + k_2^i - p) \right) \quad (2.1)
\end{aligned}$$

and

$$\begin{aligned}
PH_{\Lambda}^{s,t}(\mathbf{k}_1^i, \mathbf{k}_2^i; \mathbf{k}_2^f, \mathbf{k}_1^f) = & \\
& \sum_{i,j} J_{i,j}^{s,t} \int_{\mathbf{p}} \Gamma_{\Lambda}^i(\mathbf{k}_1^i, \mathbf{p}; \mathbf{k}_1^i + \mathbf{p} - \mathbf{k}_1^f, \mathbf{k}_1^f) \Gamma_{\Lambda}^j(\mathbf{k}_2^i, \mathbf{k}_1^i + \mathbf{p} - \mathbf{k}_1^f; \mathbf{p}, \mathbf{k}_1^i + \mathbf{k}_2^i - \mathbf{k}_1^f) \\
& \frac{\partial}{\partial \Lambda} \left(\Theta(\Lambda - |\xi_{\mathbf{p}}^0|) \Theta(\Lambda - |\xi_{\mathbf{k}_1^i + \mathbf{p} - \mathbf{k}_1^f}^0|) \right) T \sum_{\omega_n} \left(C(p) C(k_1^i + p - k_1^f) \right) . \quad (2.2)
\end{aligned}$$

The frequency sums can be carried out explicitly using the relations [47]

$$T \sum_{\omega_n} C(i\omega_n, \mathbf{p}) C(i\nu_n - i\omega_n, \mathbf{q} - \mathbf{p}) = \frac{f(\xi_{\mathbf{p}}^0) - f(\xi_{\mathbf{q}-\mathbf{p}}^0)}{i\nu_n - \xi_{\mathbf{p}}^0 - \xi_{\mathbf{q}-\mathbf{p}}^0} \quad (2.3)$$

$$T \sum_{\omega_n} C(i\omega_n, \mathbf{p}) C(i\nu_n + i\omega_n, \mathbf{q} + \mathbf{p}) = \frac{f(\xi_{\mathbf{p}}^0) - f(\xi_{\mathbf{q}+\mathbf{p}}^0)}{i\nu_n + \xi_{\mathbf{p}}^0 - \xi_{\mathbf{q}+\mathbf{p}}^0} \quad (2.4)$$

$$T \sum_{\omega_n} C(i\omega_n, \mathbf{p}) C(i\omega_n, \mathbf{p}) = f'(\xi_{\mathbf{p}}^0) . \quad (2.5)$$

The last equation is understood as the limit $\mathbf{q} \rightarrow \mathbf{0}$ after $\nu_n \rightarrow 0$ of the second equation and applies to the forward channel.¹ The three-dimensional integration/summation over the internal variable p has been reduced to a two-dimensional one over \mathbf{p} , and due to the sharp cutoff

¹ In the case $t' = 0$ and $\mu = 0$ the third equation is also relevant for $\mathbf{q} = (\pi, \pi)$.

it can be further simplified to a one-dimensional one due to the relation $\partial_\Lambda \Theta(\Lambda - a) = \delta(\Lambda - a)$. Therefore, by switching from (p_x, p_y) to a new set of variables $(\tilde{\xi}, \tilde{\lambda})$ with an energy variable $\tilde{\xi}$ and an angular variable $\tilde{\lambda}$, the integration over $\tilde{\xi}$ can be carried out immediately, and we are left with a one-dimensional integration over $\tilde{\lambda}$, which we choose to be p_y .

An analogous procedure to the one outlined here for the flow of the four-point function is used in chapter 4 in the calculation of the two-point function.

2.2 Discretisation of the Brillouin Zone

In order to solve the simplified form of equations 2.1 and 2.2 numerically we have to reduce the values which the arguments in the four-point function can take from un-countably many to a finite number, an obvious necessity when using computational methods. Concerning the momentum coordinates we use momentum conservation and discretise the Brillouin zone (BZ) and with it the Fermi surface, thereby further reducing the four-point function $\Gamma_\Lambda^{s,t}(\mathbf{k}_1^f, \mathbf{k}_2^f; \mathbf{k}_2^i, \mathbf{k}_1^i)$ to a function $V_\Lambda^{s,t}(i, j; l)$ defined on a discrete and finite set of patches, or, to be more precise, on a finite set of patch points on the non-interacting Fermi surface. This procedure is not unique, and differences in the discretisation may influence the results. While it is not possible to conduct a complete check with respect to this issue, it is imperative to investigate it to at least some extent. We will do this in the last section of this chapter by considering two discretisations, depicted in figure 2.1. In both cases patch points are put on the Fermi surface only. In one case (left picture) the BZ is patched along the axes as well as the diagonals, meaning that some of the patch points lie on these symmetry axes. In the other case (right picture) the discretisation avoids patches on axes and diagonals, such that no patch point is on a symmetry axis. To complete the definition of the discretisation, we have to specify the number of patches we use, as well as the size of their area, which in the following is always chosen to be equal for all patches. The points on the Fermi surface are chosen such that a straight line either from the origin or from (π, π) through the patch point to the Umklapp surface defined by $|k_y| = \pi - |k_x|$ splits the corresponding patch into two parts of equal size, as illustrated in figure 2.1.

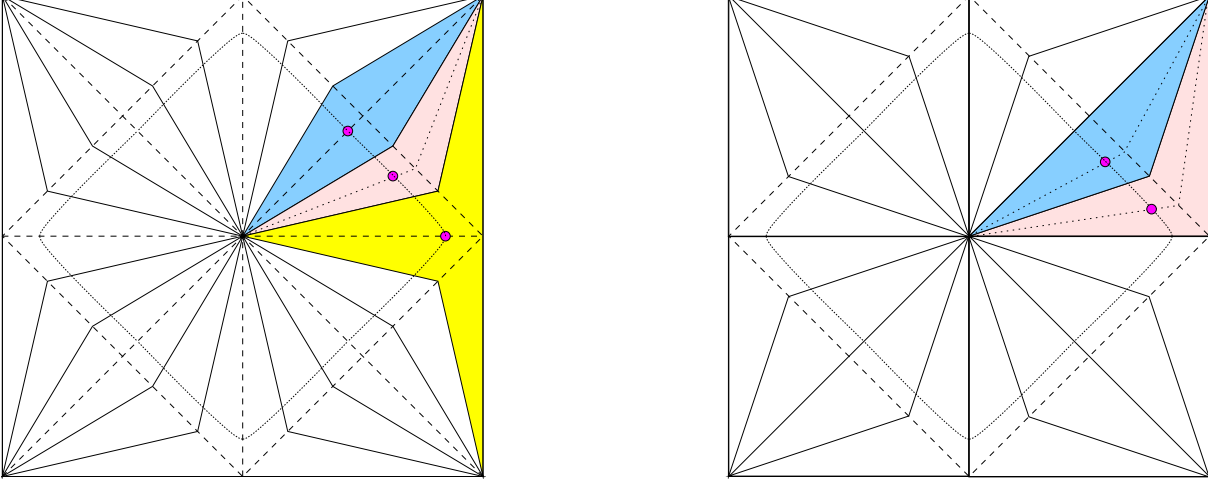


Figure 2.1: The two patching schemes we consider - in the on-axes scheme (left) patch points are allowed to sit on the axes and the diagonals, while in the off-axes scheme (right) no patch points are located on axes and diagonals (right).

2.3 External vs Internal Projection

There exists an ambiguity when replacing Γ by V . We denote by $\mathcal{P}(\mathbf{p}) = i(\mathbf{p})$ the mapping of \mathbf{p} to the number of the patch it is located in, with the corresponding patch momentum \mathbf{p}_i on the Fermi surface. To understand how this enters in the RHS of equations 2.1 and 2.2, consider as an example a contribution to PP_Λ^s on the RHS of equation 1.26 of the form

$$\int_p \Gamma_\Lambda^s(\mathbf{k}_i, \mathbf{k}_j; \mathbf{p}, \mathbf{q} - \mathbf{p}) \Gamma_\Lambda^s(\mathbf{q} - \mathbf{p}, \mathbf{p}; \mathbf{q} - \mathbf{k}_l, \mathbf{k}_l) \dot{D}_\Lambda(p) D_\Lambda(q - p), \quad (2.6)$$

where $q := k_i + k_j$. The differentiated propagator $\dot{D}_\Lambda(p)$ is fixed at $\xi_{\mathbf{p}}^0 = \pm\Lambda$ due to the sharp cutoff, and the external momenta $\mathbf{k}_i, \mathbf{k}_j$ and \mathbf{k}_l are the patch momenta on the Fermi surface associated with the patches i, j and l .

The four-point function Γ^s (Γ^t) is symmetric (antisymmetric) under the exchange of two incoming or outgoing momenta. Therefore we can replace $\Gamma_\Lambda^s(\mathbf{q} - \mathbf{p}, \mathbf{p}; \mathbf{q} - \mathbf{k}_l, \mathbf{k}_l)$ by $\Gamma_\Lambda^s(\mathbf{q} - \mathbf{p}, \mathbf{p}; \mathbf{k}_l, \mathbf{q} - \mathbf{k}_l)$, and analogously $\Gamma_\Lambda^t(\mathbf{q} - \mathbf{p}, \mathbf{p}; \mathbf{q} - \mathbf{k}_l, \mathbf{k}_l)$ by $-\Gamma_\Lambda^t(\mathbf{q} - \mathbf{p}, \mathbf{p}; \mathbf{k}_l, \mathbf{q} - \mathbf{k}_l)$. To switch from Γ to V in equation 2.6 we can then set

$$\begin{aligned}
& \int_p \Gamma_\Lambda^s(\mathbf{k}_i, \mathbf{k}_j; \mathbf{p}, \mathbf{q} - \mathbf{p}) \Gamma_\Lambda^s(\mathbf{q} - \mathbf{p}, \mathbf{p}; \mathbf{k}_l, \mathbf{q} - \mathbf{k}_l) \dot{D}_\Lambda(p) D_\Lambda(q - p) \\
& \approx \int_p V_\Lambda^s(i, j; \mathcal{P}(\mathbf{p})) V_\Lambda^s(\mathcal{P}(\mathbf{q} - \mathbf{p}), \mathcal{P}(\mathbf{p}); l) \dot{D}_\Lambda(p) D_\Lambda(q - p) \quad , \quad (2.7)
\end{aligned}$$

meaning that \mathbf{p} is projected in both $\Gamma_\Lambda^s(\mathbf{k}_i, \mathbf{k}_j; \mathbf{p}, \mathbf{q} - \mathbf{p})$ and $\Gamma_\Lambda^s(\mathbf{q} - \mathbf{p}, \mathbf{p}; \mathbf{k}_l, \mathbf{q} - \mathbf{k}_l)$, while in $\Gamma_\Lambda^s(\mathbf{q} - \mathbf{p}, \mathbf{p}; \mathbf{k}_l, \mathbf{q} - \mathbf{k}_l)$ also the second internal loop variable $\mathbf{q} - \mathbf{p}$ is projected. In the Wick-ordered scheme this approximation is exact in the limit $\Lambda \rightarrow 0$ and infinitely many patches, due to the contraction of the support of the complementary propagator D_Λ around the Fermi surface. We call it internal projection and will use it throughout the whole work.

Alternatively, instead of $\mathbf{q} - \mathbf{p}$ we could in $\Gamma_\Lambda^s(\mathbf{q} - \mathbf{p}, \mathbf{p}; \mathbf{k}_l, \mathbf{q} - \mathbf{k}_l)$ project the fourth external variable $\mathbf{q} - \mathbf{k}_l$. Using time-reversal and conjugation symmetry, which tells us that $\Gamma_\Lambda^{s,t}(\mathbf{q} - \mathbf{p}, \mathbf{p}; \mathbf{k}_l, \mathbf{q} - \mathbf{k}_l) = \Gamma_\Lambda^{s,t}(\mathbf{q} - \mathbf{k}_l, \mathbf{k}_l; \mathbf{p}, \mathbf{q} - \mathbf{p})$ [1], we then have the replacement

$$\begin{aligned}
& \int_p \Gamma_\Lambda^s(\mathbf{k}_i, \mathbf{k}_j; \mathbf{p}, \mathbf{q} - \mathbf{p}) \Gamma_\Lambda^s(\mathbf{q} - \mathbf{p}, \mathbf{p}; \mathbf{k}_l, \mathbf{q} - \mathbf{k}_l) \dot{D}_\Lambda(p) D_\Lambda(q - p) \\
& \approx \int_p V_\Lambda^s(i, j; \mathcal{P}(\mathbf{p})) V_\Lambda^s(\mathcal{P}(\mathbf{q} - \mathbf{k}_l), l; \mathcal{P}(\mathbf{p})) \dot{D}_\Lambda(p) D_\Lambda(q - p) \quad (2.8)
\end{aligned}$$

as done in [1].² This external projection is less favourable in the Wick-ordered scheme, since $\mathbf{q} - \mathbf{k}_l$ is not restricted to a small stripe around the Fermi surface when the cutoff becomes small. Thus, this choice of projection does *not* become exact in the limit $\Lambda \rightarrow 0$ and infinitely many patches.

In the particle-hole channel the procedure is analogous. Consider, again as an example, a contribution to PH_Λ^s on the RHS of equation 1.27 of the form

$$\int_p \Gamma_\Lambda^s(\mathbf{k}_i, \mathbf{p}; \mathbf{p} + \mathbf{q}, \mathbf{k}_l) \Gamma_\Lambda^s(\mathbf{k}_j, \mathbf{p} + \mathbf{q}; \mathbf{p}, \mathbf{q} + \mathbf{k}_j) \dot{D}_\Lambda(p) D_\Lambda(p + q) \quad , \quad (2.9)$$

²C. J. Halboth, private communication - which type of projection is actually used is not explicitly stated in [1].

where $q := k_i - k_l$. We again use the symmetry under exchange of two outgoing momenta to replace $\Gamma_\Lambda^s(\mathbf{k}_i, \mathbf{p}; \mathbf{p} + \mathbf{q}, \mathbf{k}_l)$ by $\Gamma_\Lambda^s(\mathbf{k}_i, \mathbf{p}; \mathbf{k}_l, \mathbf{p} + \mathbf{q})$, and then project \mathbf{p} . In $\Gamma_\Lambda^s(\mathbf{k}_j, \mathbf{p} + \mathbf{q}; \mathbf{p}, \mathbf{q} + \mathbf{k}_j)$ we project \mathbf{p} as well as $\mathbf{p} + \mathbf{q}$ and we have

$$\begin{aligned} & \int_p \Gamma_\Lambda^s(\mathbf{k}_i, \mathbf{p}; \mathbf{k}_l, \mathbf{p} + \mathbf{q}) \Gamma_\Lambda^s(\mathbf{k}_j, \mathbf{p} + \mathbf{q}; \mathbf{p}, \mathbf{q} + \mathbf{k}_j) \dot{D}_\Lambda(p) D_\Lambda(p + q) \\ & \approx \int_p V_\Lambda^s(i, \mathcal{P}(\mathbf{p}); l) V_\Lambda^s(j, \mathcal{P}(\mathbf{p} + \mathbf{q}); \mathcal{P}(\mathbf{p})) \dot{D}_\Lambda(p) D_\Lambda(p + q) \quad . \end{aligned}$$

We omit the expression for the case of external projection, since it is completely analogous to the particle-particle case, and we will not need it in the following.

We shall mention here that we have made several checks regarding the impact of the projection scheme on the results. We did not observe substantial differences, thus the results in [1] are by no means questioned here. However, in this work we stick to the internal projection since it is favourable *a priori*.

2.4 Integrating the RGE

With these specifications we integrate the flow equation numerically using an implicit, adaptive Runge-Kutta method provided in [48], which we slightly adapted to our needs. We verified throughout the calculations that changes in our choice of parameters entering the Runge-Kutta method do not lead to relevant quantitative changes in the results. An overview of the steps that we make to treat the RGE numerically is shown in table 2.1.

2.5 How Many Patches Do We Need?

We can now turn to the question raised at the beginning of this chapter concerning the potential influence of different discretisation schemes on the results. While the two discretisation procedures presented in the previous sections are equivalent in the limit of infinitely high resolution, that is the limit of infinitely many patches, we have to restrict ourselves to a finite number, and we want to find out which discretisation scheme requires the fewest patches.

Numerical Solution of RGE - Overview

- (1) Choose representation of spin structure of four-point function (here: singlet-triplet)
- (2) Drop frequency dependence in four-point function
- (3) Discretise and patch BZ (here: linear and off-axis)
- (4) Choose internal or external projection (here: internal)
- (5) Integrate RG equation specifying the method (here: adaptive, implicit Runge-Kutta)

Table 2.1: The RG recipe

We do this by looking at the dependence of the flow of the four-point function on the number of patches as well as on the discretisation scheme, i.e. on-axes or off-axes.

At small temperatures and in the parameter range of interest the four-point function diverges when the cutoff approaches a certain value Λ_c , indicating that the true state of the system may qualitatively differ from the non-symmetry-broken state we started from. The physical implications of this behaviour will be discussed in more detail in the next chapter. Here, we are interested only in the technical question concerning the patching procedure. We set the temperature to $T = 0.01$, the next-nearest neighbour hopping to $t' = -0.1$ and the bare interaction to $U = 2.0$. We calculate the flow for different values of $\delta_{vH} := \epsilon_{vH} - \mu$, stopping the flow when the largest value of the four-point function exceeds 100. We call the corresponding cutoff scale Λ_{100} . Figure 2.2 shows Λ_{100} as a function of δ_{vH} for different numbers of patches N per octand in the two different types of discretisation mentioned above. We see that for $N = 6$ on-axes and off-axes results agree reasonably well with each other. For smaller values of N the off-axes scheme is qualitatively stable in the sense that it always yields the maximum value of Λ_{100} for the same value of δ_{vH} . In contrast, the on-axes scheme for $N = 3$ predicts the largest value of Λ_{100} to be at van Hove filling. Only using more patches cures this artefact.

We use these results as a hint that the off-axes scheme is favourable since it is more stable regarding the qualitative aspects. We always stick to $N = 6$, unless explicitly stated otherwise. In figure 2.3 the numbering scheme of patches is shown as it will be used in the following chapters. The numbering convention is somewhat counter-intuitive for technical reasons.

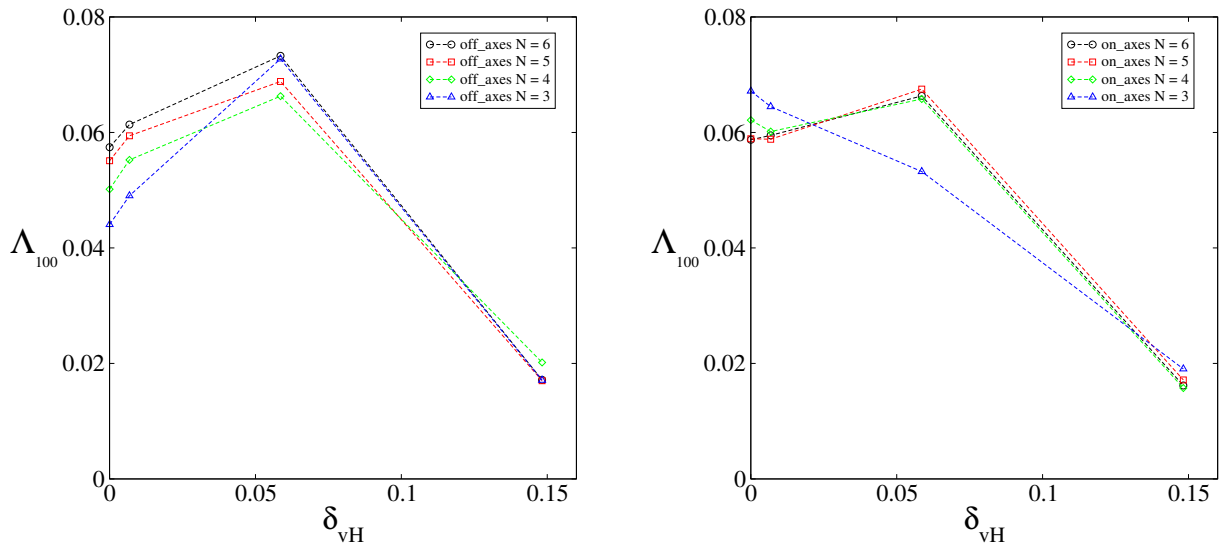


Figure 2.2: Comparison between off-axis and on-axis schemes for different numbers of patches

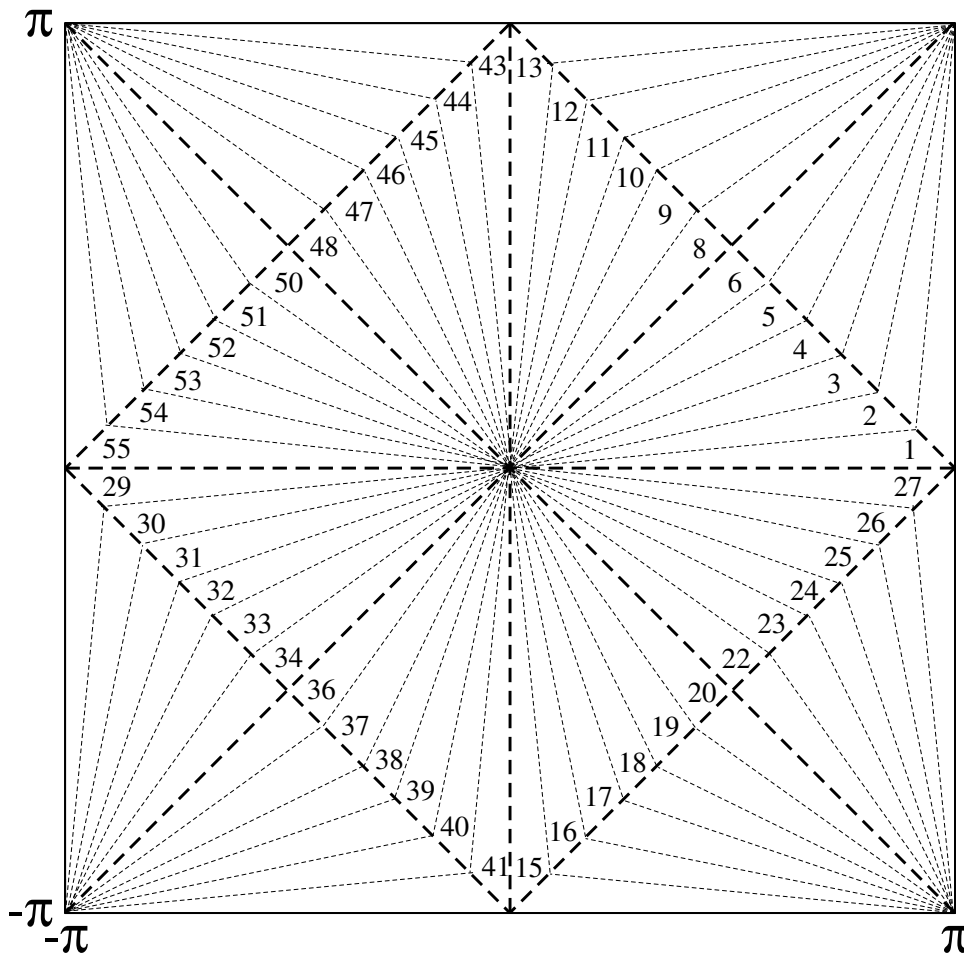


Figure 2.3: Discretisation of the Brillouin zone and the corresponding numbering scheme.

Chapter 3

Critical Scales and Dominant Correlations

In the first chapter we have mentioned that fRG methods are a powerful tool for treating correlated Fermi systems. We will now turn to concrete calculations which will show the type of results that can be obtained within fRG schemes at the current level of approximation, and in how far we can expect these results to be reliable. We extend the work presented in references [1] and [2] by conducting calculations for the Wick-ordered as well as the 1-PI scheme, for identical parameters. Comparison between the two sets of results yields valuable information with respect to quantitative as well as qualitative aspects. In this chapter we focus on correlations and restrict ourselves to the flow equation for the four-point function V .

Within the approximations we have discussed in the first and second chapter, the flow of the four-point function diverges at a finite value $\Lambda_c(T)$ for $T < T_c$, where the value of T_c depends on the bare interaction, the chemical potential and the hopping amplitudes. This feature is generic for both, the Wick-ordered as well as the 1-PI scheme, and signals the onset of strong correlations, which can lead to binding phenomena and eventually to symmetry breaking if a small coupling, for example hopping, in the third dimension is added. It can be viewed as a generalisation of the Thouless criterion, which relates the divergence in the Cooper channel appearing in the particle-particle ladder to the onset of symmetry breaking [49]. We note that the temperature T_c is of mean-field type, which is an artefact of the approximation, which does not adequately describe order-parameter fluctuations. For a continuous symmetry, these fluctuations rule out the breaking of a continuous symmetry in a two-dimensional system at finite temperature, as known from the Mermin-Wagner theorem [26]. Also, Kosterlitz-Thouless physics, as relevant to a two-component superconducting order parameter in a two-dimensional system, is not captured. However, here we are not looking at the symmetry-broken state, but are trying to extract normal-state properties near an instability. Then, strong correlations do appear, and even if they cannot lead to true long-range order

they contain information about the tendencies of the system and their mutual interplay.¹

When comparing the results from the two different schemes, we will first look at the critical scales, i.e. $\Lambda_c(T)$ and T_c , and their dependence on the chemical potential. We then turn to important qualitative information about the interplay between leading correlations, as contained in the functional behaviour of the four-point function when these critical scales are approached. The chapter is organised as follows: First we choose the parameter range of interest. This mainly concerns the chemical potential which is adjusted to look at the potential relevance of so-called hot spots. Secondly, we outline the differences between the RGE for the four-point function in the Wick-ordered and the 1-PI scheme. We then present results for the critical scales and the leading correlations, and finally conclude with a detailed discussion, mainly concerning the interpretation of the data.

3.1 Parameters

The physics of largest interest in the 2D-HM at weak coupling is found in the region between van Hove filling, when $\mu = \epsilon_{vH}$, and half filling. In the case of vanishing next-nearest neighbour hopping t' these two cases coincide for $\mu = 0$, leading to a perfectly nested Fermi surface, i.e. the nesting condition $\epsilon_{\mathbf{k}} = \epsilon_{\mathbf{k}+\mathbf{Q}}$ with $\mathbf{Q} = (\pi, \pi)$ is fulfilled for all points on the Fermi surface. In this case antiferromagnetic tendencies are known to be dominating, and no competition between different types of instabilities occurs. We avoid this situation by introducing a finite next-nearest neighbour hopping t' , which separates van Hove filling and half filling, and destroys the possibility of perfect nesting [2]. To stay away from ferromagnetic tendencies which can appear at van Hove filling, $|t'|$ must not be too large [6]. We choose $t' = -0.1$ to achieve this. Besides, if one is tempted to make contact with certain cuprates such as La_2CuO_4 -based compounds, this is not an unreasonable value. The bare coupling is always fixed at $U = 2$.

We put special focus on the importance of so-called hot spots, defined as the points where the Fermi surface intersects the Umklapp surface. The special property of these hot spots is the fact that they can be connected by $\mathbf{Q} = (\pi, \pi)$ momentum transfers, which are the driving correlations for alternating order, such as antiferromagnetism. We thus focus on values of the chemical potential for which one of the patch points on the Fermi surface is a hot spot, and

¹ In fact, a finite superconducting density *can* exist *without* true long-range order in the Kosterlitz-Thouless phase [50].

restrict ourselves to the three points on the Fermi surface which are closest to the Brillouin zone boundary. We additionally present data for van Hove filling. The corresponding Fermi surfaces illustrating the choice of parameters are shown in figure 3.1.

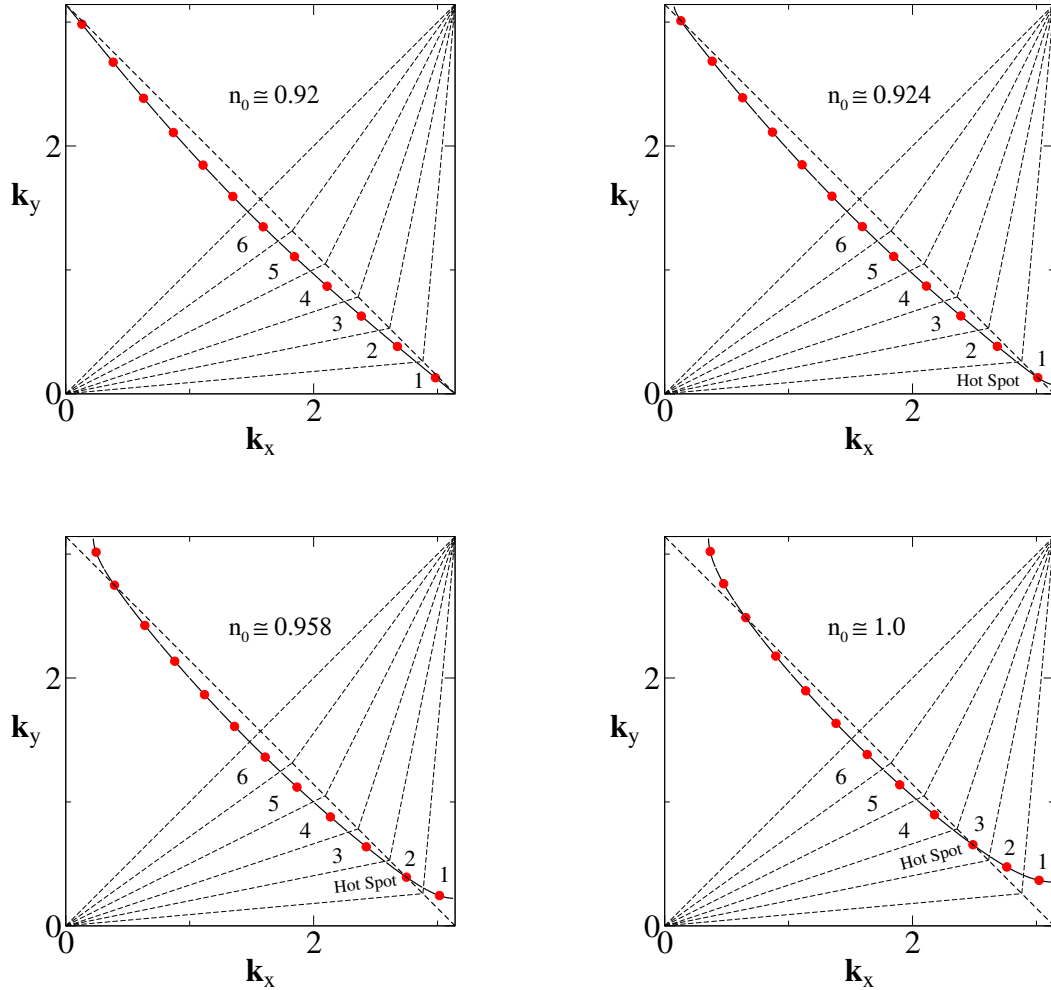


Figure 3.1: The four cases for which calculations are done. The first case is van Hove filling, the other three are defined by the condition that one of the three points near the zone boundary is located on the Umklapp surface.

3.2 Wick-ordered vs 1-PI Scheme

We have discussed the flow equations in the Wick-ordered scheme in chapters 1 and 2. At one-loop level and without self-energy feedback, the flow equation for the four-point func-

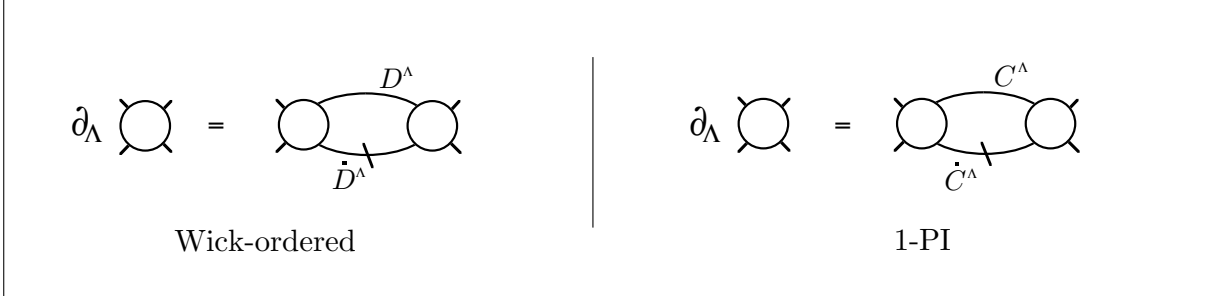


Figure 3.2: One-loop RGEs for the four-point function without self energy feedback in the Wick-ordered and the 1-PI scheme. While the diagrams are topologically identical, the crucial difference is the region of support of internal propagators.

tion in the 1-PI scheme is quite similar. In fact, the corresponding diagrams are topologically identical, as shown in figure 3.2, where both RGEs are depicted. However, while the internal lines in the Wick-ordered scheme are “D”-propagators, the ones in the 1-PI scheme are “C”-propagators. Both are free propagators living on certain subsets in \mathbf{k} -space, with a crucial difference: D_Λ is restricted to the region $|\xi_{\mathbf{k}}^0| < \Lambda$, meaning its support *shrinks* during the flow, until it vanishes completely in the limit $\Lambda \rightarrow 0$. In contrast, C_Λ is restricted to the region $|\xi_{\mathbf{k}}^0| > \Lambda$, meaning its support initially vanishes and becomes *larger* during the flow, until it covers the whole BZ in the limit $\Lambda \rightarrow 0$. The sharp border at scale Λ between support and complementary part of the BZ is identical in both schemes. In certain limiting cases and approximations only this border is relevant. In these situations both schemes yield identical results [51], which is not so in general as we will see below.

3.3 Critical Scales

In chapter 2 we have introduced the quantity Λ_{100} , which denotes the cutoff scale at which the magnitude of the largest flowing coupling V_{max} exceeds the value of 100. This scale is temperature-dependent, and we shall thus refer to it as $\Lambda_{100}(T)$. Accordingly, since there exists a critical temperature T_c above which the flow remains bounded in the limit $\Lambda \rightarrow 0$, we can also define a quantity T_{100} denoting the temperature below which the magnitude of the largest flowing coupling exceeds the value of 100 in the limit $\Lambda \rightarrow 0$.

The introduction of these quantities is necessary for two reasons:

- (1) It is rather inconvenient to look for the “real” critical values T_c and $\Lambda_c(T)$ at which the largest coupling tends to infinity, since we have to determine everything numerically, and infinity is a number which is not accessible to computer simulations.
- (2) More importantly, we use an approximation which is not valid if the couplings become too large. Clearly, there is no obvious criterion saying that a value of 100 in magnitude is large or small, but we have to make a choice. The important thing here is that we make the same choice for both schemes, of course. This should always be kept in mind when results from different sources are compared.

Results

In figure 3.3 we present the scales T_{100} and $\Lambda_{100}(T = 0)$ as a function of δ_{vH} for the two different schemes. For technical reasons we choose $T = 0.001$ to represent the zero-temperature limit, and stop the flow at $\Lambda = 0.0001$ to obtain the T_{100} results.

There are several important aspects to the results shown in figure 3.3:

- In the 1-PI scheme, the values of T_{100} and Λ_{100} differ on average by a factor of approximately 3.5. In the Wick-ordered scheme they are much closer to each other.
- The 1-PI scheme predicts the largest value of T_{100} to be at $\delta_{vH} = 0.0586$ and the largest value of Λ_{100} to be at $\delta_{vH} = 0.0068$. The Wick-ordered scheme yields exactly the opposite situation.
- In the Wick-ordered scheme, the difference between T_{100} and Λ_{100} is largest in the vicinity of van Hove filling.
- In all cases the largest scale is *not* at van Hove filling.

From these observations we find that the quantitative as well as the qualitative information about the dependence of critical energy scales on the chemical potential is somewhat inconclusive. Qualitative agreement is found in the last point, i.e. the fact that the largest scale is *not* at van Hove filling. This is different from the results reported in [18], the reasons being

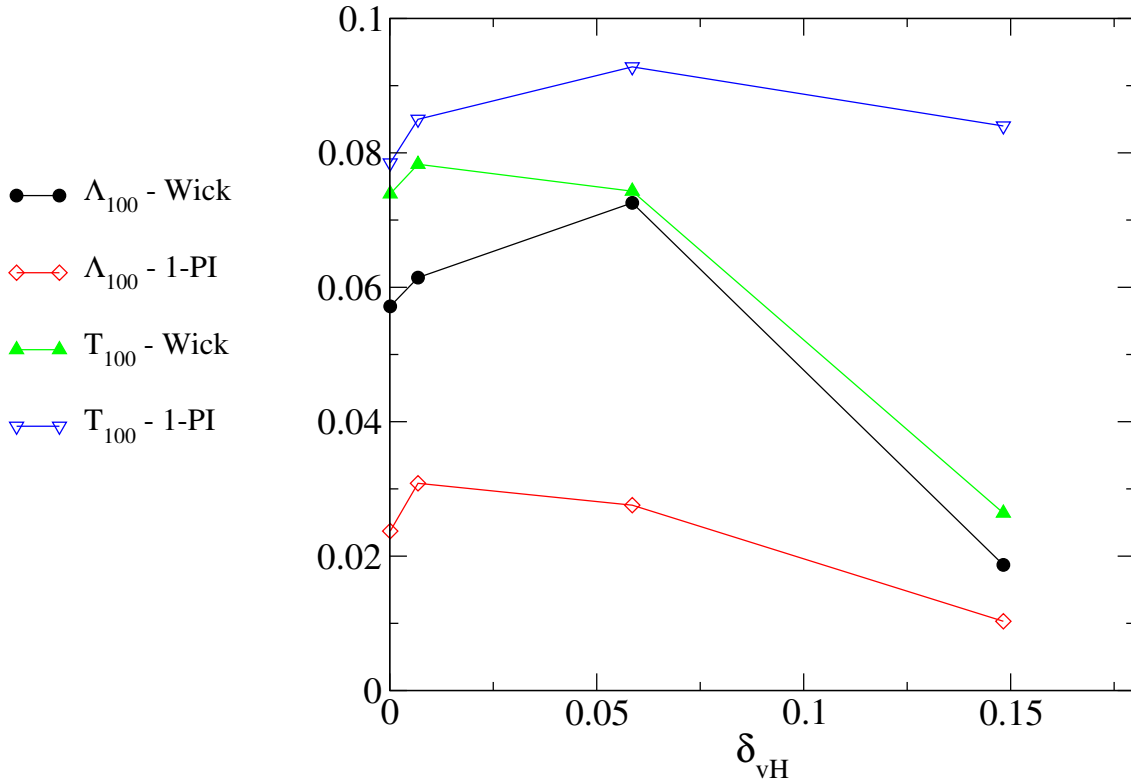


Figure 3.3: T_{100} and Λ_{100} for the Wick-ordered as well as the 1-PI scheme as a function of δ_{vH} .

most likely that in [18] a patching scheme of the “on-axis” type with a comparatively small number of patches is used, the effect of which was discussed in chapter 2.

However, we should not be too surprised about the deviations. The critical scales are non-universal, unlike critical exponents. They are more difficult to calculate and are very sensitive to differences in the approximation. This can be understood already on the level of the simple BCS case, where roughly speaking the critical temperature depends exponentially on the inverse of the effective coupling, and thus small differences in the flow can lead to large differences in the critical scales. The message here is that we must not take the values for T_{100} and Λ_{100} literally, but we should not worry too much about it, either.

We shall instead turn to a more important question about another qualitative aspect, namely the behaviour of correlations when a critical scale is approached. This is at the heart of the FRG, since we are only able to extract such information by renormalising a *function* instead of a few coupling *constants*.

It is instructive to look at the actual flow of some of the largest couplings to see how the critical scales are actually approached. In figure 3.4 we show the flow of the combined Cooper/Q-

transfer component $V^s(1, 29, 13)$ for the case $\delta_{vH} = 0.0068$ at $T = 0.001$. In addition to the two flows obtained from the Wick-ordered and the 1-PI scheme, we show the flows in either scheme when the four-point function on the RHS of the RGE is replaced by the bare coupling. In the limit $\Lambda \rightarrow 0$ this reproduces the results in second-order perturbation theory (SOPT). We see that for $\Lambda > 1$ not much happens and the feedback of the four-point function on the RHS of the RGE is not of crucial importance. For $\Lambda < 1$ this feedback starts to play a more and more important role, and the fact that the value of $V^s(1, 29, 13)$ is slightly higher in the Wick-ordered scheme at $\Lambda = 1$ leads to a substantially quicker increase in the low-energy region. We also note that the *results* in SOPT agree in both schemes in the limit $\Lambda \rightarrow 0$, while the *paths* taken by the four-point functions are slightly different.

In figure 3.5 we plot the flow of the combined Cooper/**Q**-transfer component $V^s(1, 29, 13)$ as well as the Umklapp component $V^s(1, 1, 41)$ from both schemes at T_{100} (c.f. figure 2.3). Note that in the 1-PI scheme $V^s(1, 1, 41)$ is always larger than $V^s(1, 29, 13)$. In the Wick-ordered scheme the flow of $V^s(1, 1, 41)$ is cut off for small Λ due to the shrinking phase space, and consequently $V^s(1, 29, 13)$ is the largest coupling in the limit $\Lambda \rightarrow 0$. Figure 3.5 also illustrates the relevance of our choice to stop the flow at $V_{max} = 100$. Had we chosen $V_{max} = 10$ the qualitative picture would be the same as in the 1-PI scheme, with $V^s(1, 29, 13)$ smaller than $V^s(1, 1, 41)$. However, the numerical values in the different schemes still differ by a factor of about two.

3.4 Dominant Correlations

We now analyse the dominant correlations for the three cases when the patch points near the zone boundary are hot spots. We omit the case of van Hove filling since it does not differ significantly from the case $\delta_{vH} = 0.0068$, i.e. the case when the first patch point is a hot spot.

Results

In tables 3.1 to 3.3 the six strongest coupling components are listed, for T_{100} and Λ_{100} in either scheme. The parametrisation of the vertex function is to be inter-linked with figure 2.3 for identification.

An inherent feature of all results is the competition between Cooper couplings and **Q**-transfer couplings, which is consistent with previous calculations [1, 2, 41]. The term ‘competition’

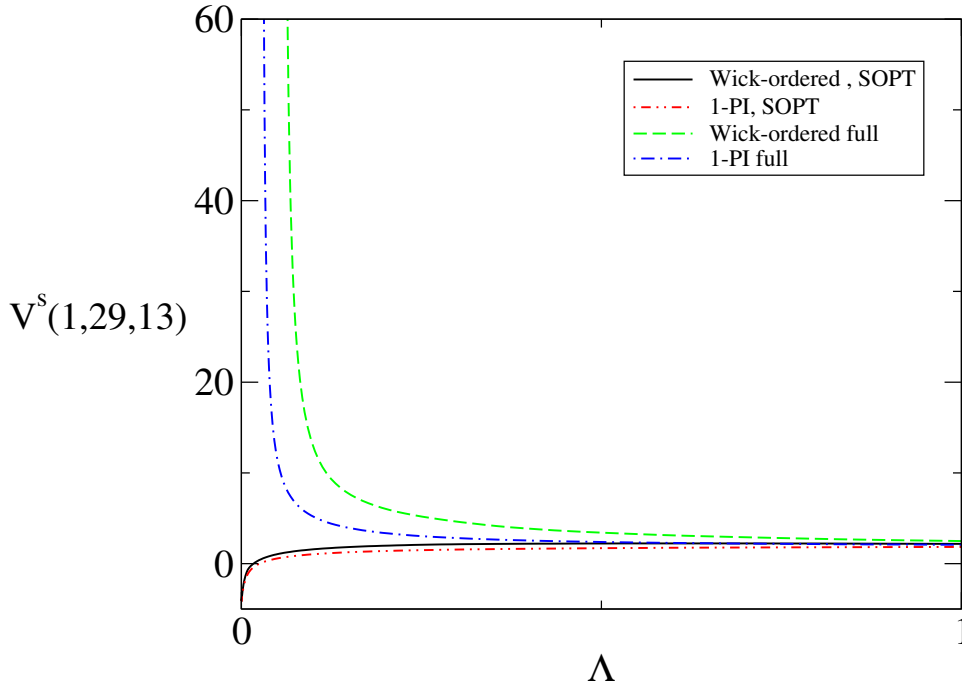


Figure 3.4: Flow of the combined Cooper/ \mathbf{Q} -transfer component $V_{\Lambda}^s(1, 29, 13)$ for the case $\delta_{vH} = 0.0068$ at $T = 0.001$.

should be used with caution, though. Strong correlations in the Cooper channel at small energy scales, which signal the onset of strong superconducting fluctuations, cannot appear without the influence of particle-hole contributions at high and intermediate energy scales during the flow. The \mathbf{Q} -transferring couplings are among the strongest of these contributions, meaning that at higher energy scales we do not find competition, but rather favourable influence of the particle-hole channel on the particle-particle channel, in which the Cooper divergence eventually appears. On the other hand, once substantial correlations are generated in the particle-particle channel, they feed back onto the particle-hole channel. At sufficiently small but still finite energy scales and $T = 0$ a divergence will always show up in the Cooper channel, provided that no other divergence sets in before. This is a general feature in interacting Fermi systems, known as the Kohn-Luttinger effect [52]. However, if another divergence does appear *before* the Cooper divergence sets in, we end up with a different situation. In the cases we are looking at this other divergence appears in the \mathbf{Q} -transferring ‘subspace’ of the particle-hole channel and reflects antiferromagnetic tendencies in the system.²

²We note that it is also possible to find the leading correlations in a non-commensurate channel [53], but that is not observed here.

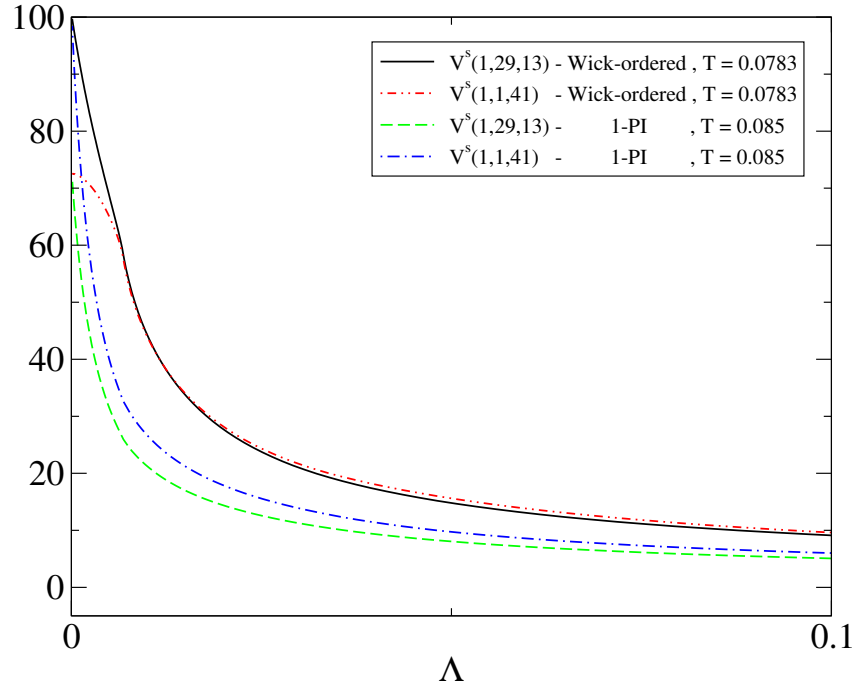


Figure 3.5: Flow of the combined Cooper/ \mathbf{Q} -transfer component $V_{\Lambda}^s(1, 29, 13)$ and the Umklapp coupling $V_{\Lambda}^s(1, 1, 41)$ for the case $\delta_{vH} = 0.0068$ and $V_{max} = 100$.

A closer look at the data in tables 3.1 to 3.3 shows that the two schemes agree in certain cases, while in others they do not. Also, the same scheme can yield a slightly different picture at T_{100} in comparison to the zero-temperature results for $\Lambda \rightarrow \Lambda_{100}$.

For $\delta_{vH} = 0.0068$ both schemes show excellent agreement in the results for $\Lambda \rightarrow \Lambda_{100}$. In both cases the \mathbf{Q} -transferring Umklapp coupling $V^S(1, 1, 41)$ with both incoming momenta at the first patch point is the leading coupling, followed by the \mathbf{Q} -transferring Cooper coupling $V^S(1, 29, 13)$ with one incoming momentum at the first patch point. In the 1-PI scheme the sub-leading correlations are predominantly of \mathbf{Q} -transferring type, while in the Wick-ordered scheme also the Cooper coupling $V^S(1, 29, 15)$ is rather large. This tendency carries over to the results at T_{100} where it is more evident: Compared to the zero-temperature results $V^S(1, 29, 13)$ is enhanced and $V^S(1, 1, 41)$ suppressed in the Wick-ordered scheme, while in the 1-PI scheme the Cooper couplings are suppressed and the Umklapp coupling remains strongest, closely followed by other \mathbf{Q} -transferring couplings.

For $\delta_{vH} = 0.0586$ the second patch point is a hot spot, and in both schemes the results for

$\Lambda \rightarrow \Lambda_{100}$ agree reasonably well. The **Q**-transferring Umklapp coupling $V^S(2, 2, 40)$ with both incoming momenta on the second patch point is dominating, and we have a first indication towards the relevance of hot spots. We note that the 1-PI scheme shows slightly stronger correlations in the Cooper channel than the Wick-ordered scheme, but they agree in showing that it now is the **Q**-transferring Cooper coupling $V^S(2, 30, 12)$ with one incoming momentum at the second patch which is largest within the Cooper subset – a further hint towards the importance of the hot spots.

The results at T_{100} behave similarly as for $\delta_{vH} = 0.0068$. In the Wick-ordered scheme the results shift towards stronger Cooper correlations, while in the 1-PI scheme **Q**-transferring couplings take over. Furthermore, in the Wick-ordered scheme the strongest Cooper coupling is not $V^S(2, 30, 12)$, but $V^S(1, 29, 13)$. We assign this to the higher density of states in the first patch near van Hove filling. This effect is absent in the zero-temperature results since the cutoff does not cross the van-Hove scale. At T_{100} the cutoff does cross this scale and the effect of the high density of states at the van-Hove scale shows up.

For $\delta_{vH} = 0.1482$ already the results for $\Lambda \rightarrow \Lambda_{100}$ differ in the sense that the Wick-ordered scheme favours Cooper correlations *not* located on the hot spot, while in the 1-PI scheme the **Q**-transferring Umklapp coupling $V^S(3, 3, 39)$ with both incoming momenta on the third patch point is strongest. In the results at T_{100} we observe that in the Wick-ordered scheme $V^S(2, 2, 40)$ becomes larger, and the strongest coupling changes to be the **Q**-transferring Cooper coupling $V^S(3, 31, 11)$ with one incoming momentum at the third patch. In the 1-PI scheme $V^S(3, 3, 39)$ remains strongest, and Cooper correlations are again suppressed with respect to the results for $\Lambda \rightarrow \Lambda_{100}$. We note that $\delta_{vH} = 0.1482$ corresponds to half filling, which is however not a special situation here since we are in the weak-coupling region and away from particle-hole symmetry due to a finite $t' = -0.1$.

Wick $\Lambda_{100} = 0.0614$			1-PI $\Lambda_{100} = 0.0308$		
Coupling	Value	Type	Coupling	Value	Type
$V^s(1, 1, 41)$	100.6	Q-transfer	$V^s(1, 1, 41)$	101.5	Q-transfer
$V^s(1, 29, 13)$	88.5	Cooper , Q-transfer	$V^s(1, 29, 13)$	69.1	Cooper , Q-transfer
$V^s(1, 55, 15)$	84.4	Q-transfer	$V^s(1, 55, 15)$	62.1	Q-transfer
$V^s(1, 27, 41)$	80.5	Q-transfer	$V^s(1, 27, 41)$	62.0	Q-transfer
$V^s(1, 29, 15)$	76.5	Cooper	$V^s(1, 13, 29)$	47.2	Q-transfer
$V^s(1, 1, 15)$	50.5		$V^s(1, 15, 55)$	45.0	Q-transfer

Wick $T_{100} = 0.0783$			1-PI $T_{100} = 0.085$		
Coupling	Value	Type	Coupling	Value	Type
$V^s(1, 29, 13)$	99.7	Cooper , Q-transfer	$V^s(1, 1, 41)$	98.4	Q-transfer
$V^s(1, 29, 15)$	87.4	Cooper	$V^s(1, 27, 41)$	95.9	Q-transfer
$V^s(1, 1, 41)$	72.5	Q-transfer	$V^s(1, 55, 15)$	95.8	Q-transfer
$V^s(1, 29, 27)$	-69.9	Cooper	$V^s(1, 1, 15)$	88.2	
$V^s(1, 29, 1)$	-68.3	Cooper , Forward	$V^s(1, 1, 43)$	87.1	
$V^s(1, 55, 15)$	55.1	Q-transfer	$V^s(1, 29, 15)$	81.4	Cooper

Table 3.1: Strongest couplings, hot spot in first patch ($\delta_{vH} = 0.0068$)

Wick			$\Lambda_{100} = 0.0726$		
Coupling	Value	Type			
$V^s(2, 2, 40)$	100.2	Q-transfer			
$V^s(1, 2, 40)$	61.4	Q-transfer			
$V^s(1, 54, 16)$	56.8	Q-transfer			
$V^s(1, 30, 12)$	56.6	Q-transfer			
$V^s(2, 30, 12)$	55.8	Cooper , Q-transfer			
$V^s(1, 26, 44)$	55.6	Q-transfer			

1-PI			$\Lambda_{100} = 0.0276$		
Coupling	Value	Type			
$V^s(2, 2, 40)$	102.0	Q-transfer			
$V^s(2, 30, 12)$	72.4	Cooper , Q-transfer			
$V^s(1, 2, 40)$	64.7	Q-transfer			
$V^s(1, 29, 13)$	59.0	Cooper			
$V^s(1, 54, 16)$	57.6	Q-transfer			
$V^s(1, 30, 12)$	56.5	Q-transfer			

Wick			$T_{100} = 0.0743$		
Coupling	Value	Type			
$V^s(1, 29, 13)$	99.3	Cooper			
$V^s(2, 2, 40)$	89.8	Q-transfer			
$V^s(1, 29, 15)$	82.4	Cooper			
$V^s(2, 30, 12)$	81.1	Cooper Q-transfer			
$V^s(1, 29, 1)$	-73.7	Cooper , Forward			
$V^s(1, 29, 27)$	-71.9	Cooper			

1-PI			$T_{100} = 0.0928$		
Coupling	Value	Type			
$V^s(2, 2, 40)$	98.5	Q-transfer			
$V^s(1, 2, 40)$	73.3	Q-transfer			
$V^s(1, 1, 41)$	72.3				
$V^s(3, 3, 39)$	64.0	Q-transfer			
$V^s(1, 54, 16)$	62.0	Q-transfer			
$V^s(1, 26, 44)$	58.8	Q-transfer			

Table 3.2: Strongest couplings, hot spot in second patch ($\delta_{vH} = 0.0586$)

Wick $\Lambda_{100} = 0.0187$			1-PI $\Lambda_{100} = 0.0103$		
Coupling	Value	Type	Coupling	Value	Type
$V^s(2, 30, 12)$	106.8	Cooper	$V^s(3, 3, 39)$	100.7	Q-transfer
$V^s(3, 31, 11)$	93.5	Cooper , Q-transfer	$V^s(3, 31, 11)$	72.4	Cooper , Q-transfer
$V^s(1, 29, 12)$	90.0	Cooper	$V^s(4, 4, 38)$	65.1	
$V^s(1, 29, 13)$	89.8	Cooper	$V^s(2, 2, 40)$	61.4	
$V^s(2, 30, 2)$	-89.4	Cooper , Forward	$V^s(2, 3, 39)$	58.9	Q-transfer
$V^s(2, 30, 16)$	88.2	Cooper	$V^s(2, 30, 12)$	56.8	Cooper

Wick $T_{100} = 0.0264$			1-PI $T_{100} = 0.084$		
Coupling	Value	Type	Coupling	Value	Type
$V^s(3, 31, 11)$	99.2	Cooper , Q-transfer	$V^s(3, 3, 39)$	98.0	Q-transfer
$V^s(3, 3, 39)$	92.2	Q-transfer	$V^s(4, 4, 38)$	69.4	
$V^s(2, 30, 12)$	84.0	Cooper	$V^s(2, 2, 40)$	63.7	
$V^s(3, 31, 3)$	-73.5	Cooper , Forward	$V^s(2, 3, 39)$	62.1	Q-transfer
$V^s(2, 30, 2)$	-64.3	Cooper , Forward	$V^s(3, 4, 39)$	57.0	Q-transfer
$V^s(2, 30, 11)$	62.6	Cooper	$V^s(5, 5, 37)$	53.7	

Table 3.3: Strongest couplings, hot spot in third patch ($\delta_{vH} = 0.1482$)

3.5 Discussion

We have seen that the Wick-ordered and the 1-PI fRG schemes agree with respect to certain aspects and disagree with respect to others. The two main reasons which have to be considered to explain the discrepancies are the following:

- (1) As mentioned before, the two flow equations for the four-point function are quite different from a technical point of view. The flow of the 1-PI scheme starts much slower due to the restricted phase space at the beginning of the flow, while in the Wick-ordered scheme the contributing phase space shrinks towards the end of the flow. Since the divergences appearing in both schemes are due to feedback effects of the flowing four-point functions during the flow, the different initial behaviour leads to sometimes considerable differences in the results. This can be seen in figures 3.4 and 3.5.
- (2) In the 1-PI scheme the projection of momenta appearing as arguments in the four-point function on internal lines onto the Fermi surface is not well-controlled in the limit $\Lambda \rightarrow 0$, since the internal momenta are not restricted to a small shell around the Fermi surface, but rather lie outside this shell. In this respect the Wick-ordered scheme can be expected to be more reliable.

The different behaviour of results in the two schemes is also present and in fact even more obvious when response functions are calculated. For example, in the Wick-ordered scheme the flow of certain susceptibilities in the particle-hole channel, such as e.g. those relevant for antiferromagnetic tendencies, is cut off due to the shrinking phase space for small values of Λ [1, 18], while this is not the case in the 1-PI scheme [2, 32].

Despite the disagreement which undoubtedly exists for certain cases, we note the common success shared by fRG methods in general, and the Wick-ordered and 1-PI scheme in particular. We recall that the driving force behind most of the recent work on the 2D-HM is the issue of the mechanisms leading to superconductivity in High- T_c cuprates. In this respect both schemes, and we can say all fRG schemes, offer the same natural mechanism for the appearance of superconducting correlations in the weak-coupling limit, in particular explaining the d -wave symmetry of the order parameter. This mechanism is understood on the basis of perturbation theory as a consequence of the interplay between particle-hole and particle-particle contributions. Certain infinite summations in perturbation theory, such as ladder

approximations or FLEX, demonstrate similar effects, but they cannot treat the mutual interplay *on equal footing*. Moreover, the fRG results obtained so far are only the first step of successive improvements of approximations on the basis of a rigorous and exact starting point. With respect to real materials it is necessary to carry the calculations over to higher values of the bare interaction. Also, new materials which can be mapped to the Hubbard model and in which the repulsion is weak would be helpful since they could be directly compared to weak-coupling calculations.

We have stated at the beginning of chapter 2 that the static approximation for the four-point function may become unreliable when the couplings become large. However, looking at particular restrictions of the RGE we see that this is not necessarily the case. For instance, if we reduce the RHS of the RGE for the four-point function to the particle-particle channel, we recover the effective interaction as known from the non-selfconsistent T-matrix approximation. This includes the frequency dependence, albeit a very simple one since in this case the effective interaction depends only on total incoming momentum and frequency. Thus, we can evaluate the one-loop diagram on the RHS, since the total incoming frequency can be taken out of the sum over the internal frequency and momentum variable. Similarly, restricting ourselves to the direct particle-hole channel we recover the familiar non-selfconsistent RPA. In both approximations the effective interaction diverges first at zero total frequency, and zero frequency transfer respectively. Thus, since the frequency channels are decoupled we can in these cases restrict the flow to the zero-frequency component to determine critical scales without including the frequency dependence of the four-point function on the RHS. The hope is that this carries over in some approximate way to the case when the coupling between all three channels is included. However, this leads to a more complex frequency dependence, with the four-point function truly depending on three momenta and frequencies, also on the internal frequency over which is summed. Then, when the couplings become large we do not know in how far the replacement of the four-point function by its static components is reasonable, and the approximation may break down.

Chapter 4

Self Energy and Spectral Function

In the previous chapter we have seen that the fRG yields valuable information on strong correlations which appear in the vicinity of critical scales in the 2D-HM. In this chapter we turn to the question in how far these strong correlations affect single-particle properties. We employ the Wick-ordered fRG scheme to calculate the one-particle irreducible self energy, again focusing on the relevance of hot spots.

Single-particle properties of a many-body system are encoded in the retarded Green function $G(\omega + i0^+, \mathbf{k})$, which is related to the one-particle self energy via the Dyson equation

$$G^{-1}(\omega + i0^+, \mathbf{k}) = \omega - (\epsilon_{\mathbf{k}}^0 - \mu) - \Re\Sigma(\omega + i0^+, \mathbf{k}) - i\Im\Sigma(\omega + i0^+, \mathbf{k}). \quad (4.1)$$

To compute the self energy, we calculate the imaginary part $\Im\Sigma(\omega + i0^+, \mathbf{k})$ for momenta on the (non-interacting) Fermi surface from the flow of the two-point function as given in equation 1.24, and from this determine the real part $\Re\Sigma(\omega + i0^+, \mathbf{k})$ via a Kramers-Kronig relation. Since we work directly on the real axis, the determination of the single-particle spectral function $A(\omega, \mathbf{k})$ is straightforward. In equation 1.24 we can only identify the two-point function Σ_{Λ} with the “true” self energy Σ in the limit $\Lambda \rightarrow 0$, which means we have to integrate the flow down to zero. We shall mostly be interested in temperatures slightly above T_c , where the renormalised couplings are strongest, and are thus expected to be most relevant. In physical terms this means we probe the system in the non-symmetry-broken phase close to a temperature at which binding phenomena begin to have noticeable effects on one-particle properties.

4.1 Spectral Function and Quasi-Particle Peak

The way in which the Green function contains information on single-particle properties is readily seen by looking at the spectral function $A(\omega, \mathbf{k})$. The spectral function is given, follow-

ing the convention used by Mahan [54], as

$$\begin{aligned} A(\omega, \mathbf{k}) &= -2 \Im G(\omega + i0^+, \mathbf{k}) \\ &= \frac{-2 \Im \Sigma(\omega + i0^+, \mathbf{k})}{[\omega - (\epsilon_{\mathbf{k}}^0 - \mu) - \Re \Sigma(\omega + i0^+, \mathbf{k})]^2 + [\Im \Sigma(\omega + i0^+, \mathbf{k})]^2} \end{aligned} \quad (4.2)$$

The term quasi particle is introduced after realising that under certain conditions the spectral function possesses a single, well-defined peak located at a certain energy $\epsilon_{\mathbf{k}}$. The spectral function then has a functional form closely related to a Lorentzian, and the so-called renormalised dispersion $\epsilon_{\mathbf{k}}$ is generally given by the condition

$$\epsilon_{\mathbf{k}} - (\epsilon_{\mathbf{k}}^0 - \mu) - \Re \Sigma(\epsilon_{\mathbf{k}}, \mathbf{k}) = 0, \quad (4.3)$$

provided the solution of this equation is unique. The relation of the spectral function to a Lorentzian becomes obvious when the self energy is expanded in a Taylor series around $\epsilon_{\mathbf{k}}$:

$$\Re \Sigma(\omega, \mathbf{k}) \approx \Re \Sigma(\epsilon_{\mathbf{k}}, \mathbf{k}) + (\omega - \epsilon_{\mathbf{k}}) \left. \frac{\partial \Re \Sigma(\omega', \mathbf{k})}{\partial \omega'} \right|_{\omega'=\epsilon_{\mathbf{k}}} + \frac{1}{2} (\omega - \epsilon_{\mathbf{k}})^2 \left. \frac{\partial^2 \Re \Sigma(\omega', \mathbf{k})}{\partial \omega'^2} \right|_{\omega'=\epsilon_{\mathbf{k}}} \quad (4.4)$$

$$\Im \Sigma(\omega, \mathbf{k}) \approx \Im \Sigma(\epsilon_{\mathbf{k}}, \mathbf{k}) + (\omega - \epsilon_{\mathbf{k}}) \left. \frac{\partial \Im \Sigma(\omega', \mathbf{k})}{\partial \omega'} \right|_{\omega'=\epsilon_{\mathbf{k}}} + \frac{1}{2} (\omega - \epsilon_{\mathbf{k}})^2 \left. \frac{\partial^2 \Im \Sigma(\omega', \mathbf{k})}{\partial \omega'^2} \right|_{\omega'=\epsilon_{\mathbf{k}}} \quad (4.5)$$

If the corrections are small enough to justify these approximations, one typically uses $\Re \Sigma$ in first order and $\Im \Sigma$ in zeroth order in $(\omega - \epsilon_{\mathbf{k}})$ to obtain

$$G^{-1}(\omega + i0^+, \mathbf{k}) \approx (\omega - \epsilon_{\mathbf{k}}) \left(1 - \left. \frac{\partial \Re \Sigma(\omega', \mathbf{k})}{\partial \omega'} \right|_{\omega'=\epsilon_{\mathbf{k}}} \right) - i \Im \Sigma(\epsilon_{\mathbf{k}}, \mathbf{k}) \quad (4.6)$$

and

$$A(\omega, \mathbf{k}) \approx A^{QP}(\omega, \mathbf{k}) = Z_{\mathbf{k}} \frac{-2 Z_{\mathbf{k}} \Im \Sigma(\epsilon_{\mathbf{k}}, \mathbf{k})}{(\omega - \epsilon_{\mathbf{k}})^2 + (Z_{\mathbf{k}} \Im \Sigma(\epsilon_{\mathbf{k}}, \mathbf{k}))^2}, \quad (4.7)$$

with the field renormalisation factor

$$Z_{\mathbf{k}} := \left(1 - \left. \frac{\partial \Re \Sigma(\omega', \mathbf{k})}{\partial \omega'} \right|_{\omega'=\epsilon_{\mathbf{k}}} \right)^{-1}.$$

In this approximation the spectral function is thus approximated by a quasi-particle Lorentzian $A^{QP}(\omega, \mathbf{k})$, multiplied by a weight factor $Z_{\mathbf{k}}$. The retarded Green function has a single pole at $\omega = \epsilon_{\mathbf{k}} + iZ_{\mathbf{k}} \Im\Sigma(\epsilon_{\mathbf{k}}, \mathbf{k})$. From this a quasi-particle life time can be defined and calculated [55], and the inverse life time (scattering rate) is given as

$$\gamma_{\mathbf{k}} = \frac{1}{\tau_{\mathbf{k}}} \approx |Z_{\mathbf{k}} \Im\Sigma(\epsilon_{\mathbf{k}}, \mathbf{k})| . \quad (4.8)$$

$\epsilon_{\mathbf{k}} < 0$ corresponds to a mainly hole-like excitation, $\epsilon_{\mathbf{k}} > 0$ a mainly particle-like one. The quasi-particle dispersion can be used to define a Fermi surface for an interacting system at finite temperature via the condition $\epsilon_{\mathbf{k}_F} = 0$, i.e.

$$(\epsilon_{\mathbf{k}}^0 - \mu) + \Re\Sigma(0, \mathbf{k}) = 0 \quad \text{for } \mathbf{k} \in \{\mathbf{k}_F\} \quad (4.9)$$

We will see that in certain cases $\Im\Sigma$ shows a dip at $\omega = 0$ for momenta on the Fermi surface. This dip becomes more pronounced when the critical temperature is approached from above. The approximation in 4.4 and 4.5 is then no longer justified, and the quasi-particle picture becomes inappropriate.

We note that equation 4.6 connects the microscopic description of single-particle properties in a many-fermion system with the elementary excitations upon which the phenomenological Landau-Fermi-liquid theory [55] is based. In the following, if 4.6 is no longer valid we shall speak of “non-Fermi-liquid behaviour”, or equivalently of a breakdown of the Landau-Fermi-liquid picture.

4.2 Adjustment of the Fermi Surface

In standard perturbation theory the self energy is calculated first, and then the density is determined from the resulting interacting Green function. Alternatively, the chemical potential can be readjusted to keep the density fixed. In self-consistent treatments this happens intrinsically, while in non-self-consistent calculations there remains the problem of Fermi-surface shifts mentioned in the first chapter. We avoid this problem by forcing the Fermi surface to remain at its non-interacting location by making the shift

$$\Sigma(\omega, \mathbf{k}) \mapsto \Sigma(\omega, \mathbf{k}) - \Re\Sigma(0, \mathbf{k}_F(\mathbf{k})) \quad (4.10)$$

before inserting it into equation 4.2. $\mathbf{k}_F(\mathbf{k})$ is a suitable projection of \mathbf{k} onto the Fermi surface of the non-interacting system. Equation 4.10 can be viewed as a correction to the dispersion relation. This artificial constraint is only sensible as long the corrections due to $\Re\Sigma$ are sufficiently small. We checked that this is indeed the case for the calculations presented here.

4.3 Calculating the Self Energy at Real Frequencies

The steps which are required to calculate the self energy are analogous to the ones made for the flow of the four-point function in chapter 2. Since we drop the frequency dependence in the four-point function, use a momentum cutoff and neglect self energy correction on internal propagators, we can carry out internal frequency sums analytically and do a straightforward analytical continuation via $k = (i\omega_n, \mathbf{k}) \rightarrow (\omega + i0^+, \mathbf{k})$ in equation 1.24. This is outlined in more detail in appendix B. For technical reasons we split the RHS of equation 1.24 into two contributions, which we call $PP\dot{H}$ and $PH\dot{P}$, according to their topology as shown in Fig. 4.1. In diagram $PP\dot{H}$ a “hole-like” propagator is differentiated with respect to Λ , whereas in diagram $PH\dot{P}$ a “particle-like” propagator is differentiated.¹

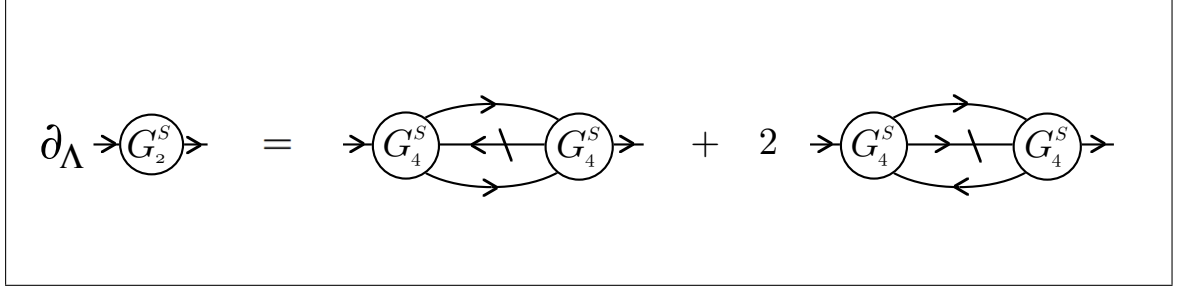
We only need to calculate the flow of the imaginary part $\Im\Sigma$, since we can obtain the real part $\Re\Sigma$ via Kramers-Kronig relations. This leads to a substantial simplification, since we can make use of the relation $\Im\frac{1}{x+i0^+} = -\pi\delta(x)$ in the integration kernel, and thus the integration over initially four variables is reduced to a two-dimensional one. We shall mention here that the numerical effort to solve the final flow equation is still very high, and one run takes about a week, using a parallel algorithm on a 20-cpu Linux cluster running on AMD Athlon 2200+ cpus. This limits the amount of data we are able to obtain within a reasonable time frame, with the required numerical accuracy.

The two diagrams lead to a RHS of the flow equation for Σ_Λ given by

$$\partial_\Lambda \Sigma_\Lambda = PP\dot{H} + 2PH\dot{P} \quad (4.11)$$

where

¹The terms “hole-like” and “particle-like” are used to account for the “directional character” of the internal lines and are not to be taken literally. In fact, each internal line includes the description of both, the propagation of a hole as well as that of a particle.

Figure 4.1: The two contributions $PP\dot{H}$ and $PH\dot{P}$ to the flow of the two-point function.

$$\begin{aligned}
\Im(PP\dot{H}) = & \\
& \frac{\pi}{(2\pi)^4} \sum_{s=\pm 1} \int d\tilde{\lambda} J(s\Lambda, \tilde{\lambda}) \\
& \int d^2\mathbf{q} F(\mathbf{k}, \mathbf{q}, \mathbf{p}) \left[\Gamma_\Lambda^s(\mathbf{k}, \mathbf{p}; \mathbf{q}, \mathbf{k} + \mathbf{p} - \mathbf{q})^2 + 3 \Gamma_\Lambda^t(\mathbf{k}, \mathbf{p}; \mathbf{q}, \mathbf{k} + \mathbf{p} - \mathbf{q})^2 \right] \\
& \Theta(\Lambda - |\xi_{\mathbf{k}+\mathbf{p}-\mathbf{q}}^0|) \Theta(\Lambda - |\xi_{\mathbf{q}}^0|) \delta(\omega - \xi_{\mathbf{p}}^0 + \xi_{\mathbf{q}}^0 - \xi_{\mathbf{k}+\mathbf{p}-\mathbf{q}}^0) \Big|_{\mathbf{p}=\mathbf{p}(s\Lambda, \tilde{\lambda})}
\end{aligned} \tag{4.12}$$

$$\begin{aligned}
\Im(PH\dot{P}) = & \\
& \frac{\pi}{(2\pi)^4} \sum_{s=\pm 1} \int d\tilde{\lambda} J(s\Lambda, \tilde{\lambda}) \\
& \int d^2\mathbf{q} F(\mathbf{k}, \mathbf{p}, \mathbf{q}) \left[\Gamma_\Lambda^s(\mathbf{k}, \mathbf{q}; \mathbf{p}, \mathbf{k} + \mathbf{q} - \mathbf{p})^2 + 3 \Gamma_\Lambda^t(\mathbf{k}, \mathbf{q}; \mathbf{p}, \mathbf{k} + \mathbf{q} - \mathbf{p})^2 \right] \\
& \Theta(\Lambda - |\xi_{\mathbf{k}+\mathbf{q}-\mathbf{p}}^0|) \Theta(\Lambda - |\xi_{\mathbf{q}}^0|) \delta(\omega - \xi_{\mathbf{p}}^0 + \xi_{\mathbf{q}}^0 - \xi_{\mathbf{k}+\mathbf{q}-\mathbf{p}}^0) \Big|_{\mathbf{p}=\mathbf{p}(s\Lambda, \tilde{\lambda})}
\end{aligned} \tag{4.13}$$

Here, $\tilde{\lambda}$ is the angular variable over which remains to be integrated after the delta function due to $\dot{D}_\Lambda(p)$ is evaluated. $J(s\Lambda, \tilde{\lambda})$ is the Jacobian of the transformation $(p_x, p_y) \rightarrow (\tilde{\xi}, \tilde{\lambda})$, and $F(\mathbf{k}, \mathbf{p}, \mathbf{q}) = (f(\xi_{\mathbf{q}}^0) - f(\xi_{\mathbf{k}-\mathbf{p}+\mathbf{q}}^0))(f(\xi_{\mathbf{p}}^0) + b(\xi_{\mathbf{q}}^0 - \xi_{\mathbf{k}-\mathbf{p}+\mathbf{q}}^0))$, where $f(x) = (e^{\frac{x}{T}} + 1)^{-1}$ and $b = (e^{\frac{x}{T}} - 1)^{-1}$ are Fermi and Bose functions, respectively. The function $F(\mathbf{k}, \mathbf{p}, \mathbf{q})$ is symmetric in \mathbf{p} and \mathbf{q} , in contrast to its appearance. The mapping of Γ onto V is done by projecting

the external momentum \mathbf{k} and the two internal momenta \mathbf{q} and \mathbf{p} onto the Fermi surface. This procedure is again exact in the limit $\Lambda \rightarrow 0$ and for infinitely many patches, since then the internal momenta are restricted to a small stripe around the Fermi surface, and we take the external momentum to be directly on the Fermi surface.

Once we have calculated the imaginary part of the self energy on the entire real axis, we obtain the real part, up to a frequency-independent real constant $\tilde{\Sigma}(\mathbf{k})$, using a Kramers–Kronig relation [56]. We then have

$$\Re\Sigma(\omega + i0^+, \mathbf{k}) = P \int \frac{d\omega'}{\pi} \frac{\Im\Sigma(\omega' + i0^+, \mathbf{k})}{\omega' - \omega} + \tilde{\Sigma}(\mathbf{k}), \quad (4.14)$$

where P denotes the Cauchy principal value. We implicitly fix $\tilde{\Sigma}(\mathbf{k}_F)$ to keep the Fermi surface fixed, instead of determining it self-consistently. In a more sophisticated, self-consistent treatment the condition $\tilde{\Sigma}(\mathbf{k}_F) = 0$ determines the shape of the Fermi surface [25].

4.4 Parameters

We use similar parameters as in the previous chapter and again restrict ourselves to the case when one of the first three patch points near the zone boundary is a hot spot. The results for van Hove filling are essentially identical to the results for $\delta_{vH} = 0.0068$.

Here, we fix the temperature instead of the bare coupling in order to minimise and control the influence of thermal effects. We use $T = 0.05$, and for each of the three cases we do three distinct calculations:

- One without a flow in the coupling function, meaning we replace the four-point function on the RHS of equation 1.24 by U . This yields the results in second-order perturbation theory in the bare coupling.
- One in which the bare coupling is adjusted such that the magnitude of the largest coupling V_{max} in the limit $\Lambda \rightarrow 0$ is approximately 15.
- One in which the bare coupling is adjusted such that the magnitude of the largest coupling V_{max} in the limit $\Lambda \rightarrow 0$ is approximately 150.

These choices are made to determine how large the correlations have to be to have a substantial influence on one-particle properties. The values of the bare interaction are listed in table 4.1.

δ_{vH}	$U (V_{max} = 15)$	$U (V_{max} = 150)$
0.0068	1.685	1.815
0.0586	1.68	1.8625
0.1482	1.80	2.06

Table 4.1: Values of the bare interaction U

4.5 Results

We begin with results for $\delta_{vH} = 0.0068$ and $\delta_{vH} = 0.1482$. We show in figure 4.2 the full frequency dependence of the imaginary part of the self energy at the respective hot spots. We have plotted the data for $V_{max} = 150$, as well as the results in second-order perturbation theory (SOPT). We observe a narrow negative peak at zero frequency in the data for $V_{max} = 150$, while the low-energy behaviour in SOPT is essentially Fermi-liquid-like. We note that the negative peak in $\Im\Sigma$ at zero frequency is much more pronounced for $\delta_{vH} = 0.0068$, while for $\delta_{vH} = 0.1482$ it is smaller by a factor of about five. At higher energies the RG results merge into the SOPT results, and we find that the strong correlations, which develop towards the end of the flow at low energy scales, affect the one-particle spectral properties only at small frequencies. This can be understood from a technical point of view by analysing equations 4.12 and 4.13: Due to the restricted phase space of the infrared propagators D_Λ the RHS only gives non-zero contributions for $|\omega| \lesssim 3\Lambda$. At the same time, the flow of the four-point functions starts to grow strongly only at cutoff values of about $\Lambda \approx 0.7$, as was shown in figure 3.4 for $T = 0.001$. We thus expect sizeable deviations between SOPT and RG flow for $|\omega| \lesssim 2.1$, in agreement with the curves in figure 4.2. We note that smaller differences between the SOPT and the RG flow are found already at higher energies, but they are not relevant for the low-energy physics.

We now focus on the low-frequency region, which determines whether the system shows Fermi-liquid behaviour or not. In figures 4.3, 4.4 and 4.5 we show the results for the three different situations mentioned above. The SOPT results are shown as dash-dotted, black lines, those for $V_{max} = 15$ as dashed, red lines, and the ones for $V_{max} = 150$ as solid, blue lines. Plotted are, from top to bottom, the imaginary part of the self energy, the real part of the self energy and the resulting spectral functions, for each of the six patch points on the Fermi surface.

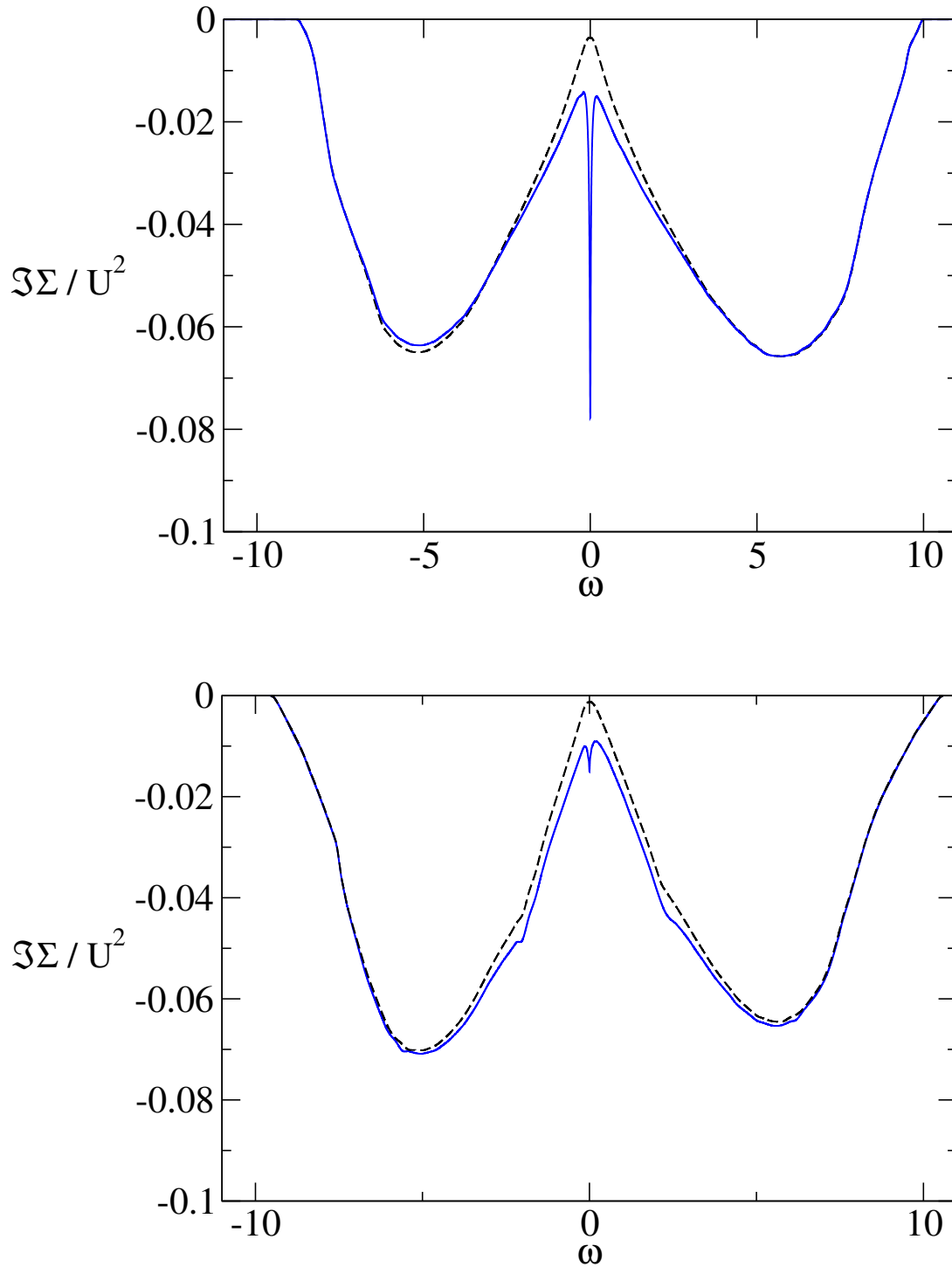


Figure 4.2: Hot spot in first patch (top) and hot spot in third patch (bottom): Imaginary part of the self energy at the respective hot spot for $V_{max} = 150$ (blue, solid line) and in second-order perturbation theory (black, dashed line)

Hot spot in first patch:

We first look at the results presented in figure 4.3, when the first patch point is a hot spot: In second order perturbation theory the self energy shows the usual Fermi-liquid-like behaviour, and the spectral functions have well-defined peaks at $\omega = 0$. The width of the spectral functions is largest at the hot spot and decreases slightly towards the zone diagonal.

For $V_{max} = 15$, a small negative hump appears at zero frequency in $\Im\Sigma$ at the hot spot. At all other patch points the behaviour is different from the SOPT result with respect to the width of the quasi-particle peaks. This width is larger for points closer to the hot spot and leads to a substantial angular dependence of quasi-particle life times, which are smaller when the peaks are wider.

For $V_{max} = 150$, the small hump at the hot spot has evolved into a pronounced negative peak, while at the second patch point a small negative hump appears. On all other patch points we observe that the quasi-particle peaks prevail, but are again wider than for $V_{max} = 15$, leading to even shorter life times.

When it is sufficiently strong, the peak in $\Im\Sigma$ leads to a break-down of the Fermi-liquid picture: the real part of the self energy acquires a positive slope near $\omega = 0$, and the formal definition 4.8 of the quasi-particle weight yields $Z > 1$. Thus, the mere concept of a quasi-particle becomes invalid. The spectral function is no longer peaked at $\omega = 0$, but instead shows two rather broad peaks, with a substantial dip between them, a structure reminiscent of a pseudogap. As noted in the preceding section, equation 4.6, which is the basis for the Fermi-liquid picture, is not valid in general, but only under certain conditions, namely if the self energy can be expanded in a Taylor series in a large enough region around $\omega = 0$. Clearly, this is not the case when the above mentioned peak is present in $\Im\Sigma$. We will come back to this in more detail later in this chapter.

Hot spot in second patch:

In figure 4.4 the results are shown when the second patch is a hot spot. We again observe a negative peak in the imaginary part of the self energy at the hot spot for $V_{max} = 150$, which is now less pronounced, but shows up at the first as well as the second patch. Some remnants of it are seen at the third patch. The resulting spectral functions on the first two patch points do not show a distinct pseudogap feature, but rather a double-hump shape. At all

other patch points the ordinary single-peak behaviour is seen, again with the effect of wider quasi-particle peaks and thus shorter life times as compared to SOPT.

In light of our interest in the importance of hot spots we note that the negative peak in $\Im\Sigma$ is stronger on the first patch point, while the second patch point is the actual hot spot. We interpret this as a competition between \mathbf{Q} -transferring correlations, which have the strongest effect on the second patch point, and a high density of states near the first patch point due to the closeness to the van Hove point $(0, \pi)$.

Hot spot in third patch:

When the chemical potential is further increased such that the third patch point becomes a hot spot, anomalous properties in $\Im\Sigma$ arise only for $V_{max} = 150$, as we can see in figure 4.5. However, we now clearly observe that the hot spot is a special point, since we find a negative peak in $\Im\Sigma$ only at the third patch point, leading to the double-hump spectral function. Furthermore, the width of the quasi-particle peak is larger for patch points closer to the hot spot. This feature evolves when we look at the three sets of results: In SOPT the quasi-particle peaks are rather sharp and the angular dependence of the width is weak, with the widest peak at the patch closest to the van Hove point $(\pi, 0)$. For $V_{max} = 15$ the situation changes. The width of the peaks is larger in the first four patches, and the peak in the second patch is already slightly wider than the one in the first patch. The relevance of self-energy effects due to the flowing four-point function is thus shifted towards the hot spot with increasing renormalised interactions.

These results agree only partially with those obtained very recently by Katanin and Kampf [4], who computed the full frequency dependence of the self energy from the one-particle irreducible version of the fRG [30], with a truncation of the exact hierarchy of flow equations at the same order as in our calculation. For a Fermi momentum very close to a van Hove point, they obtained a single peak in $\Im\Sigma$ resulting in a double peak in the spectral function, in agreement with our calculation. However, for Fermi momenta at some moderate distance from the van Hove point they found a double peak in $\Im\Sigma$ leading to a three-peak structure in the spectral function, which we do not observe in our results. In both approaches, Wick-ordered as well as one-particle irreducible fRG, the peaks in $\Im\Sigma$ are generated by strongly enhanced effective interactions, and are thus most pronounced at temperatures close to the instability scale T_c . The different structure of $\Im\Sigma$ obtained from the two fRG versions can be traced back to a different division of momentum integrals in high- and low-energy modes. In both cases

the energy variable ω is related to the excitation energies on internal lines: $\omega = \xi_{\mathbf{q}}^0 - \xi_{\mathbf{p}}^0 + \xi_{\mathbf{k}+\mathbf{p}-\mathbf{q}}^0$ in equation 4.12, and analogously $\omega = \xi_{\mathbf{p}}^0 - \xi_{\mathbf{q}}^0 + \xi_{\mathbf{k}+\mathbf{q}-\mathbf{p}}^0$ in equation 4.13. In the Wick-ordered scheme all excitation energies are at or below the cutoff, that is $|\xi| \leq \Lambda$. As a consequence, the flow for $\Im\Sigma^\Lambda(\mathbf{k}, \omega)$ with $\omega \neq 0$ stops completely for $\Lambda < |\omega|/3$. In a situation where the vertex Γ_Λ grows strongly at very small scales, $\Lambda \rightarrow 0$, the imaginary part of the self energy therefore receives the corresponding large contributions only for small frequencies, which leads necessarily to a single peak with maximal height at $\omega = 0$. By contrast, in the two-loop diagram generating the flow of $\Im\Sigma^\Lambda$ in the one-particle irreducible scheme one excitation energy is at scale Λ , the second at a scale $\Lambda' > \Lambda$, and the third one *above* the scale Λ' , where Λ' is the scale of the vertex $\Gamma^{\Lambda'}$ in the diagram. Note that the two-loop diagram for the self energy in the one-particle irreducible fRG is non-local in the cutoff. The crucial point is that not all excitation energies are bounded by the cutoff. Therefore, the flow of $\Im\Sigma^\Lambda(\mathbf{k}, \omega)$ does not stop for $\Lambda \ll |\omega|$, and the strong enhancement of $\Gamma^{\Lambda'}$ for $\Lambda' \rightarrow 0$ does not necessarily enhance $\Im\Sigma^\Lambda(\mathbf{k}, \omega)$ most strongly for the smallest energies. However, to obtain a double peak in $\Im\Sigma$ with maxima at finite frequencies, say ω_\pm , the contribution with at least one excitation energy of order ω_\pm must be particularly large. This is possible only if the vertex is not enhanced most strongly for cases with all ingoing and outgoing momenta on the Fermi surface, but rather for some interaction processes with at least one momentum away from the Fermi surface. One should also keep in mind that contributions from momenta away from the Fermi surface might be overestimated in the one-particle irreducible fRG with a momentum discretization by patches, since the dependence of the vertex Γ^Λ normal to the Fermi surface is weak only within a shell $|\xi_{\mathbf{k}}^0| < \Lambda$ in momentum space.

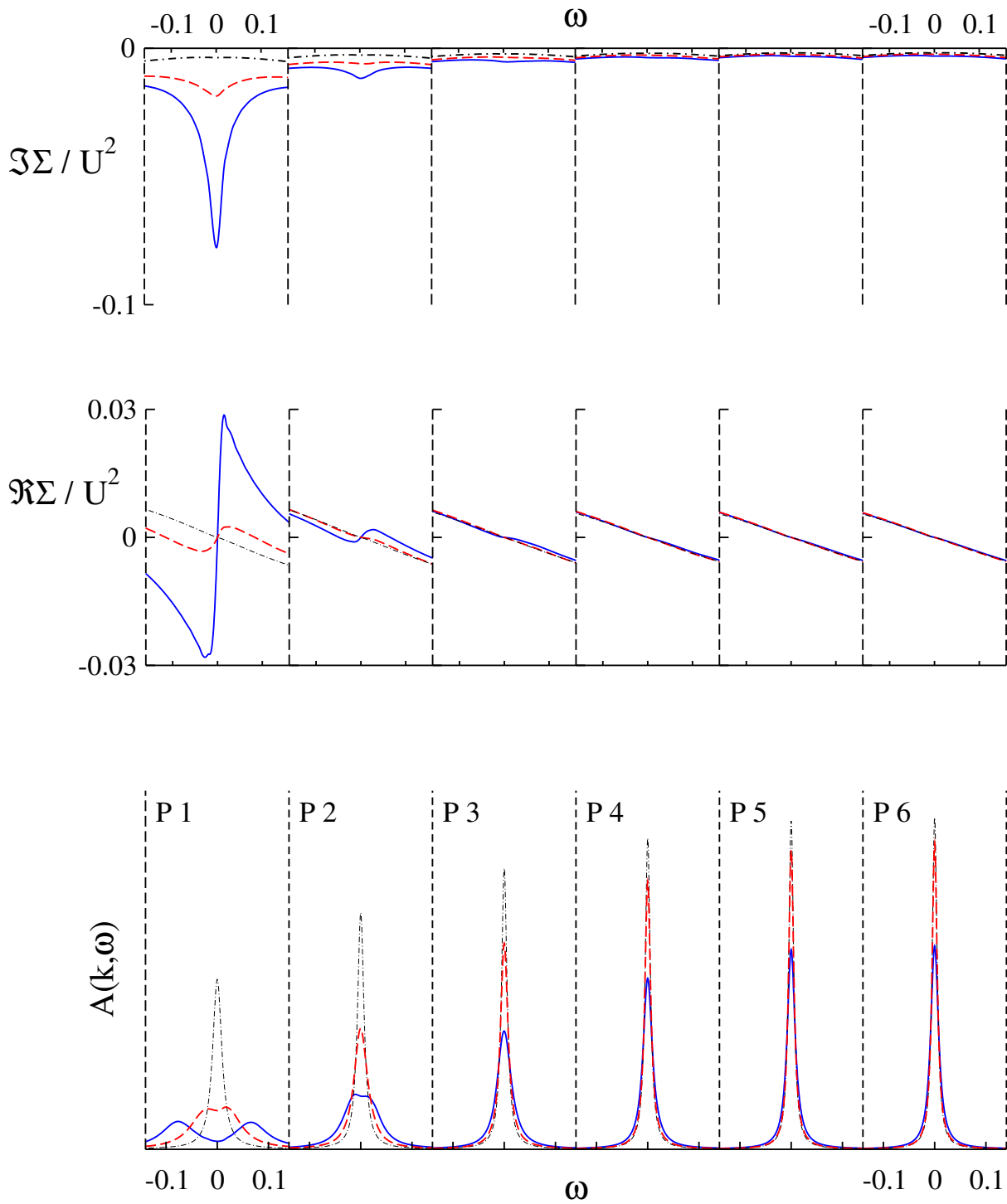


Figure 4.3: Hot spot in first patch: Self energy and spectral function on different patches along the Fermi surface for $V_{max} = 150$ (solid, blue line), $V_{max} = 15$ (dashed, red line) and in second order perturbation theory (dash-dotted, black line).

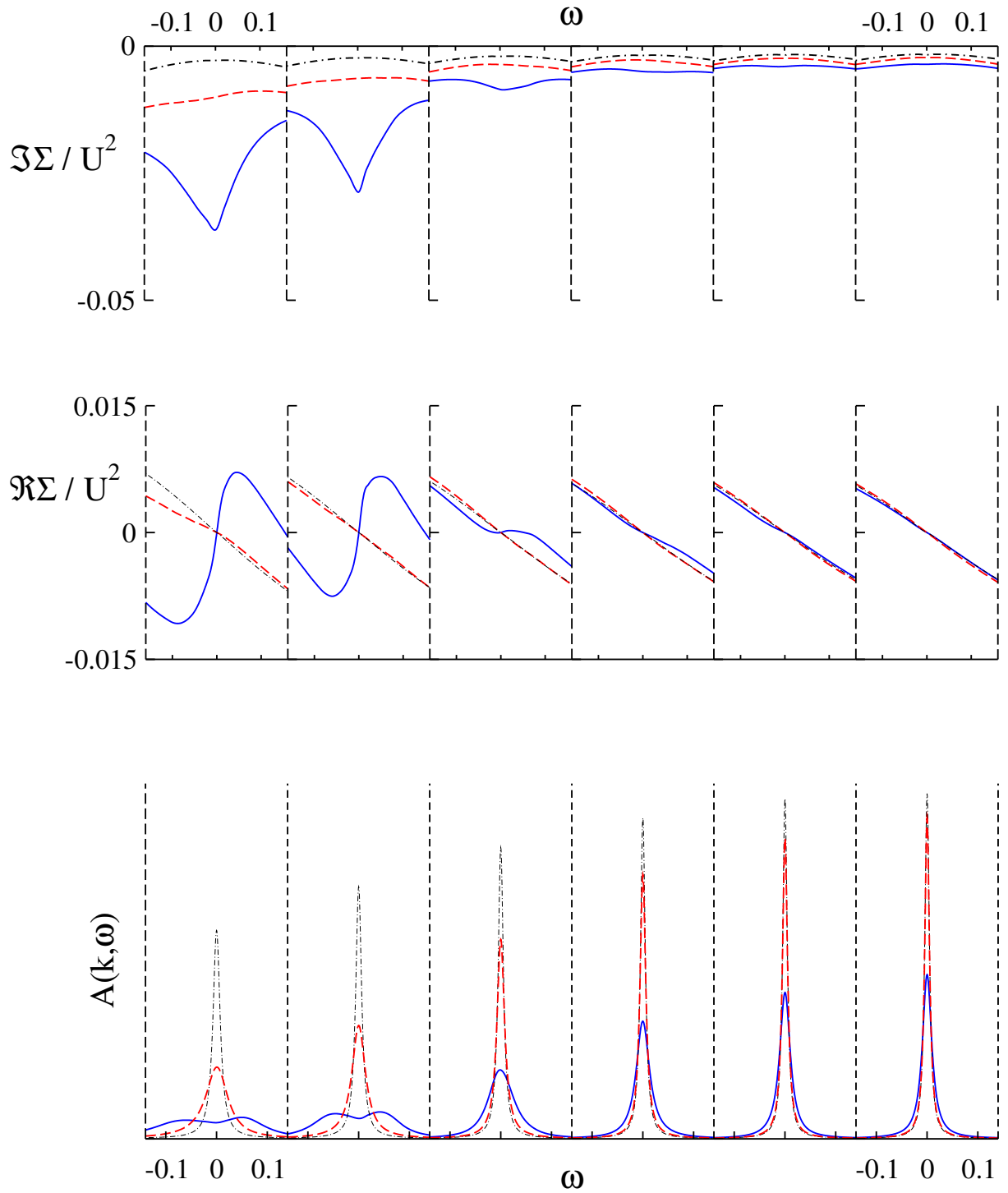


Figure 4.4: Hot spot in second patch: Self energy and spectral function on different patches along the Fermi surface for $V_{max} = 150$ (solid, blue line), $V_{max} = 15$ (dashed, red line) and in second order perturbation theory (dash-dotted, black line)

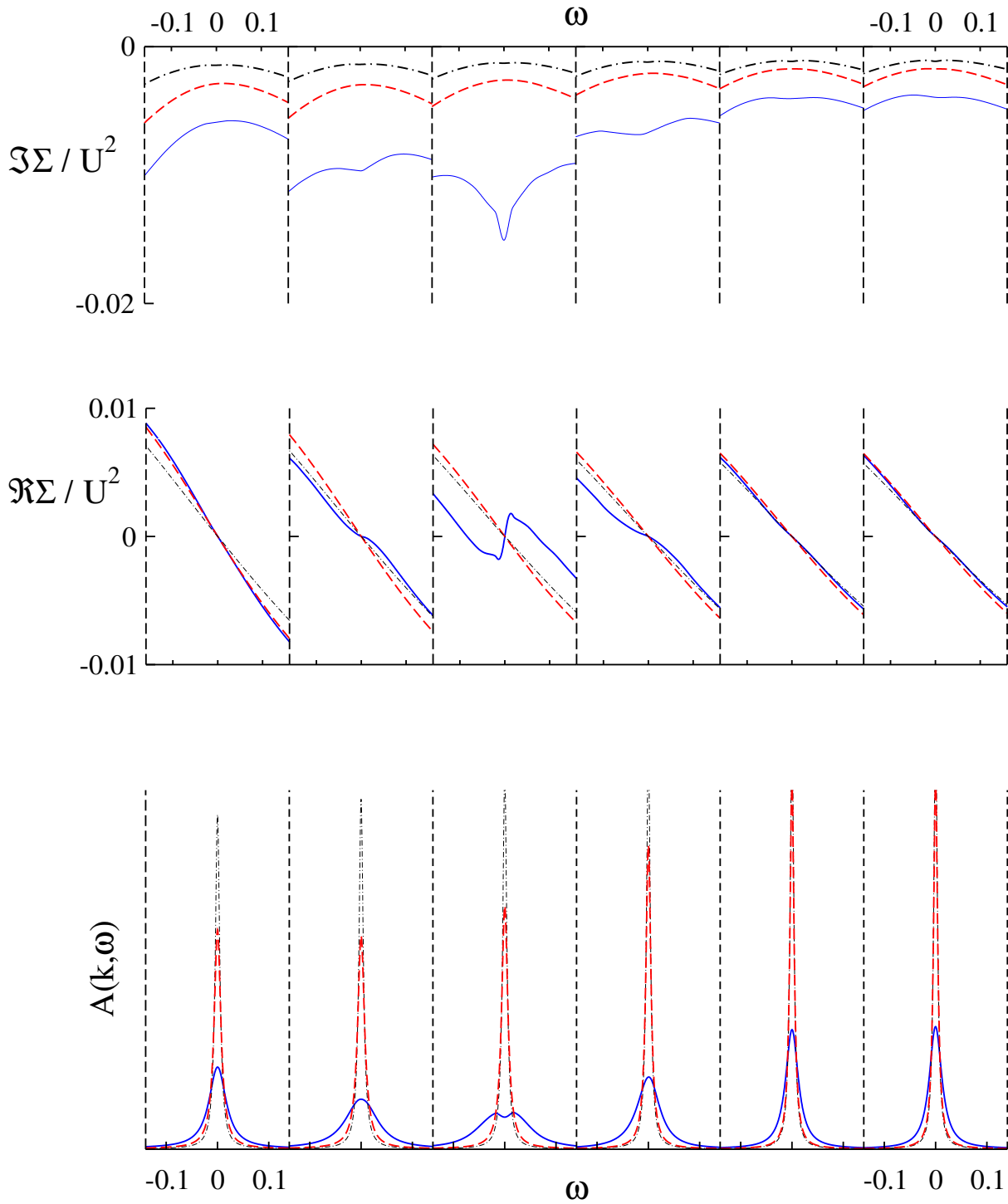


Figure 4.5: Hot spot in third patch: Self energy and spectral function on different patches along the Fermi surface for $V_{max} = 150$ (solid, blue line), $V_{max} = 15$ (dashed, red line) and in second order perturbation theory (dash-dotted, black line)

In the following we will look in more detail at the character and evolution of non-Fermi-liquid-like behaviour, our definition of which was the non-validity of equations 4.4 and 4.5, and which is caused here by the appearance of a sharp peak in the imaginary part of the self energy at zero frequency. This in turn leads to an unusual slope of the real part of the self energy around zero frequency, which makes the notion of a quasi-particle, and thus also the definition of a quasi-particle weight, inappropriate. To analyse this effect quantitatively we look at the frequency derivative $\partial_\omega \Re\Sigma(0, \mathbf{k}_{HS}) := \frac{\partial}{\partial\omega} \Re\Sigma(\omega, \mathbf{k}_{HS})|_{\omega=0}$ as well as $\Im\Sigma(0, \mathbf{k}_{HS})$ for $\delta_{vH} = 0.0586$, when the hot spot momentum \mathbf{k}_{HS} is in the second patch. When $\partial_\omega \Re\Sigma(0, \mathbf{k}_{HS}) > 0$ the formal definition of the quasi-particle weight yields $Z > 1$, already indicating the failure of the quasi-particle concept. For $\partial_\omega \Re\Sigma(0, \mathbf{k}_{HS}) > 1$ we obtain additional solutions for equation 4.3 at small finite frequencies slightly above and below $\omega = 0$, and the pseudogap feature appears. The evolution of this scenario is illustrated in figure 4.6, where the low-energy part of $\Re\Sigma(0, \mathbf{k}_{HS})$ is shown for different temperatures, along with the corresponding spectral functions, at the hot-spot momentum \mathbf{k}_{HS} .

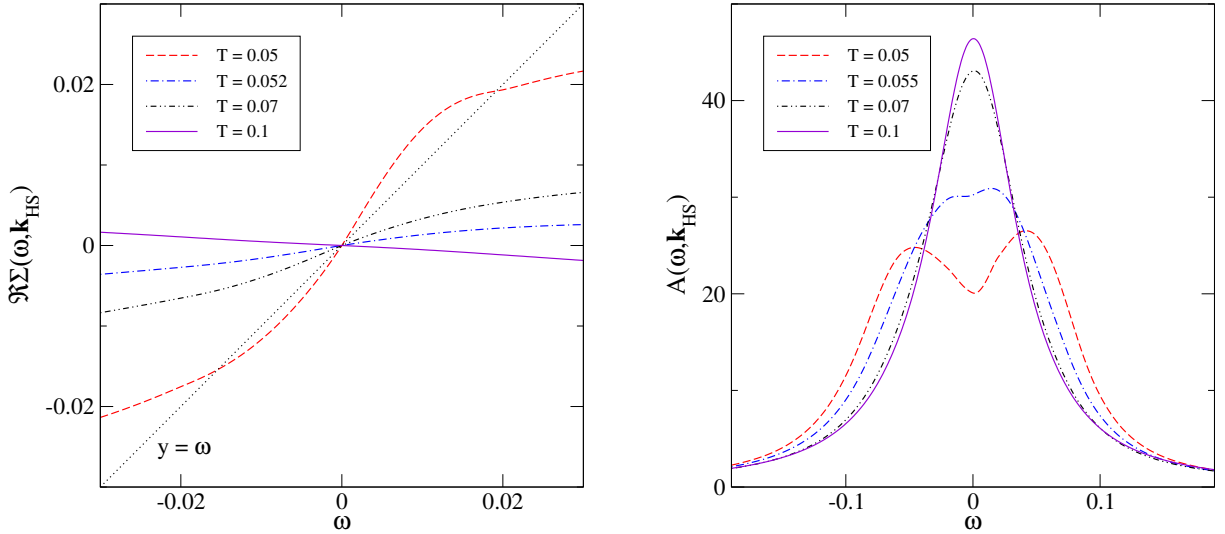


Figure 4.6: Low-frequency plots of the real part of the self energy (left) and the corresponding spectral functions (right) at the hot-spot momentum \mathbf{k}_{HS} for increasing temperature. ($\delta_{vH} = 0.0586$, $U = 1.8625$, hot spot in second patch)

While the pseudogap is only present for temperatures in the vicinity of T_c , we note that the condition $\partial_\omega \Re\Sigma(0, \mathbf{k}_{HS}) > 0$ extends to much higher temperatures. Figure 4.7 shows how $\partial_\omega \Re\Sigma(0, \mathbf{k}_{HS})$ and $\Im\Sigma(0, \mathbf{k}_{HS})$ at the hot spot behave as functions of temperature, along with the results in SOPT. The sign change in $\partial_\omega \Re\Sigma(0, \mathbf{k}_{HS})$, and thus the change from $Z > 1$ to $Z < 1$, occurs around $T = 0.075$, and for $T = 0.1$ the RG data starts to approach the SOPT

value. Similarly, $\Im\Sigma(0, \mathbf{k}_{HS})$ decreases with increasing temperature, yet remains significantly larger than the SOPT value, for instance at $T = 0.1$ by a factor of about two.

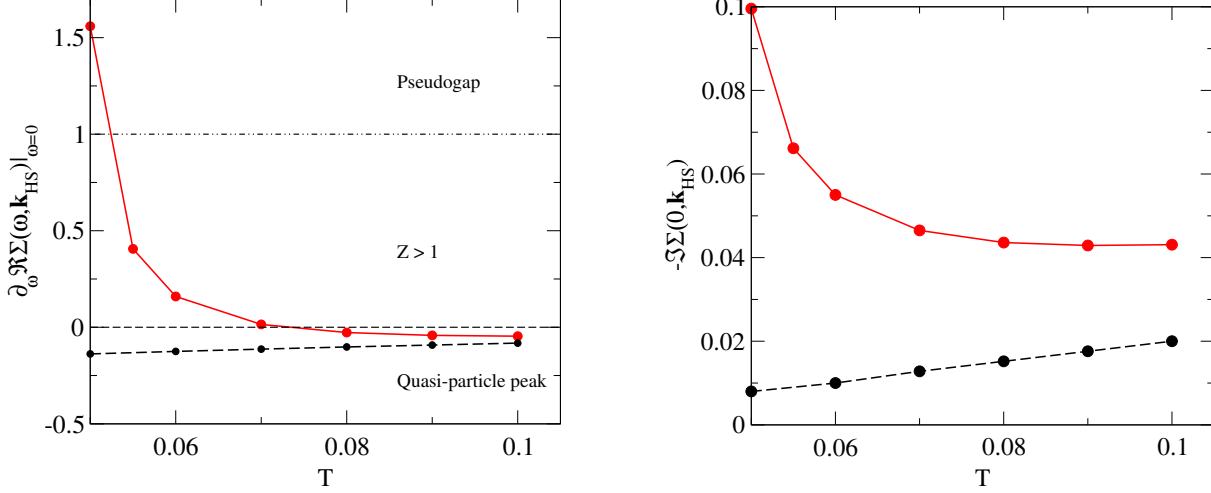


Figure 4.7: Temperature dependence of the slope of $\Re\Sigma(\omega, \mathbf{k}_{HS})$ at $\omega = 0$ (left) and $\Im\Sigma(0, \mathbf{k}_{HS})$ (right) at the hot-spot momentum \mathbf{k}_{HS} . Red, solid lines RG - black, dashed lines SOPT. ($\delta_{vH} = 0.0586$, $U = 1.8625$, hot spot in second patch)

Concerning the angular dependence of $\partial_\omega \Re\Sigma(0, \mathbf{k}_{HS})$ which is shown in figure 4.8 we observe that for $\delta_{vH} = 0.0586$, $U = 1.8625$ and $T = 0.05$ there is not only the observed pseudogap structure in the first and second patch, but we also have $Z > 1$ in the third patch. The above-defined deviation from the quasi-particle picture thus extends over a significant region along the Fermi surface. It is interesting to note that the slope of $\Re\Sigma(\omega, \mathbf{k}_{HS})$ at $\omega = 0$ has its maximum at the hot spot, while $\Im\Sigma(0, \mathbf{k}_{HS})$ is actually largest in the first patch, which is closest to the van Hove point $(\pi, 0)$ due to a larger background contribution. Had we focussed merely on the imaginary part of the self energy, as was done in [2], the hot spot would not have emerged as a special point.

Next we look at the evolution of the non-Fermi-liquid-like features as the interaction is varied at fixed temperature, thus equalising thermal effects. In figure 4.9 we see a qualitatively similar behaviour as in figure 4.7. For smaller values of the bare interaction, and thus smaller renormalised couplings, $\partial_\omega \Re\Sigma(0, \mathbf{k}_{HS})$ approaches the SOPT curve already for $U \leq 1.6$, while $\Im\Sigma(0, \mathbf{k}_{HS})$ is more sensitive to correlations in that for $U = 1.6$ it remains larger by a factor of two as compared to the SOPT result.

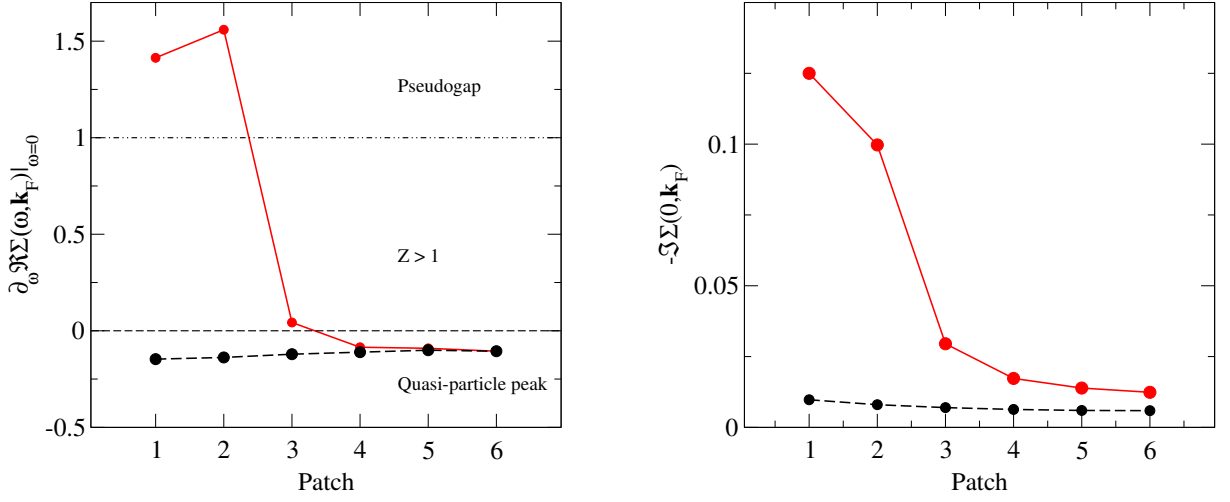


Figure 4.8: Tangential dependence of the slope of $\Re\Sigma(\omega, \mathbf{k})$ at $\omega = 0$ (left) and $\Im\Sigma(0, \mathbf{k}_{HS})$ (right) along the Fermi surface. Red, solid lines RG - black, dashed lines SOPT. ($\delta_{vH} = 0.0586$, $U = 1.8625$, hot spot in second patch)

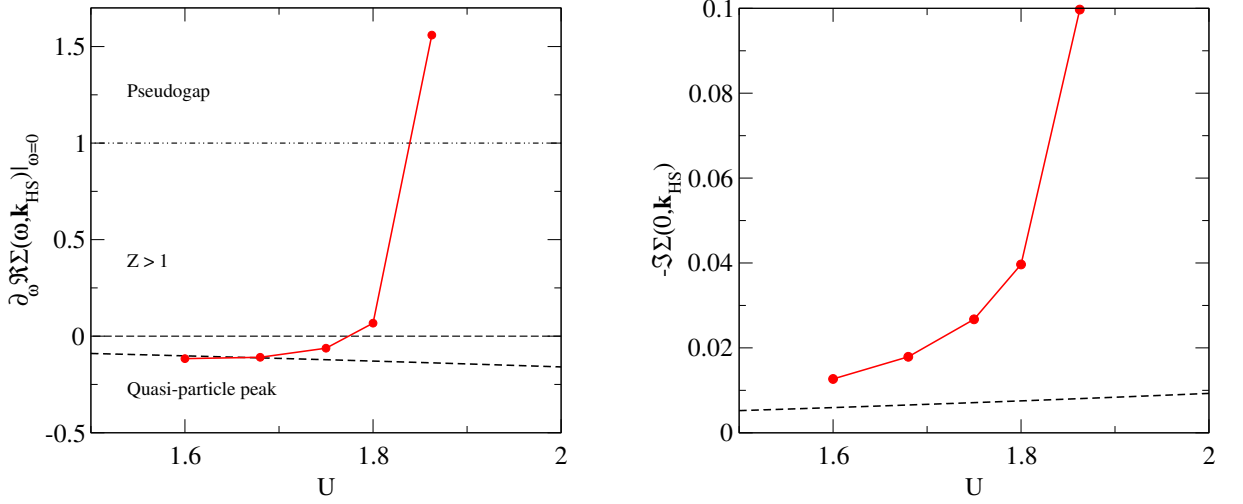


Figure 4.9: Dependence of the slope of $\Re\Sigma(\omega, \mathbf{k}_{HS})$ at $\omega = 0$ (left) and $\Im\Sigma(0, \mathbf{k}_{HS})$ (right) at the hot-spot momentum \mathbf{k}_{HS} on the bare interaction U . Red, solid lines RG - black, dashed lines SOPT. ($\delta_{vH} = 0.0586$, $T = 0.05$, hot spot in second patch)

So far we have seen that the quasi-particle picture is invalid if the condition $Z < 1$ is not satisfied. It turns out that also for $Z < 1$, when the derivative $\partial_\omega \Re\Sigma(0, \mathbf{k})$ is negative, we may still observe deviations from the usual behaviour of the self energy. This is illustrated in figure 4.10, where we plot spectral data for $\delta_{vH} = 0.0586$, $T = 0.05$ and $U = 1.75$ at the hot-spot

momentum. The inset shows the low-frequency part of $\Re\Sigma(0, \mathbf{k})$, which is linear in the interval $\omega \in (-0.1, 0.1)$, yielding a value of $\partial_\omega \Re\Sigma(0, \mathbf{k}) \approx 0.0622$ at $\omega = 0$. However, outside this interval we find a different, also linear behaviour in a range $|\omega| \in (0.1, 0.2)$. Taking the derivative of the real part not at $\omega = 0$ but at $\omega = -0.15$ yields $\partial_\omega \Re\Sigma(-0.15, \mathbf{k}) \approx 0.1175$. The functions $y = -0.0622\omega$ and $y = -0.1175\omega$ can both serve as more or less reasonable approximations in the low-energy region, as is seen in the inset in figure 4.10. Plugging either one into equation 4.7 we obtain two different quasi-particle Lorentzians $A^{QP}(\omega, \mathbf{k})$. Both agree well with the central peak of the spectral function, which is not too surprising, since the value of both functions A^{QP} at zero frequency is identical by means of equation 4.7, and the values for the quasi-particle weights are reasonably close to each other. We plot the differences $A(\omega, \mathbf{k}) - A^{QP}(\omega, \mathbf{k})$ for both cases to extract the incoherent part of the spectral function, and find that both are small in the low-frequency region. It is interesting to see that in the case when the approximation $\Re\Sigma(\omega, \mathbf{k}) \approx -0.1175\omega$ is used, the incoherent part actually exhibits a structure very similar to the pseudogap feature discussed before, and does not appear to be “truly incoherent” after all.

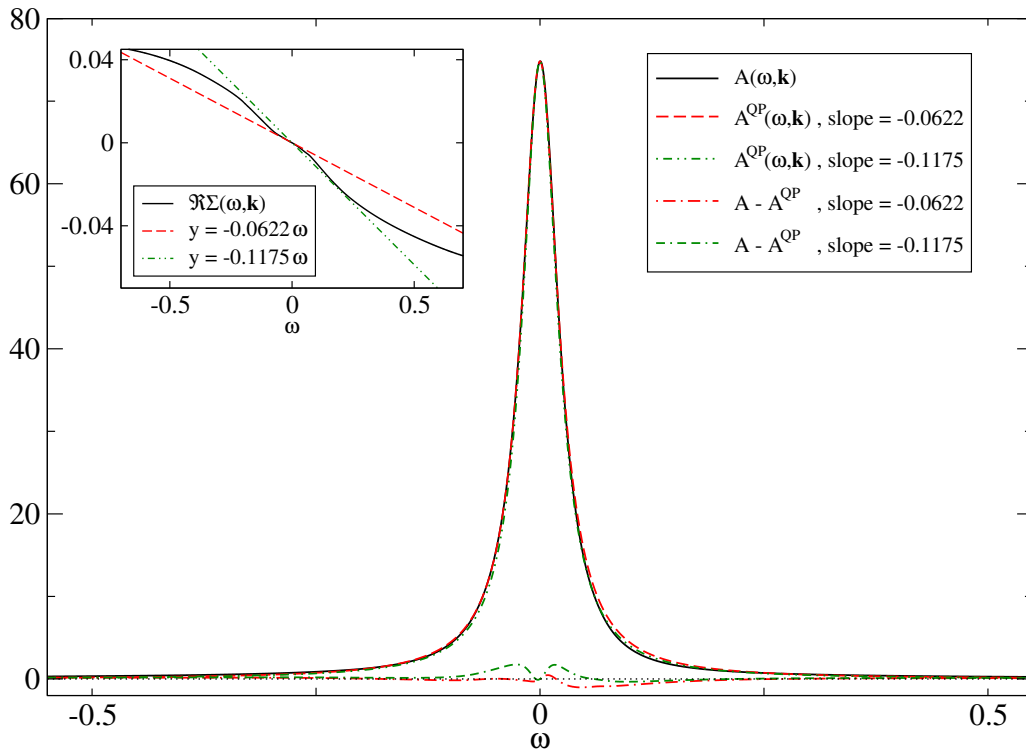


Figure 4.10: Spectral function and two tentative quasi-particle Lorentzians, together with the respective incoherent parts $A(\omega, \mathbf{k}) - A^{QP}(\omega, \mathbf{k})$, as obtained from the low-energy behaviour of the real part of the self energy shown in the inset, at the hot-spot momentum \mathbf{k}_{HS} . ($\delta_{vH} = 0.0586$, $T = 0.05$, $U = 1.75$, hot spot in second patch)

Origin of the Pseudogap

The dip in the spectral function, observed predominantly at and near the hot spots, is clearly due to the strong correlations which develop when a critical temperature is approached, and can be interpreted as the onset of pseudogap behaviour in the spectral function. We have seen in chapter 3 that in general two types of correlations become strong near a critical scale, namely superconducting as well as antiferromagnetic correlations, and we may ask which of the two, if not both, are responsible for the spectral anomalies.

To answer this question we use a simple trick: We can focus on the importance of either contribution, Cooper couplings or \mathbf{Q} -transfer couplings, by neglecting the contribution of the other one on the RHS of the flow equation for the two-point function. In practice this means we conduct two additional calculations for each of the three values for δ_{vH} and the case $V_{max} = 150(\Lambda \rightarrow 0)$: One in which $V_{\Lambda}^{s,t}(i, j, k)$ is set to the bare interaction in the two-loop diagram for the self energy, except when it is a Cooper coupling, and one in which $V_{\Lambda}^{s,t}(i, j, k)$ is set to the bare interaction in the two-loop diagram for the self energy, except when it is a \mathbf{Q} -transfer coupling. To be precise, in the latter we include couplings where the patches j and k can be transformed into each other by a shift of \mathbf{Q} . This means all scattering processes with momentum transfer parallel to \mathbf{Q} are included, some of which have a momentum transfer close to but not exactly \mathbf{Q} . However, the \mathbf{Q} -transfer couplings are largest within this set of couplings. We can then analyse the effect of the respective correlations on the imaginary part of the self energy in the limit $\Lambda \rightarrow 0$.²

The outcome of this procedure is shown in figure 4.11, where the low-energy behaviour of the imaginary part of the self energy is shown for $\delta_{vH} = 0.0068$, $\delta_{vH} = 0.0586$ and $\delta_{vH} = 0.1482$, for momenta located at the respective hot spots. Plotted are the results for the case when only the flow of Cooper couplings feeds into the flow of the self energy, as well as for the case when only the flow of \mathbf{Q} -transfer couplings feeds into the flow of the self energy, and also the “full” result.

For $\delta_{vH} = 0.0068$, when the first patch point is a hot spot, we see that both channels cause a negative peak in $\Im\Sigma$. We recall from the previous section that there always is an overlap between the Cooper channel and the \mathbf{Q} -transfer channel. The coupling $V^S(1, 29, 13)$ belongs

²We note that this strategy is somewhat ambiguous since it depends on the size, and thus the number, of patches, i.e. the level of discretisation. In the limit of infinitely many patches the channels we select are of measure zero and would thus not yield any contribution at all. We would then need to select a certain finite region in momentum space centred around these special subsets. In order to obtain a consistent and meaningful comparison, the size of these regions would then, roughly speaking, be chosen as the size of the patches as given in the discretisation used here.

to this class and is one of the strongest in this parameter range. Therefore, it does not make much sense to ask whether superconducting correlations *or* antiferromagnetic correlations are responsible for the dip in the spectral function – it is actually both.

For $\delta_{vH} = 0.0586$ the Fermi surface moves away from the van Hove scale, and we see that the contribution of Cooper couplings to the negative peak in $\Im\Sigma$ is reduced, while the contribution of \mathbf{Q} -transfer couplings accounts for most of the anomalous low-energy features.

This tendency continues when looking at the case $\delta_{vH} = 0.1482$. There, the contribution due to Cooper couplings only causes a faint hump in $\Im\Sigma$, while \mathbf{Q} -transfer couplings have a much greater impact on the self energy, albeit less pronounced than for $\delta_{vH} = 0.0068$.

We can relate these findings to existing theories of the pseudogap. The idea that antiferromagnetic correlations can cause a pseudogap in the one-particle spectral function was substantiated by Kampf and Schrieffer in 1990 in the so-called spin-bag picture [57]. Within the subsequently developed nearly-antiferromagnetic Fermi-liquid (NAFL) concept put forward by Monthoux, Pines, Schmalian et al. [58–66] the pseudogap behaviour is explained on the basis of a phenomenological description of strong antiferromagnetic correlations, and the potential importance of hot and cold parts on the Fermi surface is recognised.

Other studies have aimed at calculating one-particle spectral properties starting from more microscopic descriptions. Early fluctuation-exchange (FLEX) calculations by Dahm et al. do not find a pseudogap in the one-particle spectral function, but only in the density of states [67, 68]. Later, they found traces of a pseudogap behaviour in refined FLEX calculations, which they attribute to superconducting pair fluctuations [69]. An excellent detailed description of this type of approach is given in [70].

Also, in a type of RG-accelerated self-consistent FLEX scheme no signs of non-Fermi-liquid behaviour are seen [71]. In contrast, Yanase employed a similar scheme and found clear pseudogap behaviour, the details of which depend on the details of the approximation [72, 73]. He also finds that it is the superconducting fluctuations that generate the pseudogap behaviour. It is interesting to note that there one finds a pseudogap in a non-selfconsistent treatment, or a pseudogap plus a narrow single-particle peak at $\omega = 0$ for a self-consistent calculation, as seen in [4].

The pseudogap phenomenon is also found within the two-particle self-consistent (TPSC) approach, a non-perturbative method developed and extensively employed by Vilk, Tremblay et al. [74–82]. From these results it is inferred that strong antiferromagnetic correlations are responsible for the pseudogap. Simultaneously, S en echal and Tremblay observe the pseudogap in cluster perturbation theory at intermediate and strong coupling [83]. There, at weaker

bare interaction the pseudogap appears first at the hot spots, while for larger interaction a whole region of the Fermi surface around the zone diagonal is affected.

Saikawa and Ferraz have found a single-particle pseudogap for $t' = 0$ at different fillings within the paramagnon theory [84,85], which is based on a non-selfconsistent random-phase approximation, and have compared the results to those obtained in TPSC [85]. The paramagnon theory is closely related to the NAFL scenario in the sense that it specifies the microscopic origin of the interaction due to strong antiferromagnetic correlations. However, it completely neglects vertex corrections, which are included implicitly in the TPSC method. The paramagnon theory, just like the RG calculation presented in this work, neglects order-parameter fluctuations, and thus yields a finite transition temperature in two dimensions, inconsistent with the Mermin-Wagner theorem. The TPSC always forces T_c to zero, which is in accordance with Mermin-Wagner. However, the finite critical Kosterlitz-Thouless behaviour, namely an infinite correlation length below a finite critical temperature, is not found either. In fact, the TPSC shows the same critical behaviour as an $\mathcal{O}(N)$ model for $N \rightarrow \infty$, which explains the too-strong suppression of the transition temperature in two dimensions [76].

Recently, a strong negative peak in $\Im\Sigma(0, \mathbf{k}_F)$ and the resulting pseudogap was also found within the dynamical cluster approximation (DCA) by Hushcroft et al. [86] at as well as slightly away from half filling. At half filling the pseudogap is attributed to short-range antiferromagnetic correlations, while away from half filling also superconducting correlations in the d -wave channel appear, and the cause of the pseudogap is not clear. These results are obtained using values for the bare interaction of $U = 5.2$ and $U = 6$. Pseudogap behaviour has also been observed in a strongly frustrated system treated by Parcollet et al. within a cluster extension of dynamical mean-field theory (CDMFT) for $U \geq 8$ [87]. There, the pseudogap appears near a Mott transition, and it is not clear whether it can be attributed to any specific kind of strong correlations, or if it is a more general property of a system near a Mott transition. These results are consistent with the work by Sénéchal and Tremblay, where the Mott physics is attributed to short-range correlations [83]. In addition, the pseudogap also appears within purely numerical methods. Preuss et al. found it in quantum Monte-Carlo calculations on a finite 8×8 system for $U = 8$ away from half filling, and attribute it to antiferromagnetic correlations [88]. Despite the fact that the interactions used in these calculations may lie well outside the range of weak interaction, they are nevertheless consistent with our findings.

In light of the above discussion there seems to be no consensus concerning the origin of the pseudogap. At weak coupling, antiferromagnetic and superconducting fluctuations are valid candidates, which we can confirm from our results. However, we stress that while we see a

pseudogap in a sizeable region of parameter space, its origins need not be identical at different points within that region. To be specific, near van Hove filling the correlations are peaked around a point of degeneracy of Cooper and \mathbf{Q} -transfer couplings, and we thus cannot separate their respective importance. The further we move away from van Hove filling towards larger densities, the less influential are the correlations in the Cooper channel concerning the spectral properties at the hot spots, while correlations in the \mathbf{Q} -transfer channel, in particular umklapp components, remain active with respect to their influence on the one-particle spectral properties.

4.6 Discussion

The results presented in this chapter show how strong correlations which develop close to a critical energy scale can severely affect single-particle properties. At so-called hot spots, that is points where the Fermi surface intersects the umklapp surface, large renormalised couplings lead to the emergence of a sharp negative peak in the imaginary part of the self energy at low frequencies, and consequently to a pseudogap feature in the single-particle spectral function. In this case, the quasi-particle picture becomes invalid. Previous fRG calculations focussing on the flow of the quasi-particle weight Z [19, 37, 89] did not resolve this feature, which is not too surprising since the mere concept of defining a quasi-particle weight is invalid in the region of interest.

The first results for the full frequency dependence of the self energy using fRG were obtained very recently by Katanin and Kampf, who also find a pseudogap structure due to strong correlations, but for certain momenta on the Fermi surface they find a narrow quasi-particle peak in the middle of the pseudogap, which we do not see in our calculation [4]. While we have an understanding of this discrepancy on a technical level, there remains uncertainty concerning the true physical behaviour.

One of the major objectives of a theory is of course to explain experimental facts. While it is common to compare theoretical results for the 2D-HM with data for High- T_c cuprates, there are a number of difficulties involved. Concerning one-particle spectral properties, it is tempting to compare the spectral functions we have obtained to experimentally measured angle-resolved photoemission spectra. Doing this, we find that some data obtained by Armitage et al. indeed shows that a pseudogap feature develops near points where the Fermi surface intersects the Umklapp surface [90, 91]. However, this is not observed generically, but only in a certain parameter regime. Furthermore, recent data published by Claesson et al. does

not confirm this [92]. Unfortunately, there are substantial difficulties involved also on the experimental side, and what are claimed by some to be experimental “facts”, are argued to be “artefacts” by others. Just as in chapter 1 it is not our goal to enter the discussion about such issues. Rather, we recognise it as a matter of trial and error filtering out the wrong theories, in order to eventually arrive at the “truth” – a prescription strongly recommended by P. W. Anderson [93].

What we have presented in this chapter concerning spectral properties of a certain type of strongly correlated system is one piece in a big puzzle, and will hopefully help understand the physics of correlated electron systems. To what extent it describes the physics correctly remains to be seen, but it offers a plausible physical picture which either needs to be confirmed or ruled out. In particular, the discrepancy between our results and the findings by Katanin and Kampf [4] is an issue which has to be resolved, since we have two distinct physical scenarios, which are both plausible but contradict each other; even more so since they are both obtained by fRG methods.

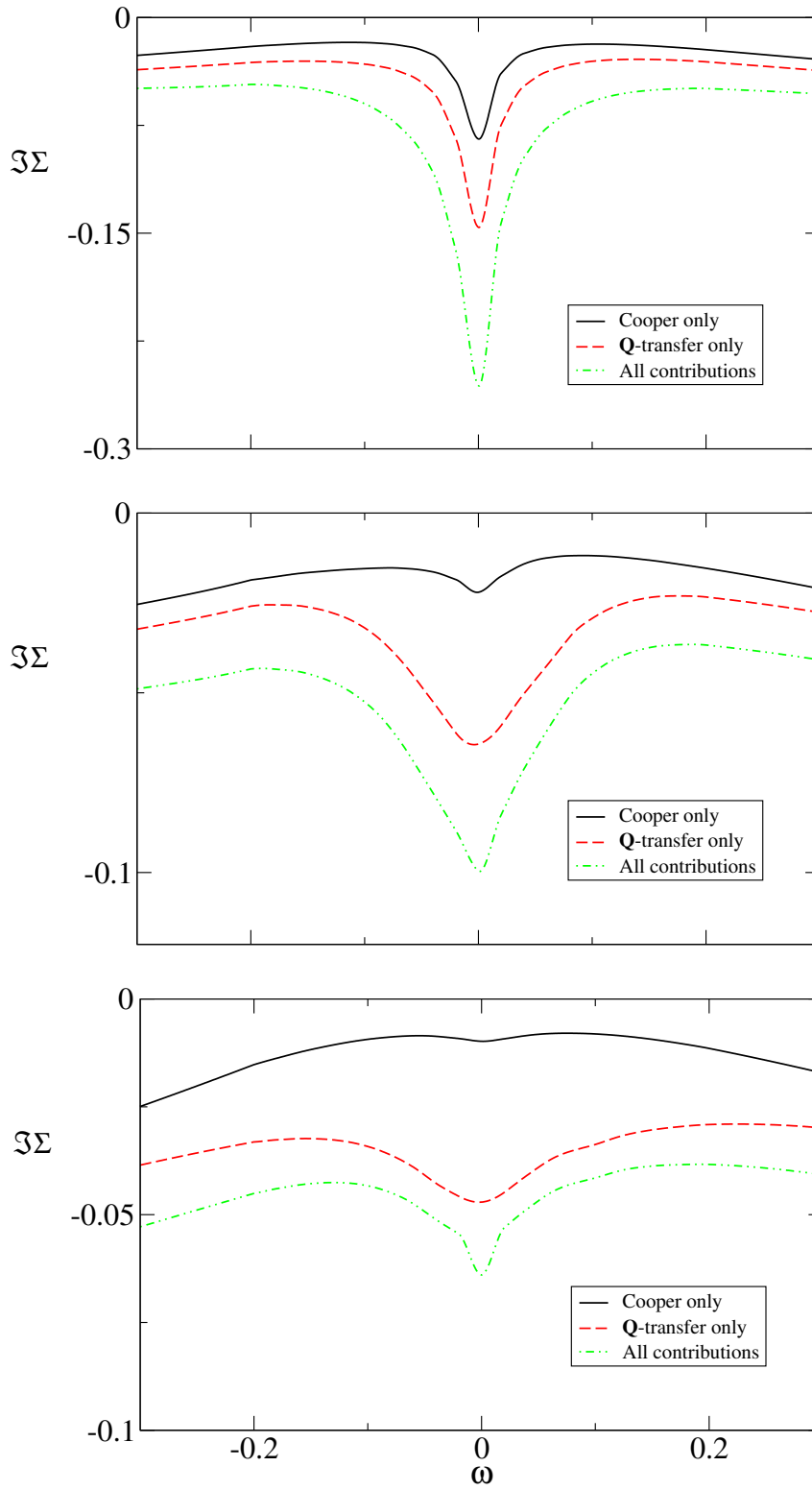


Figure 4.11: Contributions of different correlations to $\Im\Sigma$ at the respective hot spots for $\delta_{vH} = 0.0068$, $\delta_{vH} = 0.0586$ and $\delta_{vH} = 0.1482$.

Chapter 5

Discussion and Conclusion

In this thesis we have applied the functional renormalisation group (fRG) to the two-dimensional Hubbard model (2D-HM). We have done this by solving approximate renormalisation group equations for the self energy and the two-particle interaction numerically. The purpose of these calculations was two-fold in the sense that we wanted to learn about the reliability of the method on the one hand, and about the physics of the 2D-HM on the other.

We found that different fRG schemes agree in describing the mutual interplay and the resulting competition between different correlations, but also that the results sometimes differ quantitatively. This sharpens our perception when it comes to interpreting fRG results, and tells us that we have to separate the indicative character from the quantitative aspects of the results. The main line of arguments presented in previous fRG studies is confirmed, that in the weak-coupling region particle-hole correlations feed back into the particle-particle channel, triggering strong superconducting correlations in a non-zero parameter range.

Concerning the physics of the 2D-HM we have shown new results for the single-particle spectral functions for the case of a Fermi surface which is not perfectly nested and intersects the Umklapp surface at so-called hot spots. These results were obtained from the Wick-ordered fRG scheme, and the calculations were done directly on the real frequency axis. We found that close to a critical temperature T_c where correlations become strong, a dip appears in the single-particle spectral functions for momenta close to and at the hot spots, a behaviour summarised in figures 4.3 – 4.5. Away from the van Hove scale, this is traced back to strong correlations in the particle-hole channel and attributed to antiferromagnetic fluctuations, in agreement with numerous previous studies. For a Fermi surface at or very close to the van Hove scale, there exists a degeneracy in the sense that the strongest correlations are found around a point in coupling space which is relevant for both superconductivity and antiferromagnetism, and we can thus not distinguish between the importance of the respective fluctuations.

In addition, we have outlined in detail the approximations which are made to be able to put the fRG equations on the computer and solve them in a reasonable amount of time. Some of these approximations have brute-force character, and we emphasise here that it remains to be investigated how big the deviations from the "true" answers actually are. The validity is restricted to the weak-coupling regime, yet we integrate to couplings which may well lie outside this limit. It is therefore desirable to improve on each step in the approximation to learn more about the inner workings of numerical solutions of fRG equations. Extending the fRG calculations presented here to higher loops, and/or incorporating the feedback of the two-point function on the RHS of the RGE is expected to improve quality and accuracy of the results. This can be done systematically and would at least in part account for fluctuations which are particularly important in two dimensions. However, this is a formidable task, since a number of rather high obstacles have to be overcome to implement these extensions in a numerical calculation. We are confident that with the continuous development of computational resources and ongoing progress of numerical implementations of the fRG this will be within reach in the near future.

Finally, we remark that fRG methods are not restricted to the Hubbard model or closely related problems, but are rather general concerning their applicability. For example, they have been applied very successfully to spinless fermions in one dimension (see for example [5] and references therein). Furthermore, they are very flexible with respect to the choice of the parameter controlling the flow. It does not need to be a cutoff in energy or momentum space, but may also be chosen for example as the temperature [6] or even the interaction strength [8].

Appendix A

Polchinski and Wiczerkowski Equations

Here we outline the derivation of the Polchinski equation and the subsequent transformation to the Wiczerkowski equation. We start from the generating functional for connected, C -amputated Green functions,

$$\mathcal{G}^{ac}[\bar{\eta}, \eta] = \log \int d\mu_C [\bar{\psi}, \psi] e^{S_I[\bar{\psi}-\bar{\eta}, \psi+\eta]}, \quad (\text{A.1})$$

where

$$d\mu_C := \det C \mathcal{D}(\bar{\psi}, \psi) e^{(\bar{\psi}|C^{-1}|\psi)}. \quad (\text{A.2})$$

Note that the partition function of the non-interacting system is contained in this relation via $Z_0^{-1} = \det C$. Introducing a continuous parameter Λ such that $C \rightarrow C_\Lambda$ we have $\mathcal{G}^{ac}[\bar{\eta}, \eta] \rightarrow \mathcal{G}^{ac}[\Lambda; \bar{\eta}, \eta]$:

$$\mathcal{G}^{ac}[\Lambda; \bar{\eta}, \eta] = \log \int d\mu_{C_\Lambda} [\bar{\psi}, \psi] e^{S_I[\bar{\psi}-\bar{\eta}, \psi+\eta]} \quad (\text{A.3})$$

We can eliminate the integral on the RHS using the relation [1]

$$\begin{aligned} \int d\mu_{C_\Lambda} [\bar{\psi}, \psi] e^{S_I[\bar{\psi}-\bar{\eta}, \psi+\eta]} &= e^{-(\delta_\eta|C_\Lambda|\delta_{\bar{\eta}})} e^{S_I[-\delta_\zeta, \delta_{\bar{\zeta}}]} e^{(\bar{\zeta}|\eta) - (\bar{\eta}|\zeta)} \Big|_{\zeta=\bar{\zeta}=0} \\ &= e^{-(\delta_\eta|C_\Lambda|\delta_{\bar{\eta}})} e^{S_I[-\bar{\eta}, \eta]} \end{aligned} \quad (\text{A.4})$$

Differentiation with respect to Λ then yields the Polchinski equation:

$$\partial_\Lambda \mathcal{G}^{ac} [\Lambda; \bar{\eta}, \eta] = -(\delta_\eta | \dot{C}_\Lambda | \delta_{\bar{\eta}}) \mathcal{G}^{ac} [\Lambda; \bar{\eta}, \eta] - \left(\frac{\delta \mathcal{G}^{ac} [\Lambda; \bar{\eta}, \eta]}{\delta \eta} \middle| \dot{C}_\Lambda \middle| \frac{\delta \mathcal{G}^{ac} [\Lambda; \bar{\eta}, \eta]}{\delta \bar{\eta}} \right) \quad (\text{A.5})$$

Note that the initial condition reads $\mathcal{G}^{ac} [\Lambda^0; \bar{\eta}, \eta] = S_I[-\bar{\eta}, \eta]$. Due to the first term on the RHS the Polchinski equation contains tadpole diagrams, which are inconvenient as stated in chapter 1. To eliminate these tadpoles and arrive at the Wiczerkowski equation we introduce a new functional \mathcal{G}_Λ^w defined as

$$\mathcal{G}^w [\Lambda; \bar{\eta}, \eta] := e^{-(\delta_\eta | D_\Lambda | \delta_{\bar{\eta}})} \mathcal{G}^{ac} [\Lambda; \bar{\eta}, \eta] \quad (\text{A.6})$$

Substituting this into equation A.5 yields the RGE for \mathcal{G}_Λ^w :

$$\partial_\Lambda \mathcal{G}^w [\Lambda; \bar{\eta}, \eta] = e^{-(\delta_\eta | D_\Lambda | \delta_{\bar{\eta}})} \left(\frac{\delta (e^{(\delta_\eta | D_\Lambda | \delta_{\bar{\eta}})} \mathcal{G}^w [\Lambda; \bar{\eta}, \eta])}{\delta \eta} \middle| \dot{D}_\Lambda \middle| \frac{\delta (e^{(\delta_\eta | D_\Lambda | \delta_{\bar{\eta}})} \mathcal{G}^w [\Lambda; \bar{\eta}, \eta])}{\delta \bar{\eta}} \right) \quad (\text{A.7})$$

In this form it is hard to see why this equation should be more convenient than the Polchinski equation. To make the advantage explicit and to prepare for the derivation of the component form of the RGE, we first note that the differential operators $e^{(\delta_\eta | D_\Lambda | \delta_{\bar{\eta}})}$ act separately on each functional \mathcal{G}^w in the bilinear term. We make this more explicit by introducing labels 1 and 2 to the fields in each expression and write

$$\begin{aligned} & \left(\frac{\delta (e^{(\delta_\eta | D_\Lambda | \delta_{\bar{\eta}})} \mathcal{G}^w [\Lambda; \bar{\eta}, \eta])}{\delta \eta} \middle| \dot{D}_\Lambda \middle| \frac{\delta (e^{(\delta_\eta | D_\Lambda | \delta_{\bar{\eta}})} \mathcal{G}^w [\Lambda; \bar{\eta}, \eta])}{\delta \bar{\eta}} \right) \\ = & \left(\frac{\delta (e^{(\delta_{\eta_1} | D_\Lambda | \delta_{\bar{\eta}_1})} \mathcal{G}^w [\Lambda; \bar{\eta}_1, \eta_1])}{\delta \eta_1} \middle| \dot{D}_\Lambda \middle| \frac{\delta (e^{(\delta_{\eta_2} | D_\Lambda | \delta_{\bar{\eta}_2})} \mathcal{G}^w [\Lambda; \bar{\eta}_2, \eta_2])}{\delta \bar{\eta}_2} \right) \bigg|_{\eta_1=\eta_2=\eta, \bar{\eta}_1=\bar{\eta}_2=\bar{\eta}} \end{aligned} \quad (\text{A.8})$$

Next, we use the general relation $\left(\frac{d}{dx}\right)^n f(x)g(x) = \left(\frac{d}{dx_1} + \frac{d}{dx_2}\right)^n f(x_1)g(x_2)$ at $x_1 = x_2 = x$ to write the differential operator $e^{-(\delta_\eta | D_\Lambda | \delta_{\bar{\eta}})}$ in front of the bilinear term as

$$e^{-(\delta_\eta | D_\Lambda | \delta_{\bar{\eta}})} = e^{-(\delta_{\eta_1} + \delta_{\eta_2} | D_\Lambda | \delta_{\bar{\eta}_1} + \delta_{\bar{\eta}_2})} \quad (\text{A.9})$$

Inserting this into equation A.7 we get

$$\begin{aligned} \partial_\Lambda \mathcal{G}^w [\Lambda; \bar{\eta}, \eta] = \\ e^{-(\delta_{\eta_1} | D_\Lambda | \delta_{\bar{\eta}_2})} e^{-(\delta_{\eta_2} | D_\Lambda | \delta_{\bar{\eta}_1})} \left(\frac{\delta \mathcal{G}^w [\Lambda; \bar{\eta}_1, \eta_1]}{\delta \eta_1} \Big| \dot{D}_\Lambda \Big| \frac{\delta \mathcal{G}^w [\Lambda; \bar{\eta}_2, \eta_2]}{\delta \bar{\eta}_2} \right) \Big|_{\eta_1 = \eta_2 = \eta, \bar{\eta}_1 = \bar{\eta}_2 = \bar{\eta}} \end{aligned} \quad (\text{A.10})$$

From this expression we can infer that no tadpoles appear on the RHS of the RGE, since the differential operators $(\delta_{\eta_1} | D_\Lambda | \delta_{\bar{\eta}_2})$ and $(\delta_{\eta_2} | D_\Lambda | \delta_{\bar{\eta}_1})$ connect the two contributions coming from $\mathcal{G}^w [\Lambda; \bar{\eta}_1, \eta_1]$ and $\mathcal{G}^w [\Lambda; \bar{\eta}_2, \eta_2]$. This leads to the diagrammatic representation shown in figure 1.2.

The RGE at the level of the actual Green functions is obtained by expanding $\mathcal{G}^w [\Lambda; \bar{\eta}, \eta]$ as in equation 1.11 on either side of equation A.10 and comparing the coefficients.

Appendix B

Evaluation of RHS for the Two-point Function

Here we comment on two essential steps in the evaluation of the two-loop contribution to the flow of the two-point function, namely the spin sum and the explicit evaluation of internal frequency sums together with the continuation to real frequencies.

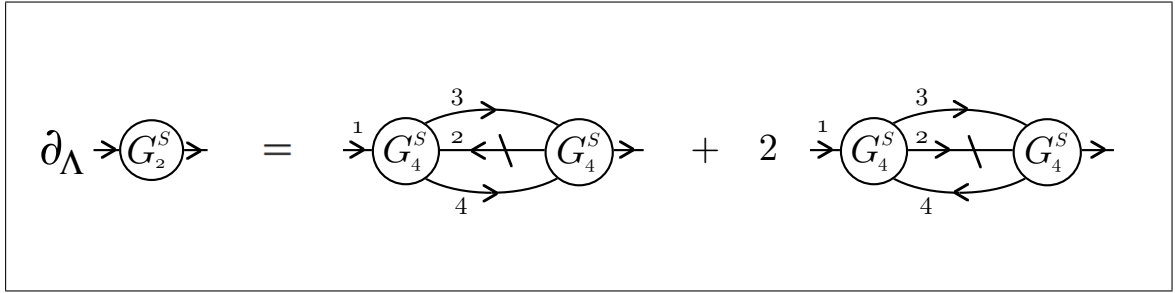


Figure B.1: The two contributions $PP\dot{H}$ and $PH\dot{P}$ to the flow of the two-point function.

To evaluate the two-loop diagram shown in figure B.1 we start from the following representation of the four-point function, as presented in chapter 1:

$$\begin{aligned}
 -G_4^S(\Lambda|\alpha, \beta; \gamma, \delta) &= \Gamma_\Lambda^s(k_\alpha, k_\beta; k_\gamma, k_\delta) \delta_{k_\alpha+k_\beta-k_\gamma-k_\delta} (\delta_{\sigma_\alpha \sigma_\delta} \delta_{\sigma_\beta, \sigma_\gamma} - \delta_{\sigma_\alpha \sigma_\gamma} \delta_{\sigma_\beta \sigma_\delta}) \\
 &+ \Gamma_\Lambda^t(k_\alpha, k_\beta; k_\gamma, k_\delta) \delta_{k_\alpha+k_\beta-k_\gamma-k_\delta} (\delta_{\sigma_\alpha \sigma_\delta} \delta_{\sigma_\beta, \sigma_\gamma} + \delta_{\sigma_\alpha \sigma_\gamma} \delta_{\sigma_\beta \sigma_\delta})
 \end{aligned}
 \tag{B.1}$$

The bilinear term consists of products of the type $\Gamma_\Lambda^{s,t}(k_1, k_2; k_3, k_4) \Gamma_\Lambda^{s,t}(k_4, k_3; k_2, k_1)$. Due to time-reversal and conjugation symmetries, at zero frequencies the four-point function is real and symmetric under exchange of incoming and outgoing momenta [1]. Within the static ap-

proximation we thus have $\Gamma_{\Lambda}^{s,t}(\mathbf{k}_1, \mathbf{k}_2; \mathbf{k}_3, \mathbf{k}_4) = \Gamma_{\Lambda}^{s,t}(\mathbf{k}_4, \mathbf{k}_3; \mathbf{k}_2, \mathbf{k}_1)$, and we can replace products of the type $\Gamma_{\Lambda}^{s,t}(\mathbf{k}_1, \mathbf{k}_2; \mathbf{k}_3, \mathbf{k}_4) \Gamma_{\Lambda}^{s,t}(\mathbf{k}_4, \mathbf{k}_3; \mathbf{k}_2, \mathbf{k}_1)$ by $\Gamma_{\Lambda}^{s,t}(\mathbf{k}_1, \mathbf{k}_2; \mathbf{k}_3, \mathbf{k}_4) \Gamma_{\Lambda}^{s,t}(\mathbf{k}_1, \mathbf{k}_2; \mathbf{k}_3, \mathbf{k}_4) = \Gamma_{\Lambda}^{s,t}(\mathbf{k}_1, \mathbf{k}_2; \mathbf{k}_3) \Gamma_{\Lambda}^{s,t}(\mathbf{k}_1, \mathbf{k}_2; \mathbf{k}_3)$, where we have omitted the "dependence" on the fourth momentum. Carrying out the sum over internal spin indices with the incoming/outgoing spin projection σ_1 held fixed, we find that cross terms of the type $\Gamma_{\Lambda}^s \Gamma_{\Lambda}^t$ cancel, and only contributions of the type $(\Gamma_{\Lambda}^{s,t})^2$ appear. Elementary algebra finally yields

$$\begin{aligned} \sum_{\sigma_2, \sigma_3, \sigma_4} \left[\Gamma_{\Lambda}^s (\delta_{\sigma_1, \sigma_4} \delta_{\sigma_2, \sigma_3} - \delta_{\sigma_1, \sigma_3} \delta_{\sigma_2, \sigma_4}) + \Gamma_{\Lambda}^t (\delta_{\sigma_1, \sigma_4} \delta_{\sigma_2, \sigma_3} + \delta_{\sigma_1, \sigma_3} \delta_{\sigma_2, \sigma_4}) \right]^2 \\ = 2 (\Gamma_{\Lambda}^s)^2 + 6 (\Gamma_{\Lambda}^t)^2, \end{aligned} \quad (\text{B.2})$$

where we have suppressed the momentum dependence in Γ_{Λ}^s and Γ_{Λ}^t . Next we evaluate the frequency sums over the Matsubara frequencies ω_2 and ω_3 explicitly, with the incoming/outgoing Matsubara frequency $i\omega_1$ and momentum \mathbf{p}_1 held fixed and ω_4 as well as \mathbf{p}_4 given by energy/momentum conservation. For the first term on the RHS in figure B.1 we get

$$\begin{aligned} \sum_{\omega_2, \omega_3} C(i\omega_2, \mathbf{p}_2) C(i\omega_3, \mathbf{p}_3) C(i\omega_1 + i\omega_2 - i\omega_3, \mathbf{p}_1 + \mathbf{p}_2 - \mathbf{p}_3) \\ = \sum_{\omega_3} \frac{1}{i\omega_3 - \xi_{\mathbf{p}_3}^0} \sum_{\omega_2} \frac{1}{i\omega_2 - \xi_{\mathbf{p}_2}^0} \frac{1}{i(\omega_1 + \omega_2 - \omega_3) - \xi_{\mathbf{p}_1 + \mathbf{p}_2 - \mathbf{p}_3}^0} \\ = (f(\xi_{\mathbf{p}_2}^0) - f(\xi_{\mathbf{p}_1 + \mathbf{p}_2 - \mathbf{p}_3}^0)) \sum_{\omega_3} \frac{1}{i\omega_3 - \xi_{\mathbf{p}_3}^0} \frac{1}{i(\omega_1 - \omega_3) + \xi_{\mathbf{p}_2}^0 - \xi_{\mathbf{p}_1 + \mathbf{p}_2 - \mathbf{p}_3}^0} \\ = \frac{(f(\xi_{\mathbf{p}_2}^0) - f(\xi_{\mathbf{p}_1 + \mathbf{p}_2 - \mathbf{p}_3}^0)) (f(\xi_{\mathbf{p}_3}^0) + b(\mathbf{p}_2 - \xi_{\mathbf{p}_1 + \mathbf{p}_2 - \mathbf{p}_3}^0))}{i\omega_1 + \xi_{\mathbf{p}_2}^0 - \xi_{\mathbf{p}_3}^0 - \xi_{\mathbf{p}_1 + \mathbf{p}_2 - \mathbf{p}_3}^0}, \end{aligned} \quad (\text{B.3})$$

where we have used the standard techniques of evaluating frequency sums to obtain the Fermi function $f(x) = \left(e^{\frac{x}{T}} + 1\right)^{-1}$ and the Bose function $b(x) = \left(e^{\frac{x}{T}} - 1\right)^{-1}$ [47]. The second term in figure B.1 is evaluated analogously. The continuation to real frequencies can now be done straightforwardly by setting $i\omega_1 \rightarrow \omega + i0^+$. Subsequently the relation $\Im \frac{1}{x+i0^+} = -\pi \delta(x)$ is used to obtain equations 4.12 and 4.13, with the combinatorial prefactors found as described in appendix A.

Bibliography

- [1] C. J. Halboth, *Niederenergie-Eigenschaften zweidimensionaler Fermi-Systeme*, PhD thesis, RWTH Aachen, 1999.
- [2] C. Honerkamp, *Superconductivity and Magnetism in the Extended Hubbard Model*, PhD thesis, ETH Zürich, 2000.
- [3] K. G. Wilson, *Rev. Mod. Phys.* **47**, 773 (1975).
- [4] A. A. Katanin and A. P. Kampf, *Phys. Rev. Lett.* **93** (2004).
- [5] S. Andergassen et al., *Phys. Rev. B* **70**, 075102 (2004).
- [6] C. Honerkamp and M. Salmhofer, *Phys. Rev. B* **64**, 184516 (2001).
- [7] C. Honerkamp, M. Salmhofer, and T. M. Rice, *Eur. Phys. J. B* **27**, 127 (2002).
- [8] C. Honerkamp, D. Rohe, S. Andergassen, and T. Enss, *Phys. Rev. B* **70**, 235115 (2004).
- [9] J. G. Bednorz and K. A. Müller, *Z. Phys. B* **64**, 189 (1986).
- [10] P. W. Anderson, *Phys. Rev.* **115**, 2 (1959).
- [11] J. Hubbard, *Proceedings of the Royal Society of London. Series A, Mathematical and Physical Sciences* **276**, 238 (1963).
- [12] M. C. Gutzwiller, *Phys. Rev. Lett.* **103**, 159 (1963).
- [13] J. Kanamori, *Prog. Theor. Physics* **301**, 275 (1963).
- [14] P. W. Anderson, *Science* **235**, 1196 (1987).
- [15] P. W. Anderson, *Physica Scripta* **T102**, 10 (2001).
- [16] E. H. Lieb and F. Y. Wu, *Phys. Rev. Lett.* **20**, 1445 (1968).
- [17] M. Salmhofer, *Renormalization*, Springer, 1998.
- [18] C. J. Halboth and W. Metzner, *Phys. Rev. B* **61**, 7364 (2000).
- [19] C. Honerkamp, *Eur. Phys. J. B* **21**, 81 (2001).
- [20] J. R. Waldram, *Superconductivity of Metals and Cuprates*, IOP Publishing Ltd, 1996.

-
- [21] E. Dagotto, *Rev. Mod. Phys.* **66**, 763.
- [22] J. W. Negele and H. Orland, *Quantum Many-Particle Systems*, Advanced Book Classics, Perseus Books, 1988.
- [23] J. Feldman, M. Salmhofer, and E. Trubowitz, XIIth International Congress of Mathematical Physics , 2411 (1997).
- [24] J. Feldman, H. Knoerrer, and E. Trubowitz, Proceedings of the XIVth International Congress on Mathematical Physics, University of Lisbon, Portugal (ICMP2003) - (C) World Scientific (2003).
- [25] A. Neumayr and W. Metzner, *Phys. Rev. B* **67**, 035112 (2003).
- [26] N. D. Mermin and H. Wagner, *Phys. Rev. Lett.* **17**, 1133 (1966).
- [27] J. Feldman, H. Knoerrer, and E. Trubowitz, *Fermionic Functional Integrals and the Renormalization Group*, volume 16 of *CRM Monograph Series*, ISSN: 1065-8599, American Mathematical Society, 2002.
- [28] T. R. Morris, *Int. J. of Mod. Phys. A* **92**, 2411 (1994).
- [29] M. Salmhofer, *Commun. Math. Phys.* **194**, 249 (1998).
- [30] M. Salmhofer and C. Honerkamp, *Prog. Theor. Physics* **105**, 1 (2001).
- [31] N. Furukawa, T. M. Rice, and M. Salmhofer, *Phys. Rev. Lett.* **81**, 3195 (1998).
- [32] C. Honerkamp, M. Salmhofer, N. Furukawa, and T. M. Rice, *Phys. Rev. B* **63**, 035109 (2001).
- [33] V. Y. Irkhin, A. A. Katanin, and M. I. Katsnelson, *Phys. Rev. B* **64**, 165107 (2001).
- [34] V. Y. Irkhin and A. A. Katanin, *Phys. Rev. B* **64**, 205105 (2001).
- [35] V. Y. Irkhin, A. A. Katanin, and M. I. Katsnelson, *Phys. Rev. Lett.* **89**, 076401 (2002).
- [36] A. P. Kampf and A. A. Katanin, *Phys. Rev. B* **67**, 125104 (2003).
- [37] C. Honerkamp and M. Salmhofer, *Phys. Rev. B* **67**, 174504 (2003).
- [38] A. A. Katanin and A. P. Kampf, *Phys. Rev. B* **68**, 195101 (2003).
- [39] J. Polchinski, *Nuclear Physics B* **231**, 269 (1983).
- [40] D. Zanchi and H. J. Schulz, *Z. Phys. B* **103**, 339 (1997).

-
- [41] D. Zanchi and H. J. Schulz, *Europhys. Lett.* **44**, 235 (1998).
- [42] D. Zanchi and H. J. Schulz, *Phys. Rev. B* **61**, 13609 (2000).
- [43] C. Wierczkowski, *Commun. Math. Phys.* **120**, 149 (1988).
- [44] C. J. Halboth and W. Metzner, *Phys. Rev. Lett.* **85**, 5162 (2000).
- [45] P. Chauve and P. Le Doussal, *Phys. Rev. E* **64**, 051102 (2001).
- [46] D. Zanchi and H. J. Schulz, *Phys. Rev. B* **54**, 9509 (1996).
- [47] W. Nolting, *Grundkurs Theoretische Physik 7 - Vielteilchentheorie*, Vieweg, 1997.
- [48] G. Engeln-Müllges and F. Reuter, *Numerik-Algorithmen*, VDI Verlag, 1996.
- [49] D. J. Thouless, *Ann. Phys.* **10**, 553 (1960).
- [50] E. Babaev and H. Kleinert, *Phys. Rev. B* **59**, 12083 (1999).
- [51] B. Binz, D. Baeriswyl, and B. Douçot, *Ann. Phys.* **12**, 704 (2003).
- [52] W. Kohn and J. M. Luttinger, *Phys. Rev. Lett.* **15**, 524 (1965).
- [53] H. J. Schulz, *Phys. Rev. Lett.* **64**, 1445 (1990).
- [54] G. D. Mahan, *Many-Particle Physics*, Plenum Press, 1990.
- [55] W. Jones and N. H. March, *Theoretical Solid State Physics*, Wiley, 1973.
- [56] A. M. Zagoskin, *Quantum Theory of Many-Body Systems*, Springer, 1998.
- [57] A. P. Kampf and J. R. Schrieffer, *Phys. Rev. B* **42**, 7967 (1990).
- [58] P. Monthoux, A. V. Balatsky, and D. Pines, *Phys. Rev. Lett.* **67**, 3448 (1991).
- [59] P. Monthoux, A. V. Balatsky, and D. Pines, *Phys. Rev. B* **46**, 14803 (1992).
- [60] P. Monthoux and D. Pines, *Phys. Rev. B* **47**, 6069 (1993).
- [61] P. Monthoux and D. Pines, *Phys. Rev. B* **49**, 4261 (1994).
- [62] D. Pines and P. Monthoux, *J. Phys. Chem. Solids* **56**, 1651 (1995).
- [63] D. Pines, *Z. Phys. B* **103**, 129 (1997).
- [64] J. Schmalian, D. Pines, and B. Stojković, *Phys. Rev. Lett.* **80**, 3839 (1998).
- [65] J. Schmalian, D. Pines, and B. Stojković, *J. Phys. Chem. Solids* **59**, 1764 (1998).

-
- [66] J. Schmalian, D. Pines, and B. Stojković, Phys. Rev. B **60**, 667 (1999).
- [67] T. Dahm and L. Tewordt, Phys. Rev. Lett. **74**, 793 (1995).
- [68] T. Dahm and L. Tewordt, Phys. Rev. B **52**, 1297 (1995).
- [69] T. Dahm, D. Manske, and L. Tewordt, Europhys. Lett. **55**, 93 (2001).
- [70] D. Manske, *Theory of Unconventional Superconductors*, Springer, 2004.
- [71] S. Wermbter, Phys. Rev. B **55**, R10149 (1997).
- [72] Y. Yanase and K. Yamada, J. Phys. Soc. Japan **70**, 1659 (2001).
- [73] Y. Yanase et al., Physics Reports **387**, 1 (2003).
- [74] Y. M. Vilk, L. Chen, and A.-M. S. Tremblay, Phys. Rev. B **49**, 13267 (1994).
- [75] A.-M. Daré, Y. M. Vilk, and A.-M. S. Tremblay, Phys. Rev. B **53**, 14236 (1996).
- [76] Y. M. Vilk and A.-M. S. Tremblay, J. Phys. I France **7**, 1309 (1997).
- [77] B. Kyung, Phys. Rev. B **58**, 16032 (1998).
- [78] B. Kyung, Phys. Rev. B **59**, 14757 (1999).
- [79] B. Kyung, J. Phys. Chem. Solids **61**, 13 (2000).
- [80] B. Kyung, J.-S. Landry, and A.-M. S. Tremblay, Phys. Rev. B **68**, 174502 (2003).
- [81] B. Kyung, V. Hankevych, A.-M. Daré, and A.-M. S. Tremblay, cond-mat/0312499 v2 (2004).
- [82] V. Hankevych, B. Kyung, A.-M. Daré, D. Sénéchal, and A.-M. S. Tremblay, cond-mat/0407085 v1 (2004).
- [83] D. Sénéchal and A.-M. S. Tremblay, Phys. Rev. Lett. **92**, 126401 (2004).
- [84] T. Saikawa and A. Ferraz, Int. J. of Mod. Phys. B **14**, 2271 (2000).
- [85] T. Saikawa and A. Ferraz, Eur. Phys. J. B **20**, 65 (2001).
- [86] C. Huscroft, M. Jarrell, T. Maier, S. Moukouri, and A. N. Tahvildarzadeh, Phys. Rev. Lett. **86**, 139 (2001).
- [87] O. Parcollet, G. Biroli, and G. Kotliar, Phys. Rev. Lett. **92** (2004).
- [88] R. Preuss, W. Hanke, C. Gröber, and H. G. Evertz, Phys. Rev. Lett. **79**, 1122 (1997).

- [89] D. Zanchi, *Europhys. Lett.* **55**, 376 (2001).
- [90] N. P. Armitage et al., *Phys. Rev. Lett.* **87**, 147003 (2001).
- [91] N. P. Armitage et al., *Phys. Rev. Lett.* **88**, 257001 (2002).
- [92] T. Claesson et al., *Phys. Rev. Lett.* **93**, 136402 (2004).
- [93] P. W. Anderson, *Physics Today* **43**, 9 (1990).

DANKSAGUNG

An dieser Stelle möchte ich mich bei den zahlreichen Personen bedanken, die zum Gelingen dieser Arbeit beigetragen haben! Sie alle einzeln aufzulisten würde den Rahmen sprengen, ich danke aber insbesondere

- meinem Betreuer Herrn Prof. Dr. Walter Metzner für die hervorragende Betreuung.
- Herrn Prof. Dr. A. Muramatsu für das Übernehmen der Mitberichteraufgabe.
- meinen Kollegen aus der Abteilung Metzner, die immer für Diskussionen und Fragen zur Verfügung standen. Besonderer Dank geht an Tilman Enss, Roland Gersch, Dirk Manske, Carsten Honerkamp und Roland Zeyher für das Korrekturlesen des Manuskripts.
- unserer Sekretärin Frau Ingrid Knapp für ihre Hilfsbereitschaft im Allgemeinen und ihre Unterstützung in der Reiseplanung im Besonderen.
- meinem westfälischen Bürokollegen Julius Reiss für das Ertragen meines rheinländischen Temperaments.
- der gesamten EDV Abteilung des MPI-FKF, insbesondere in Person Armin Schuhmachers, für die erstklassige Unterstützung.
- der Abteilung Jansen für die tägliche Versorgung eines externen Theoretikers mit Kaffee.

Dieses Projekt wurde von der Deutschen Forschungsgemeinschaft unterstützt.

LEBENS LAUF

Name	Daniel Rohe
Geboren am	25. Januar 1974
Geburtsort	Jülich
seit Jan. 2002	Wissenschaftlicher Mitarbeiter bei Prof. Dr. W. Metzner, Max-Planck-Institut für Festkörperforschung in Stuttgart
Okt. 2000 – Dez. 2001	Wissenschaftlicher Mitarbeiter bei Prof. Dr. W. Metzner, Institut für Theoretische Physik, RWTH Aachen
Okt. 1995 – Okt. 2000	Studium der Physik an der RWTH Aachen
1993 – 1994	Zivildienst beim Malteser Hilfsdienst, Jülich
1984 – 1993	Gymnasium Haus Overbach, Jülich-Barmen Abitur im Juni 1993